Faculty of Engineering and Science

Grid-tie Quasi Z-Source Inverter-Based Static Synchronous Compensator

Yong Sut Khan

This thesis is presented for the Degree of
Master of Philosophy (Electrical Engineering)
of
Curtin University

October 2018

Declaration

To the best of my knowledge and belief this thesis contains no material previously published by any other person except where due acknowledgment has been made.

This thesis contains no material which has been accepted for the award of any other degree or diploma in any university.

Signature: .....

Date: .....

Abstract

This research work proposes intensive study and mathematical modelling analysis of transformer-less quasi Z-source inverter (qZSI) based static synchronous compensator (STATCOM) system. Among the shunt-connected Flexible AC Transmission System (FACTS) controllers, STATCOM has shown extensive feasibility and effectiveness in solving a wide range of power quality problems. From the literature reviews, multilevel cascaded H-bridge inverter (MCHI) is undoubtedly the most adaptable power inverter topology in STATCOM application to produce high quality sinusoidal alternating current (AC) waveform with minimum harmonics. However, the direct current (DC) side of H-bridge inverter requires an additional bidirectional DC-DC converter (i.e., resulting a two-stage system) to achieve four quadrants of operations. This results in high cost and complicated control of the converter. A qZSI demonstrates the advantages of being able to perform power conversions from DC to AC, AC to DC, DC to DC and AC to AC through a single-stage topology when compare with the counterpart. This significantly enhances the inverter efficiency and reduces the overall construction cost. Moreover, each phase-leg of qZSI module (i.e., formed by two series-connected switches) can turn on simultaneously with no dead-time to improve the inverter reliability and the quality of the generated AC output waveform. In this work, a single-phase three-level qZSI is acted as a STATCOM system to compensate the grid reactive power (VAR) at the point of coupling (PCC) under different loading conditions. A new controller-based lead compensator is developed to achieve fast DC-link voltage balance across each quasi Z-source (qZS) network, which is unachievable with the traditional proportional integral (PI) controller. To evaluate the superiority of the proposed system and control scheme, extensive simulation studies are conducted accordingly, where all the results are documented systematically.

Keywords: Quasi Z-source Inverter, Cascaded Multilevel Inverter, Photovoltaic (PV), Static Synchronous Compensator (STATCOM)

Acknowledgement

This project is by far the most significant accomplishment in my engineering career. There are few persons who deserve my sincere appreciation in providing guidance to me during my master's degree.

Firstly, I would like to express my immense gratitude to my supervisor, Dr. Law Kah Haw, who have been guiding and advising me through my master's degree. I would like to thank my thesis committees, my co-supervisors, Dr. Ammar and Dr. Wendy and my project chairperson, Dr. Lenin for helping me during this entire journey.

Lastly, I would like to thank my parents for the love and encouragement for me to complete my research work.

List of Publication

1. K. H. L. Sut Khan Yong, Wendy Pei Qin Ng, Mohamed Dahidah, "Lead Compensator Design for Single-Phase Quasi Z-Source Inverter," Journal of Telecommunication, Electronic and Computer Engineering, vol. 10, 2017.
2. J. O. S. Xuan, K. Y. S. Khan, L. K. Haw, W. N. P. Qin, and M. Dahidah, "CCM and DCM analysis of quasi-z-source inverter," in 2017 IEEE Conference on Energy Conversion (CENCON), 2017, pp. 157-162.

Nomenclature

BCM	Boundary conduction mode
CCM	Continuous conduction mode
CHB	Cascaded H-bridge
DCM	Discontinuous conduction mode
DFR	Double-frequency ripple
FET	Field-effect transistors
Gan	Gallium nitride
I&C	Incremental and conductance
MBC	Maximum boost control
MCBC	Maximum constant boost control
MCHI	Multilevel Cascaded H-bridge Inverter
MPP	Maximum power point
MPPT	Maximum power point tracking
P&O	Perturb and observe
PAM	Pulse width amplitude modulation
PCC	Point of common coupling
P	Proportional
PI	Proportional integral
PID	Proportional integral derivative
PLL	Phase-lock loop
PSA-PWM	Phase-shifted amplitude PWM
PS-SPWM	Phase-shifted SPWM
PV	Photovoltaic
PWM	Pulse width modulation
qSBI	Quasi switched boost H-bridge inverter
qZCHI	Quasi Z-source cascaded multilevel inverter
qZS	Quasi Z-source
qZSI	Quasi Z-source Inverter
SBC	Simple boost control

SPWM	Sinusoidal pulse width modulation
SRF	Synchronous reference frame
STATCOM	Static synchronous compensator
SVM	Space vector modulation
THD	Total harmonic distortion
VAR	Reactive power

Table of Contents

List of Figure

List of Tables

Chapter 1 : A Critical Review for the Open Literature

Batteries have become one of the most promising energy resources in recent years and have increased enormously in the markets. DC/AC inverter is designed as the core of the battery system that inverts DC to AC supply waveform to suit remote stand-alone application or off-grid power system. In the past five years, numerous control schemes have been applied to battery qZSI based STATCOM system. Particularly, DC-link voltage control scheme has been developed to balance the DC-link voltage in qZS network. In most cases, proportional-integral (PI) controller has been the most popular method to perform control actions specifically in the STATCOM's feedback loops [1-4]. However, PI controller shows some drawbacks which include slow response speed as well as poor robust performance against the system uncertainties and exogenous disturbances. Also, there are several existing works revealed that the use of PI controller will lead to poor transient and dynamic responses as well as causing instability to the system when the system parameters and operating points are varying [5, 6]. Another drawback of PI controller is that it could not provide precise tracking on the commanded values which is the main cause of poor transient response and instability in the STATCOM system [7]. Similarly, no research has been carried out to demonstrate the dynamic and transient performances of qZSI based STATCOM system under different loading condition. Besides, the mathematical derivation of STATCOM controller's parameter (i.e., gain parameters) has not been specifically defined. Furthermore, details on the modulation techniques as well as the application of both the sampling and switching frequencies on the modulation techniques are not revealed.

The aforementioned phenomena also apply to qZSI module itself, where the DC side impedance design and efficiency calculation methods are not established in any work. These include:

i. The relationship between the generated line voltage total harmonic distortion (THD) and the shoot-through duty cycles.
ii. The relationship between the generated line voltage THD and the modulation index.

iii. The relationship between the shoot-through duty cycles and the pulse width modulation (PWM) modulation index.
iv. The control scheme to provide direct control of shoot-through duty ratio based on different loading conditions.
v. The boundary condition at which the qZSI network will operate in continuous conduction mode (CCM) or discontinuous conduction mode (DCM).

All these matters have direct effect on the cost, size, reliability, dynamic and transient performances of battery qZSI based STATCOM system.

1.1 Building the Justification

1.1.1 The Research Field

QZSI is one type of power inverter which can boost the DC input voltage and invert it to AC waveform in a single-stage topology. When compared with conventional DC-AC inverter which requires additional DC-DC converter to buck/boost the DC input voltage, the two series-connected switches from each phase-leg of qZSI can be turned on at the same time. This interval is referred to as the shoot-through state, which the inductors will be charged up. On the contrary, the inductors will release its stored energy and charge up the qZS network's capacitors in active-state to achieve boosting effect. QZSI can operate in boundary, CCM and DCM. However, CCM mode is preferable because the input current will never fall to zero; hence, resulting in lower voltage stress and higher system efficiency.

STATCOM is one of the inverter-based FACTS devices. It can be used as a shunt-connected compensator to control the power flow, enhance the transient stability, and improve the power factor of the grid. To achieve that, STATCOM is connected at the PCC to inject or absorb active and reactive current. For instance, when inductive loading condition or low PCC voltage is detected, STATCOM will produce larger magnitude of AC voltage than the PCC voltage to inject the current at the PCC. In contrast, STATCOM can absorb reactive current from the PCC when PCC voltage is higher or capacitive loading condition is sensed.

1.1.2 Research Gap

The selection of switching frequency has direct proportional relation with the active suppression of THD and the dynamic response of a qZSI. Since a single-stage qZSI topology can be operated with considerable high-equivalent switching frequency (i.e., from 5 kHz [8] to 100 kHz [4, 9]), the qZSI based STATCOM system will provide fast power compensation across the grid under different loading conditions. Nevertheless, the switching loss, conduction loss, and power handling of qZSI module should be taken into consideration in the design process.

The cost and size of STATCOM system can be affected by the size of the DC-link passive components (i.e., capacitors and inductors). qZSI is no doubt the favourable inverter when compared with other DC-DC converters due to its smaller size of LC filters at high switching frequencies. Nevertheless, mathematical formulation to obtain the effective value of each passive component should be proposed to achieve a compromise between size, efficiency, switching frequency, and cost for a given power rating.

There are two capacitors in a qZS network. Unlike inductor current, DC voltage of capacitors in qZS network will never fall to zero in any operating mode (i.e., boundary condition, CCM and DCM). Till present, there is no existing work has been done to investigate the fundamental mathematical derivation of the steady-state small-signal equivalent circuit of battery qZSI based STATCOM system.

1.1.3 Research Questions

The research questions are listed as below:

i. What are the relationships between the efficiency and power density of the battery qZSI based STATCOM system with
   a) Switching frequency
   b) qZS network parameters
   c) boundary condition, CCM and DCM operation

ii. Do the shoot-through reference lines, which are used to control the shoot-through duty ratio via intersection of carrier waveform affect the THD of the generated PWM voltage, increase the output current ripple as well as influence the qZS network design and the system efficiency?

iii. Is qZSI based STATCOM system able to provide fast acting dynamic power compensation for voltage support during fortuity events [10, 11] and then reach steady-state within 200ms according to the grid codes [12]?

1.2 Objectives

The aim of this research work is to design transformer-less battery qZSI based STATCOM system for grid-tie application. The research objectives can be classified as:

i. Derivation of mathematical equation to determine the boundary condition, CCM and DCM and validate the accuracy of the mathematical equation by examine the variation of simulation results from theoretical value (deviation within +/-10%).

ii. Development of control scheme to achieve balanced DC-link voltage in qZSI to ensure the voltage deviated within +/- 10% from the pre-set DC voltage reference.

iii. Design the battery qZSI STATCOM system that can provide reactive power compensation to the grid and achieve steady-state within $200ms$ when a step change of loading condition is applied.

1.3 Novelty, outcomes and Significance

The first novelty of this research work is the development of battery qZSI STATCOM system. In this research work, the proposed system is utilized to provide reactive current compensation to the grid. Furthermore, the fundamental mathematical equations of the steady-state small-signal equivalent circuit of the proposed system which has not been covered in any literature are derived.

On the other hand, lead compensator is used to replace PI controller to achieve fast and stable DC-link voltage balance in qZS impedance network. According to literature review, lead compensator demonstrated better performance than PI and PID controller in controlling the speed of machine and robotic movement [13, 14]. Nevertheless, no research has been carried out to implement lead compensator in voltage or current control loop of a qZSI topology.

Apart from that, several researchers have defined the boundary condition, CCM and DCM in qZSI [42, 43]. However, no existing work had been done to distinguish the operating mode between CCM and DCM in qZSI topology. In this work, mathematical equations are derived to distinguish the operating modes of qZSI in boundary condition, CCM and DCM. Noticed that DC-link output voltage generated by qZSI diverges to a larger value when the topology changes from CCM to DCM mode. Most research works only focused on CCM mode, but knowing that in real-life application, the qZSI topology has the contingency to go from CCM to DCM or vice versa due to the changes in loading condition. Therefore, it is important to derive a mathematical equation that define the DC-link voltage of qZSI in DCM mode.

The outcomes of this research work are summarized as follows:

i. The derived mathematical equations (i.e., to distinguish between boundary condition, CCM and DCM) reflect the selection of the size of passive component (i.e., inductor) to construct qZS network. Designing a qZSI topology that operates in CCM mode reduces the voltage stress and thus increasing the overall efficiency. The selection of the size of passive components also provide direct influence on the dynamic and transient response of the qZS network. On the contrary, the operation mode of qZSI in DCM must be taken into consideration as well. When

the qZSI topology changes from CCM to DCM, the derived mathematical equation that characterized DC-link voltage in DCM is complied in the control system block diagram to avoid undesired deviation in output voltage.

ii. The developed controller (indicated in second novelty) ensures stable and good dynamic responses in DC-link voltage which attain a maximum percentage overshoot of 10% and accomplish steady-state in $\mathbf{200}\boldsymbol{ms}$ when there is a step change in loading condition.

iii. The proposed qZSI should be ensured to generate AC voltage with THD of 5% or less. A low THD output voltage indicates that the inverter topology produces a more accurate and undistorted voltage to the grid.

1.4 Significances

The significances of this research work are listed as follows:

i. The proposed system can improve the power quality as well as the system efficiency of battery-based electricity generation.
ii. The proposed system provides power compensation to the grid.
iii. This research project can be implemented in rural electrification projects especially in Sabah and Sarawak at where intensive solar energy is available and inland transportation is less developed. The coverage can be extended to remote and isolated areas with minimal cost as continuous grid connection from urban electricity generation source to remote area is limited.
iv. The number of components used in the proposed system are reduced due to lower number of switching elements. The reduction in components used allows the cost of the inverter system to be reduced in proportional.
v. This research project could improve and accelerate the contribution of solar energy in Malaysia electricity generation and it is expected to be able to reduce the non-renewable energy consumption especially the use of fossil fuels. Hence, resulting in the reduction of harmful by-product and greenhouse gases emission which came from transportation and power generation sectors.
vi. This research project can be upgraded and commercialize into electronic products in industry and household application.

1.5 Research Method

The initial phase of this research work is to investigate the characteristics of battery resource and the operating characteristics of qZSI. Then, novel control scheme and modulation technique was explored and implemented for qZSI to operate in either boundary conduction mode (BCM), CCM or DCM. All previous efforts have been extended and acting as a STATCOM system. After verifying all theoretical analysis, further validation has been carried out via simulation results. The 1.5 years research activities are summarized in the Gant charts under Research Timeline section. This research work has been carried out according to the following stages:

i. Design of qZSI's DC-link controller:

Several approaches have been carried out to design the controller for qZSI to ensure desired PWM duty ratio generation and stabilization of its DC-link voltage. These include:

a) Mathematic derivation of small-signal model of qZSI (i.e., its state-space equations and transfer functions),
b) Mathematic derivation of qZSI in boundary, CCM and DCM,
c) Signal-flow graph of qZSI's system variables (i.e., its dynamic modelling), and
d) Design of DC-link controller (i.e., lead compensator).

Besides that, proper selection of the size of passive components (i.e., capacitors and inductors) should be taken into consideration in the qZS impedance network design process.

For instance, the size of the inductor determines the qZSI operating mode (i.e., boundary condition, DCM or CCM) while the capacitor value has direct effect to the DC-link voltage ripple. In addition, the size of these passive components has a direct influence on the dynamic and transient response of a control scheme.

ii. Simulation and Verification of Models:

The works have been carried out using graphical programming tool (i.e., MATLAB/Simulink software package). This includes the implementation of grid-tie PV-battery qZCHI based STATCOM system, which aimed to achieve both grid-tie and reactive current compensation in qZS network. The performance of the proposed

system has been measured under all or either in boundary, CCM or DCM. The dynamic and transient responses of the proposed control scheme (i.e., STATCOM feed-forward and DC-link controllers) have been evaluated and discussed briefly. The in-depth research methodology of the qZSI model were explained in more details in their own sections (i.e., chapter 4 to chapter 6).

1.6 Thesis outline

A brief description for each chapter is provided as follows, a more detail explanations for each chapter have been covered in the following section.

Chapter 1:

Provides a general introduction covering the power electronics technology. This chapter also covers the research background, research gap and relevant research questions, scope and objective, novelties, outcomes and significant of this project. Moreover, this chapter includes one section which describes a brief introduction on the research methods taken to achieve the aim of the project. The details methodology is included in of the following chapters (i.e., Chapter 3, Chapter 4 and Chapter 5).

Chapter 2:

This chapter describes the literature reviews which is relevant to this research topic. This chapter also provides the comprehensive investigation on the previous researchers' finding in qZSI topology and its DC-link control system. In addition, this chapter provides a comparison of different type of existed controllers and its performance in maintaining the dynamic and transient response of inverter topology. Furthermore, the operating modes of the qZSI are also discussed and investigated including CCM and DCM. Using the literature reviews, able to provide with more research questions and solution finding.

Chapter 3:

This chapter covers the working principle of qZSI in both CCM and DCM. This includes the mathematical equations to distinguish between these modes. This chapter also discusses on the parameters that have a direct impact on the operating mode of qZSI. Simulation results have been included to verify the feasibility of the derived equations.

Chapter 4:

This chapter covers the detail mathematical derivation of qZSI large and small-signal analysis. The working principle and the design procedure of the proposed controller (i.e., lead compensator) are explained in detail. Simulation results are presented at the end of this chapter to identify the performance of the proposed controller. The simulation results consist of two parts, first part includes the effectiveness of the controller in maintaining the DC-link voltage when a step change in reference DC-link voltage was applied. The second part shows the simulation results of the proposed lead compensator when different loading conditions were applied in the output load.

Chapter 5:

Chapter 5 presents different methods used to regulate the power quality of the qZSI module at the PCC and when qZSI is integrated with PV power system. This includes the used of maximum power point tracking (MPPT) algorithm to stabilize the fluctuation of the PV power. Meanwhile, STATCOM system is responsible to provide power factor correction for the grid to maximize power transmission efficiency. Then, it is followed by the modelling of two energy storing battery-based qZSI. This includes the derivation of the transfer function of the proposed model. This chapter is later extended with the modelling of PV-based qZSI model with STATCOM system. The chapter is ended with two simulation results; the first simulation covers the employment of MPPT algorithm into qZSI module to achieve maximum power tracking. Second simulation depicts the $\boldsymbol{i_{oq}}$ algorithm in providing reactive power compensation to the grid.

Chapter 6:

Chapter 6 presents the conclusion remarks of the entire research project as well as the possible future works to be carried on.

Chapter 2 : Literature review

2.1 Introduction

Due to the fluctuation in fuel price which is a common circumstance in recent years, it has caused extensive growth in power electronics and battery industries. As a result, the demand for Electric Vehicles (EVs) has grown drastically over the past two years [15]. This lead to a lower equilibrium cost and hence, more consumers to purchase EVs since then. Therefore, power quality and efficiency issues have becoming a very important subject to be investigated. Moreover, most of the existing unidirectional EV's battery chargers with conventional two-stage rectifier-inverter circuit cannot be used in smart grid for vehicle-to-grid purpose [16, 17]. To overcome the stated phenomena, the integration of power electronic and renewable energy generation systems promises alternatives to replace conventional generation units for electricity regeneration.

Apart from that, the STATCOM system plays an important role in maintaining high system efficiency in converter topology. Reactive power is present in converter system due to the reactive components such as inductors and capacitors in an AC power system. High reactive power generated in the power grid will cause extensive power loss. To avoid power loss, the power factor must be kept as close to unity as possible. Therefore, STATCOM system plays the role in reactive power compensation by regulating the desired output AC voltages or current which is to be fed into the grid synchronously. The STATCOM system provide power compensation by either generating or absorbing reactive power.

2.2 qZSI topology

The qZSI topology (see Figure 2.1(a)) was first emerged in 2008 as an improved version of Z-source inverter (see Figure 2.1(b)) which introduced back in 2003 [18]. The improvements of qZSI include constant DC current drawn from the source [19, 20], less switching pulses [21], lower passive component rating, and reduction of capacitor's voltage stress in the qZS network [22]. Conventional H-bridge inverter requires an extra DC-DC boost converter (see Figure 2.2), which form a two-stage system, to achieve variable DC voltage levels across its DC-link. When compared with qZSI, the generated AC output waveform via the two-stage system is distorted due to the dead-time employed across each phase-leg to prevent short-circuit occurs through the series-connected upper and lower switches. Moreover, the integration of DC-DC converter with H-bridge inverter increases the construction cost and reduces the operating efficiency [23]. For qZSI, it provides boosting capability and voltage inversion in just a single-stage. It allows the series-connected active switches to be turned on simultaneously in shoot-through state and the DC voltage to be boosted in active-state. These aspects made qZSI an attractive topology for interfacing with renewable energy sources, especially wind and solar energy to the grid [23-28].

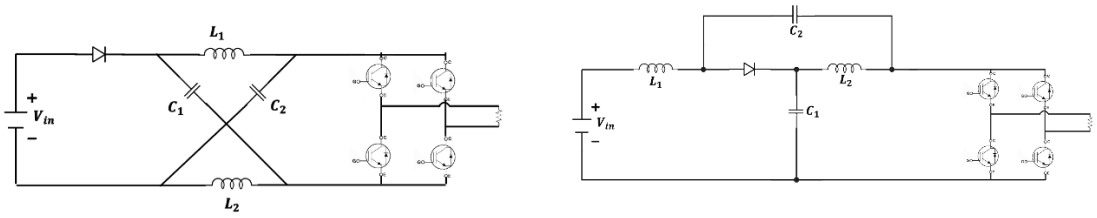

(a) *(b)*

Figure 2.1: Single-phase (a) Z-source inverter and (b) qZSI

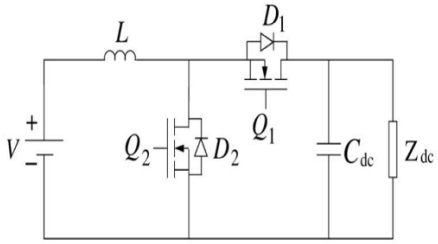

Figure 2.2: Traditional two-stage buck-boost inverter

Figure 2.3 (a) depicts circuit diagrams of conventional MCHI and qZS cascaded H-bridge inverter (qZCHI) topologies. MCHI, which acts as voltage-source inverter (VSI), produces less THD of multilevel output voltage with low switching frequency and possibly, eliminate the needs of AC filters [24-26]. Those are achieved by stacking more H-bridge inverter in series to generate higher-level staircase sinusoidal voltage waveform. Nevertheless, even though MPPT has been employed in the module, MCHI is still suffered with extensive power loss and DC-link voltage unbalance across each unit which may cause instability. Then, qZCHI overcome the aforementioned disadvantages of conventional MCHI by combining the quasi impedance network (i.e., with 2 pairs of LC filters) and H-bridge inverter [2-4, 27, 28]. The network is shown in Figure 2.3(b). The bridge leg of qZSI allows shoot-through states to occur without extra switching element required on the DC side. These features made qZCHI competitive in the application of PV power system in terms of efficiency and reliability.

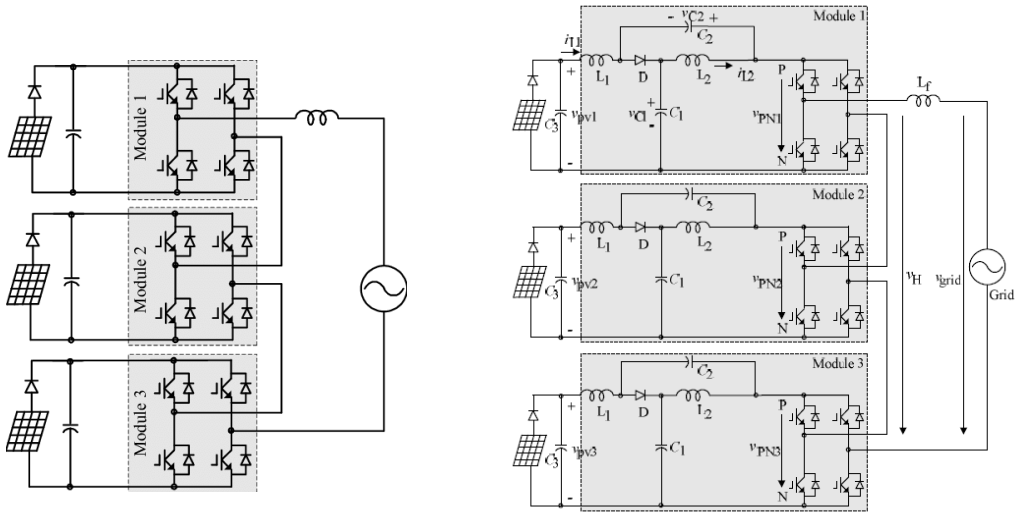

(a) *(b)*

Figure 2.3: Single-phase circuit diagram of (a) MCHI and (b) Multilevel qZCHI

2.3 Pulse Width Modulation Techniques of qZSI

During the past decade, qZSI topology had undergone fast development because of their promising characteristics. Like other power conversion topologies, the key elements of qZSI consist of the voltage/current control scheme, PWM technique, and the circuit structure itself. For instance, a semi-Z-source inverter with only two active switching devices was proposed in [1] to realize the same output voltage produced by qZSI. In addition, the introduction of shoot-through zero state to the modified sinusoidal PWM (SPWM) technique was not needed. Nevertheless, the efficiency of the proposed inverter was discontented due to the high switch voltage stress on the switches (i.e., switching frequency of 20 kHz).

Carrier-based PWM was the commonly used PWM technique for qZSI to generate AC output voltage. To achieve shoot-through state, there are several existing carrier-based PWM technique, which known as simple boost control (SBC) [18], maximum boost control (MBC) [29] and maximum constant boost control (MCBC) [30]. Besides, space vector modulation (SVM) techniques were also investigated and provide different maximum shoot-through time intervals [31]. For instance, in 2014, a single-phase seven level qZCHI controlled with SVM was proposed in [2] and [32]. The results demonstrated the accomplishment of DC-link voltage balance among the cells and low THD of the grid-tie output voltage and current. Later, the work was extended to three-phase system, where all the positive outcomes from [2] was achieved in [32]. Nevertheless, detail of associated switching frequency was not reveal. Pulse width amplitude modulation (PAM), which was proposed in [33], shows that a reduction of up to 87% switching loss can be achieved. Moreover, PAM-based inverter can achieve higher power density with smaller footprint when compared with the mentioned modulation techniques.

In 2013, a comparison work between the phase-shifted amplitude PWM (PSA-PWM) and phase-shifted sinusoidal pulse width modulation (PS-SPWM) was demonstrated in [12]. It was concluded that the proposed technique greatly reduced the number of switching actions with lower switching frequency (i.e., 5 kHz). Therefore, reducing the switching loss for more than 50%. Later, to prevent any solar energy

harvesting issue, a modified modulation technique incorporated with a double-frequency ripple (DFR) suppression controller was proposed to lower down the DC input voltage DFR without using large capacitance [9]. The capacitance used in the qZSI was 10 times smaller than the conventional application. Nevertheless, proposed topology experienced higher power loss and the voltage stress across the switches (i.e., at switching frequency of 100 kHz) was increased by 53% when compared with conventional design.

2.4 Integration of novel topology to qZS network

Another novel topology of cascaded (two-stage) qZS network was proposed in [34, 35] to achieve extended voltage boost. When compared with classical qZS network, this topology was constructed with additional diode, inductor and two capacitors, which capable to lower the shoot-through duty cycle by 30% with the same voltage boost factor. However, this topology required complex controlling technique due to the interactive influence of one cascaded module to another.

In 2013, photovoltaic (PV) power generation based qZS cascaded H-bridge inverter (qZCHI) which utilized the enhancement mode gallium nitride (GaN) field effect transistors (FETs) was presented in [4] as an effort to enhance the efficiency and provide high power density at high switching frequency (i.e., 100 kHz). The outcome illustrated that a peak efficiency of 98.06% was able to attain with the modified sawtooth carrier modulation strategy, but with a drawback of requiring large inductor size to minimize the increased inductor current ripple due to the merged shoot-through period.

A high voltage gained isolated multistage DC-DC converter was presented in 2014. The topology composed of a qZS network connected to a push-pull square-wave inverter [36]. The output was connected to a voltage-doubler rectifier. Through experimental verification, the converter was able to produce a wide range of voltage gain using small duty cycle. Therefore, the proposed topology was suitable to be used in application, where a wide range of voltage gain was required especially in renewable energy generation, transportation sectors and telecommunication. In the study, a small turn ratio of isolated transformer was used. This greatly minimized the conduction losses and the structure size of the converter. Nevertheless, since the topology consists of multi-stages, the control system requirement is becoming more complex.

In 2015, a single-phase quasi switched boost H-bridge inverter (qSBI) which is suitable in low power renewable energy application was proposed [37]. The work illustrated a full comparison between qSBI and qZSI including the component selection (i.e., inductor and capacitor value), analyzation on the DC and AC component, current

and voltage stress on semiconductor, system efficiency and power loss calculation. The experiment results concluded that:

i. The inductance in qSBI and qZSI were the same whereas the capacitance of qZSI was four times higher than qSBI.
ii. qSBI had higher system efficiency than qZSI.
iii. qSBI had one extra active switch and diode, but its current rating of the diode and both the active switches were smaller than qZSI.
iv. The capacitor voltage stress of qSBI was higher than qZSI.
v. Even with the same parasitic effect, the qSBI's DC-link boost factor was higher than of qZSI.

2.5 DC-link voltage controller in qZSI

The qZSI network generates a non-minimum phase due to the right-hand plane zero in the transfer function. Therefore, it is difficult for conventional PI or proportional integral derivative (PID) controller to achieve good dynamic performance. Moreover, PI controller is unable to remove low-order harmonics due to bandwidth limitation [38]. To fulfil voltage boost and voltage inversion capabilities as well as MPPT control, the closed loop control system has to be carefully designed. For instance, H2/H∞ based optimal controller was proposed in [39] and it demonstrates better performance in tracking the changes in reference currents of the AC and DC-link voltage distribution. The proposed controller offered lower overshoot and attained more promising transient performance than PI controller. However, it cannot evaluate the robustness under exogenous disturbance and system parameter perturbations.

Proportional Resonant (PR) controller was proposed in several works as an alternative to replace PI controller in qZSI control system [38, 40]. PR-controller can provide high gain value for selected fundamental frequency and keeping other frequencies at low gain while conversely, the gain of the PI controller is limited by the gain at its resonant frequency and it introduces phase-shift to the output voltage. However, PR-controller is particularly used in grid-tie based transfer function rather than in DC-link voltage loop transfer function.

On the contrary, type-II compensator was used in [41] which demonstrated that the controller is able to reduce overshoot of the buck converter PWM generated output voltage during transient time. Lead compensator is one of the most commonly used technique in control system. The results in [13, 14] showed that lead compensator has outperformed PI and PID controller in controlling the speed of machine and robotic movement. However, yet no research has been conducted to develop voltage or current control loop using a lead compensator for qZSI. In 2015, a control scheme for an energy stored PV-based multilevel qZCHI based grid-tie power system was proposed [3]. An energy storing battery was added in each qZSI module to balance the stochastic fluctuation of PV solar power injected to the grid. The combination of MPPT and energy storing

battery ensured the grid to operate at maximum power. The author incorporated the proposed control scheme with 10 kHz PS-SPWM modulation technique. The experimental results show that MPPT was distributed throughout the PV-panels and power balanced was achieved between different PV-panels.

2.6 CCM and DCM of qZSI

The qZS network has the input inductor that buffers the current source of the network. Therefore, the qZS network can operate in CCM when the input current never drops to zero during shoot-through state. With CCM operation, the input voltage stress can be minimized. However, only few existing works had been done to demonstrate comprehensive mathematical analysis between DCM and CCM operating mode of the qZSI only [42, 43]. In this work, the boundary condition between the CCM and DCM in qZSI has been derived and the methods to avoid undesired DCM operation will also be discussed.

2.6 Active and reactive power compensation

Power quality and efficiency issues has been the major issue in power systems, resulted by low power factor voltage collapse, excessive harmonics etc. Voltage imbalance problems are one of the major treats to power quality and efficiency issues. It could be caused by a poor DC-link control system or induced by unbalanced output load or any unsymmetrical faults through the transmission lines. High reactive power in the system can cause high I^2R losses due to the high current presented in the circuit. Therefore, the incorporation of STATCOM system with DC-link voltage regulator is vital in providing a high efficiency output power. With VSC, the output voltage is increased, at the same time reducing the current level, therefore, reducing active power loss.

STATCOM which is usually applied for reactive power compensation, can also provide harmonic compensation and voltage regulation (i.e. D-STATCOM) [44]. There are two types of control methods in STATCOM system, namely the direct and indirect

current control methods. The direct current control takes the STATCOM as a voltage source and output the desired AC voltage wave phase that will indirectly control the AC current [45]. This method is simple, but it is imprecise and require a very long response time.

In a STATCOM system, PLL is commonly implemented in the system, which is based on positive-sequence bus voltage. PLL strategy obtained the phase angle from dq rotating coordinate by transforming the $\alpha\beta$ stationary coordinate system to the dq rotating coordinate system. In [44], the author proposed a STATCOM based five-level cascaded inverter controller and incorporated i_{oq} algorithm control scheme. The proposed control scheme is to provide indirect control to the AC current by obtaining the inner active and reactive currents from the abc-to-dq transformation block. Then, the controller can provide reactive power compensation control for different loading conditions. From [44], the controller maintained a stable active source current while provides positive leading reactive current which is used to cancel out the negative reactive source current.

2.7 Summary

To conclude this chapter, different type of qZS topology have been proposed by researchers, each consists of advantages and disadvantages. Besides, the performance of several modulation techniques was reviewed in this chapter. From the reviews, it has shown that PS-SPWM can greatly reduce the number of switching actions even with lower switching frequency. Moreover, PS-SPWM is the only sinusoidal based PWM method that can generate multilevel output voltage/current. Moving on to the qZSI control system, knowing that qZS network generates a non-minimum phase due the existence of right-hand plane zero; the controller is difficult to provide a superior transient response in the qZSI output voltage. Therefore, it is utmost important to select a controller that can provide excellent dynamic and transient response when the system is dominated with a non-minimum phase. The performance comparison between several controllers has been reviewed. This includes the comparison between the most commonly used controller (i.e., PI and PID controller) with different type of linear/non-linear controller (i.e., H2/H∞ controller, PR-controller, type-II controller and lead compensator). Lastly, attention has been paid to the operating mode of qZSI; with CCM and DCM. This part plays an important role when qZSI is subjected to major change in system parameters during contingency events (i.e., change in duty cycle, input voltage etc.).

Chapter 3 : CCM, boundary condition and DCM analysis of qZSI

This chapter presents a working model of qZSI together with detail mathematical derivation of the transfer function that characterizes qZSI in both CCM and DCM. Furthermore, the mathematical equation to distinguish between boundary condition, CCM and DCM have been derived. The equations are used to determine the selection of the size of passive component (i.e., inductor) to construct the qZS network in the next chapter. Also, this chapter introduces the parameters that have a direct impact on the operating mode of qZSI.

This chapter discusses the following: Section 3.1.1 describes the equations and characteristics of qZSI in CCM and DCM. This includes the analysis and derivation of the equation to characterize each voltage and current present in the network. Besides, this section also includes the derivation of qZSI input-output transfer function in CCM and DCM. Section 3.1.2 describes the impact of CCM and DCM on the input current and output voltage. The transition boundary condition of CCM to DCM also covered in this section. This includes the relationship between the operating mode of qZSI with inductor value, switching frequency and shoot-through duty ratio. Lastly, section 3.3 covers the simulation to verify the derived equations in section 3.1 and section 3.2.

3.1 Mathematical derivation of qZSI's characteristic and transfer function

QZSI was derived by adding two inductors, two capacitors and one diode to the traditional inverter topology to allow voltage boost functions in a single-stage. qZSI topology features advantages such as continuous input current, excellent reliability and most importantly, it allows low inrush start-up current. Figure 3.1 shows the qZS topology attached to H-bridge inverter that has been introduced to replace the traditional ZSI topology. By introducing a special shoot-through state, magnetic energy will be stored in the inductor L_1 and L_2 during this state without short-circuiting the DC capacitor C_1 and C_2. If the input voltage of the qZSI is high enough, the topology starts to operate as traditional VSI.

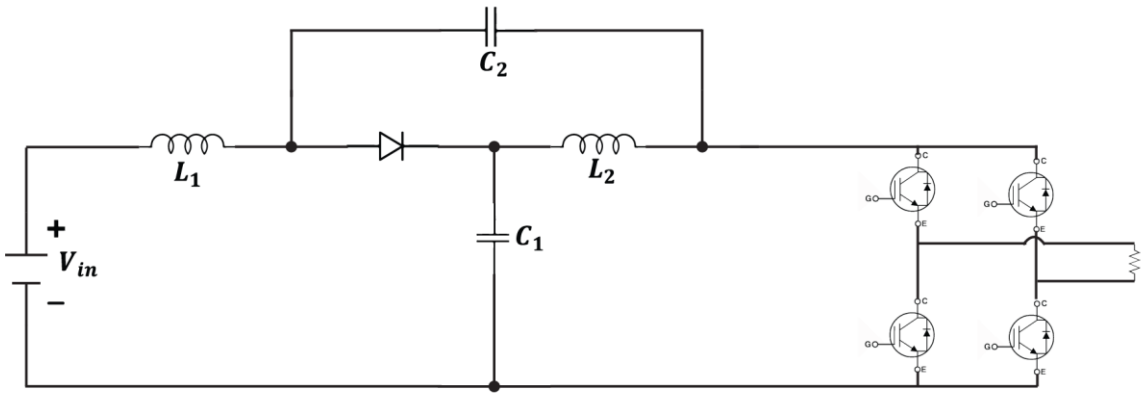

Figure 3.1: qZSI with H-bridge

In Figure 3.2, V_{L1} and V_{L2} represent the voltage of inductor L_1 and L_2 respectively; I_{L1} and I_{L2} represent the current that flow through inductor L_1 and L_2 respectively. V_{C1} and V_{C2} represent the voltage across capacitor C_1 and C_2. I_{C1} and I_{C2} represent the current of capacitor C_1 and C_2. V_{DC} represents the DC-link voltage at the output side of the qZSI topology. I_{DC} represents the DC-link current generated at the output side of qZSI topology. Lastly, I_{diode} and V_{diode} represent the current and voltage of the diode respectively.

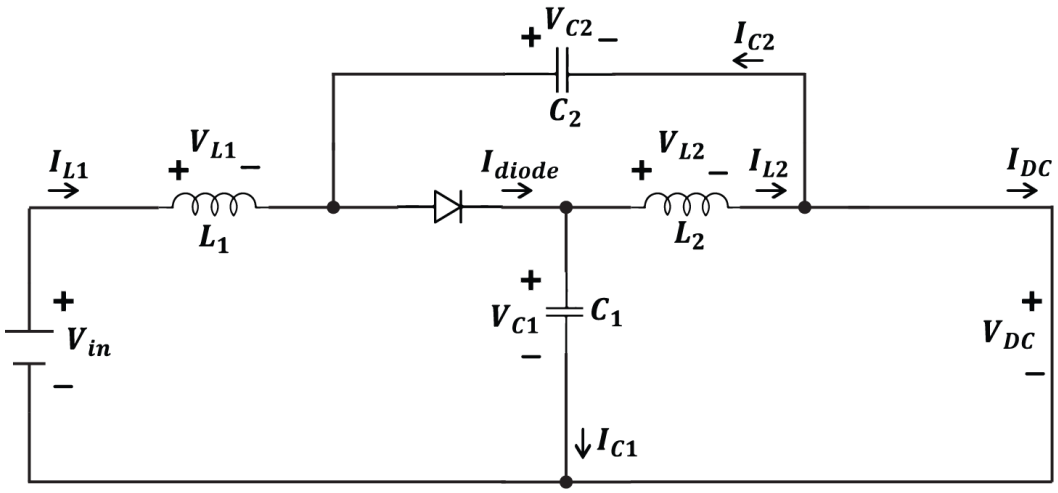

Figure 3.2: qZSI topology

3.1.1 Mathematical deviation of qZSI in CCM

qZSI topology can concurrently drive up the input voltage and invert the DC-voltage into AC output voltage. In CCM, qZSI operates in three different operating modes which include shoot-through state, non-shoot-through state (consists of active-state and null state). Figure 3.3(a) and Figure 3.3(b) show the equivalent circuits of qZSI in shoot-through and active-state respectively. To obtain a better view and understanding of qZSI operation in shoot-through and null state, the qZSI model in Figure 3.3 are redrawn and shown in Figure 3.4(a) and Figure 3.4(b) respectively.

As seen in Figure 3.2, qZSI topology input side is connecting in series with an inductor. This inductor acts as buffer for the current source. In other words, in continuous conduction mode (CCM), the input current (i.e., I_{L1}) will never falls to zero, no matter in shoot-through or non-shoot-through state, featuring a reduce stress topology for converter application. However, in the case of large load, low boost factor, small inductor value and low switching frequency, qZSI could operates in the discontinuous conduction mode (DCM). When the qZSI operates in this mode, the input current falls to zero during the discontinuous conduction interval and resulting in increasing voltage and current stress.

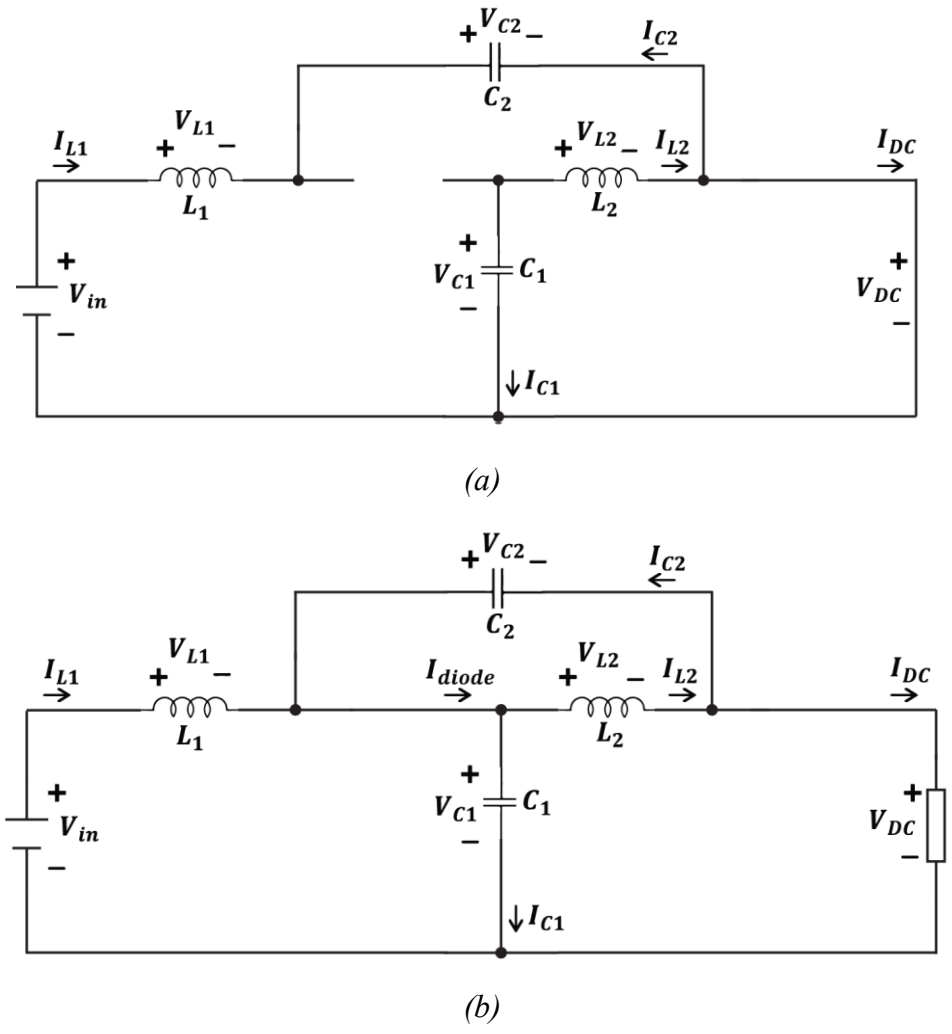

Figure 3.3: Equivalent circuit of qZSI (a) shoot-through state (b) active-state

Particularly, when qZSI topology operates in shoot-through state (i.e., Figure 3.3(a)), either one or two phase-leg of the inverter are short-circuited to form two active loops. In conventional inverter, short-circuit will cause the output current of the inverter to become very large and destroy the components in the entire circuit. However, in qZSI, due to the presence of inductor and capacitor, the short-circuited event allows the current to remain low and prevent the current throughout the entire topology to turn into infinite value. In shoot-through state, one complete loop is attained through input voltage V_{in}, capacitor C_2 and inductor L_1, and resulting in the charge up process of inductor L_1. Meanwhile, the other loop is formed through capacitor C_1 and inductor L_2 to charge up L_2.

During active-state, the high side and low side of the IGBT in the same phase-leg are switched on and off simultaneously; the diode forward biased. In this state, the capacitor C_1 voltage discharge through inductor L_2 and thus providing more current to flow through the output load. In other words, boosting mechanism occurs during active-state and it works as conventional voltage-source inverter (VSI) without employing any dead-time.

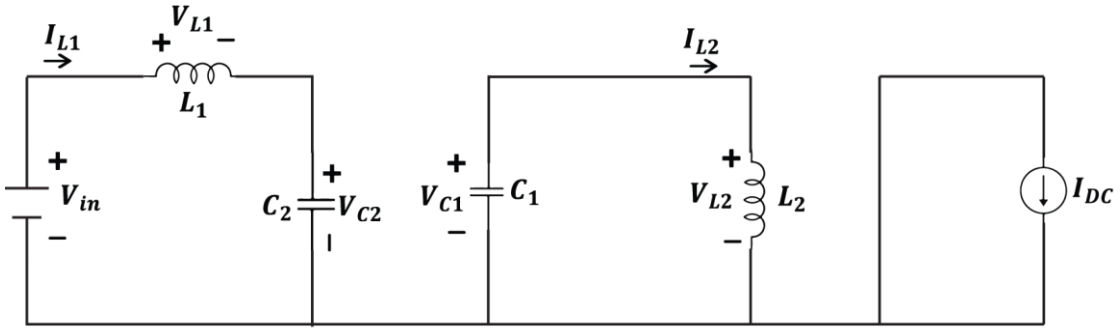

(a)

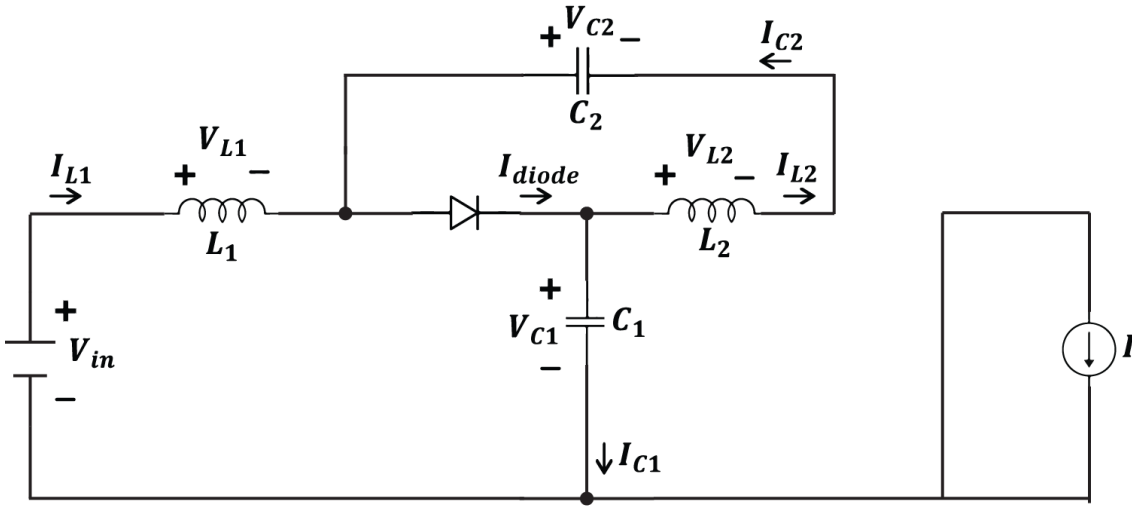

(b)

Figure 3.4: Equivalent operation modes for qZSI (a) shoot-through state (b) null state

Null state happens when both the IGBT at the lower and upper phase-legs are turned on at the same time. During this state, the H-bridge inverter is disconnected from the qZSI impedance network; causing the current flows through inductor L_2 to recharge capacitor C_2 while the current flows through inductor L_1 to charge capacitor C_1

concurrently. The mathematical equations of qZSI in shoot-through state can be defined as follows:

$$I_{C1} = -I_{L2} \tag{3.1}$$

$$I_{C2} = -I_{L1} \tag{3.2}$$

$$V_{L1} = V_{in} + V_{C2} \tag{3.3}$$

$$V_{L2} = V_{C1} \tag{3.4}$$

$$I_{DC} = I_{L1} + I_{L2} \tag{3.5}$$

$$V_{DC} = 0 \tag{3.6}$$

The state space equation of shoot-through state in steady-state of qZSI is derived as follows:

$$\begin{bmatrix} L_1 & 0 & 0 & 0 \\ 0 & L_2 & 0 & 0 \\ 0 & 0 & C_1 & 0 \\ 0 & 0 & 0 & C_2 \end{bmatrix} \begin{bmatrix} \dot{\imath_{L1}}(t) \\ \dot{\imath_{L2}}(t) \\ \dot{v_{C1}}(t) \\ \dot{v_{C2}}(t) \end{bmatrix} = \begin{bmatrix} 0 & 0 & 0 & 1 \\ 0 & 0 & 1 & 0 \\ 0 & -1 & 0 & 0 \\ -1 & 0 & 0 & 0 \end{bmatrix} \begin{bmatrix} i_{L1}(t) \\ i_{L2}(t) \\ v_{C1}(t) \\ v_{C2}(t) \end{bmatrix} + \begin{bmatrix} 1 & 0 \\ 0 & 0 \\ 0 & 0 \\ 0 & 0 \end{bmatrix} \begin{bmatrix} v_{in}(t) \\ i_{DC}(t) \end{bmatrix} \tag{3.7}$$

The mathematical equations of qZSI in active-state can be defined as follows:

$$I_{C1} = I_{L1} - I_{DC} \tag{3.8}$$

$$I_{C2} = I_{L2} - I_{DC} \tag{3.9}$$

$$V_{L1} = V_{in} - V_{C1} \tag{3.10}$$

$$V_{L2} = -V_{C2} \tag{3.11}$$

$$I_{diode} = I_{C1} + I_{L2} \tag{3.12}$$

$$I_{diode} = I_{L1} + I_{L2} - I_{DC} \tag{3.13}$$

$$V_{DC} = V_{C1} + V_{C2} \tag{3.14}$$

$$I_{DC} = I_o \tag{3.15}$$

The state space equation of active-state in steady-state of qZSI is derived as per (3.16):

$$\begin{bmatrix} L_1 & 0 & 0 & 0 \\ 0 & L_2 & 0 & 0 \\ 0 & 0 & C_1 & 0 \\ 0 & 0 & 0 & C_2 \end{bmatrix} \begin{bmatrix} \dot{\iota_{L1}}(t) \\ \dot{\iota_{L2}}(t) \\ \dot{v_{C1}}(t) \\ \dot{v_{C2}}(t) \end{bmatrix} = \begin{bmatrix} 0 & 0 & -1 & 0 \\ 0 & 0 & 0 & -1 \\ 1 & 0 & 0 & 0 \\ 0 & 1 & 0 & 0 \end{bmatrix} \begin{bmatrix} i_{L1}(t) \\ i_{L2}(t) \\ v_{C1}(t) \\ v_{C2}(t) \end{bmatrix} + \begin{bmatrix} 1 & 0 \\ 0 & 0 \\ 0 & -1 \\ 0 & -1 \end{bmatrix} \begin{bmatrix} v_{in}(t) \\ i_{DC}(t) \end{bmatrix} \tag{3.16}$$

Throughout one switching cycle, the average equation of capacitor current (i.e., I_{C1} and I_{C2}) and inductor voltage (i.e., V_{L1} and V_{L2}) are equate to zero. Solving the equation, we get:

$$I_{L1} = I_{L2} \tag{3.17}$$

$$V_{in} = V_{C1} - V_{C2} \tag{3.18}$$

$$\frac{V_{C1}}{V_{in_{ccm}}} = \frac{1 - D_{ST}}{1 - 2D_{ST}} \tag{3.19}$$

$$\frac{V_{C2}}{V_{in_{CCM}}} = \frac{D_{ST}}{1 - 2D_{ST}} \tag{3.20}$$

$$B_{CCM} = \frac{V_{DC}}{V_{in_{CCM}}} = \frac{1}{1 - 2D_{ST}} \tag{3.21}$$

$$B_{CCM} = \frac{V_{C1}}{V_{in} * (1 - D_{ST})} \tag{3.22}$$

$$\frac{V_{DC}}{V_{C1_{CCM}}} = \frac{1}{1 - D_{ST}} \tag{3.23}$$

Where B_{CCM} represents the boost factor of qZSI in CCM. D_{ST} represents the shoot-through duty ratio and its value should be smaller than 0.5 to prevent unpredictable output voltage generation. Equating shoot-through duty ratio to 0.5 will cause the denominator of equation (3.21) to become zero, resulting in an infinite boost factor of qZSI.

3.1.2 Mathematical deviation of qZSI in DCM

Figure 3.5(a) shows the operating mode of qZSI in DCM mode. By rearranging the circuit for better view and understanding, the circuit is redrawn and shown in Figure 3.5(b). During this state, there is a certain interval where the diode in qZSI topology stops to conduct. DCM takes place during non-shoot-through state. In DCM, non-shoot-through state can be split into three different operating states (i.e., active-state, null state and discontinuous conduction state). As discussed in section 3.1.1 above, similar to CCM mode, null state in DCM occurs when both the IGBT at the lower and upper phase-legs are turned on simultaneously. In active-state, the diode supposed to be forward biased, but when DCM occurs, the diode will be turned off during this entire interval. DCM occur when the inductor magnetic field (or current) has fully discharged before the next shoot-through interval occurs.

The reason that cause DCM to occur is due to the inability of the inductor to stay charged during the entire non-shoot-through state. Normally, DCM occurs when the inductor value used is too small; small inductor can only store a limited amount of charge and it will be fully discharged before the next switching interval. Hence, in section 3.2, the mathematical equations to reflect the right inductor size for specific systems parameter are being derived.

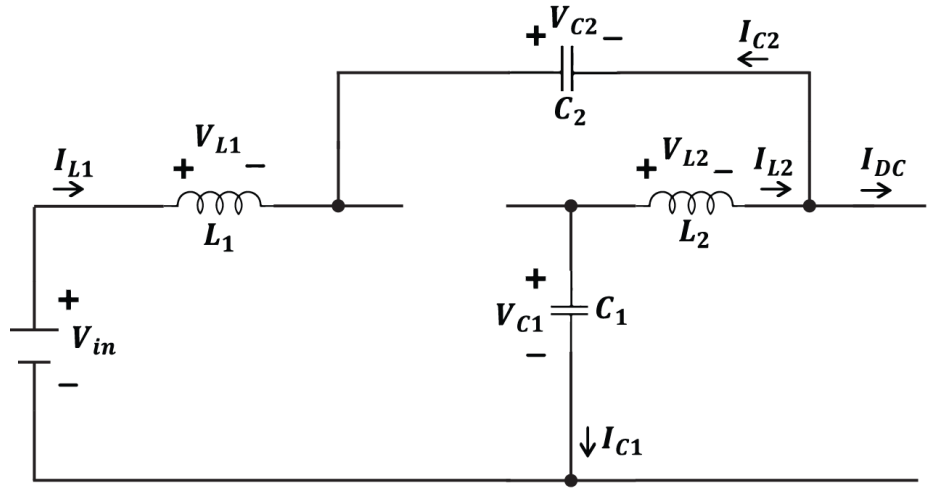

(a)

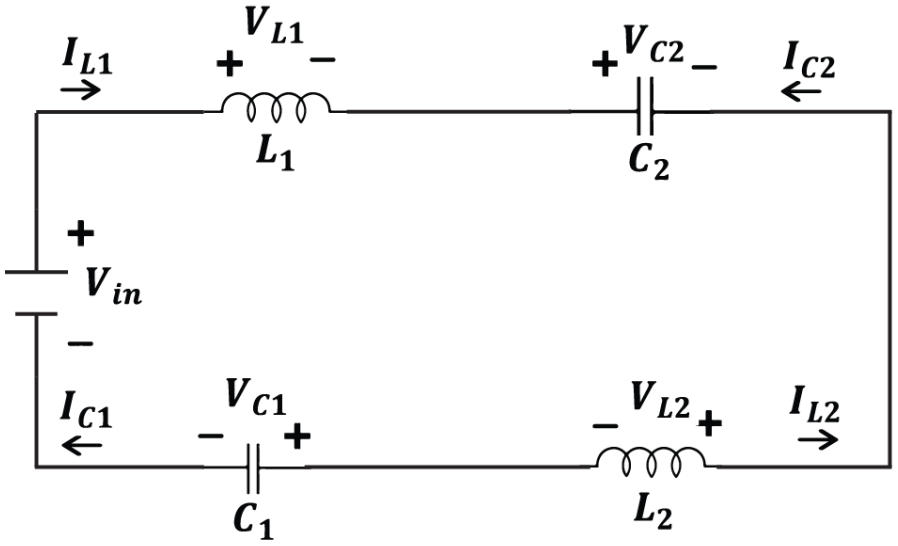

(b)

Figure 3.5: Equivalent operation modes (a) DCM (b) rearrange view of DCM

In shoot-through state, the mathematical equation of the qZSI operation can be defined as follows:

$$V_{L1} = V_{in} + V_{C2} \tag{3.24}$$

$$V_{L2} = V_{C1} \tag{3.25}$$

In active-state, the mathematical equation of the qZSI operation can be defined as follows:

$$V_{L1} = V_{in} - V_{C1} \tag{3.26}$$

$$V_{L2} = -V_{C2} \tag{3.27}$$

By using equation (3.26) and (3.27), the average equation of inductor voltage V_{L1} is shown as follows:

$$\langle V_{L1} \rangle = (V_{in} + V_{C2})D_{ST} + (V_{in} - V_{C1})(1 - D_{ST} - D_D) + 0(D_D) \tag{3.28}$$

D_D can be defined as the duty ratio of the DCM.

Substitute: $V_{in} = V_{C1} + V_{C2}$ into the above equation. The average equation of V_{L1} over on switching cycle is equal to zero. Thus,

$$\langle V_{L1} \rangle = 0$$

$$0 = (V_{in} + V_{C1})(D_{ST}) + (V_{in} - V_{C1})(1 - D_{ST} - D_D)$$

Solving the equation, get:

$$\frac{V_{C1}}{V_{C2}} = \frac{1 - D_{ST} - D_D}{D_{ST}} \tag{3.29}$$

From (3.18), in active-state

$$V_{in} = V_{C1} - V_{C2}$$

$$V_{C2} = V_{C1} - V_{in} \tag{3.30}$$

Substitute equation (3.18) into equation (3.29), we get,

$$\frac{V_{C1}}{V_{C1} - V_{in}} = \frac{1 - D_{ST} - D_D}{D_{ST}}$$

$$V_{C1} = \frac{1 - D_{ST} - D_D}{D_{ST}} V_{C1} - \frac{1 - D_{ST} - D_D}{D_{ST}} V_{in}$$

$$\left(\frac{V_{C1}}{V_{in}}\right)_{DCM} = \frac{1 - D_{ST} - D_D}{1 - (2D_{ST} + D_D)} \tag{3.31}$$

Substitute equation (3.30) into equation (3.31), we get

$$\frac{(1 - D_{ST} - D_D)V_{C2}}{V_{in}} = \frac{1 - D_{ST} - D_D}{1 - (2D_{ST} + D_D)}$$

$$\frac{V_{C2}}{V_{in}} = \frac{D_{ST}}{1 - (2D_{ST} + D_D)} \tag{3.32}$$

From equation (3.14), DC-link voltage in active-state can be written as:

$$V_{DC} = V_{C1} + V_{C2}$$

Substituting equation (3.14) into equation (3.32) above, we get:

$$V_{DC} = \left[\frac{1 - (D_{ST} - D_D)}{1 - (2D_{ST} + D_D)} + \frac{D_{ST}}{1 - (2D_{ST} + D_D)}\right] V_{in} \tag{3.33}$$

Therefore, in DCM mode, the DC-link to input voltage transfer function can be written as:

$$\frac{V_{DC}}{V_{in}} = \frac{1 - D_D}{1 - (2D_{ST} + D_D)} \tag{3.34}$$

The boost factor of qZSI topology in DCM mode can be written as:

$$B_{DCM} = \frac{V_{DC}}{V_{in}} = \frac{V_{C1}}{V_{in}} + \frac{V_{C2}}{V_{in}} \tag{3.35}$$

By rearranging equation (3.31) the discontinuous conduction duty ratio equation is obtained via (3.36) below:

$$D_D = \frac{\left(V_{C1} - V_{in} + D_{ST}(V_{in} - 2V_{C1})\right)}{V_{C1} - V_{in}} \tag{3.36}$$

3.2 Mathematical derivation to distinguish qZSI in boundary condition, CCM and DCM

Figure 3.6 shows inductor voltage (V_{L1}, V_{L2}) and inductor current (I_{L1}, I_{L2}) waveforms during CCM. Notice when the system is in CCM, the inductor current will never fall to zero. Based on inductor's volt-second balance and capacitor's ampere-second balance rules, the inductor current cannot change instantaneously in transition of shoot-through state to non-shoot-through state. Therefore, the average value of inductor voltage in one switching cycle is equal to zero.

The shoot-through characteristic of the qZSI will render a ripple effect on the inductor current because the inductor charges (during shoot-through state) and discharge (during non-shoot-through state) in one switching cycle. The ripple current amplitude flowing through the inductor L_1 and L_2 are denoted as ΔI_{L1} and ΔI_{L2} respectively, as shown in the Figure 3.6 below.

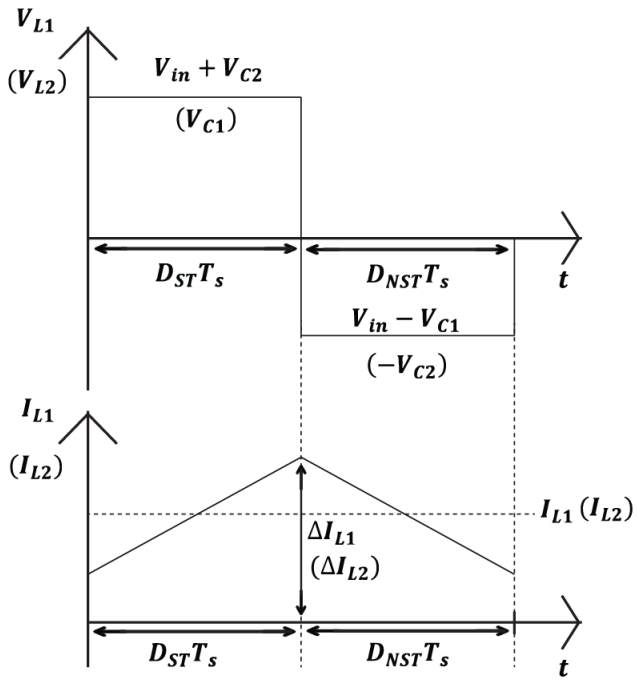

Figure 3.6: Inductor voltage and current waveform in CCM

In CCM, the inductor current continuously forming an upward and downward adjoining line; seeming like a triangular shaped graph. The boundary condition formed when the system is about to turn into DCM; called it as BCM. In this transition state, the ripple inductor current falls upon touching the x-axis; the inductor waveform may touch the zero line for a short instance or slightly higher than zero line. The trailing statements are shown in Figure 3.7.

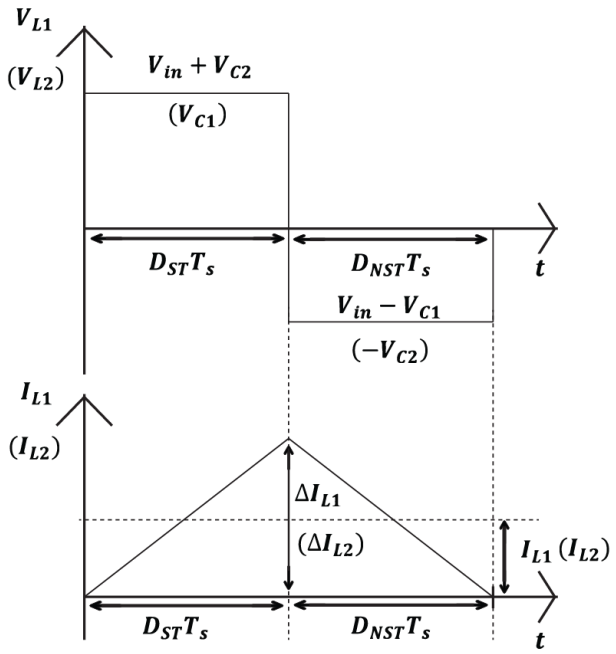

Figure 3.7: Inductor voltage and current waveform in BCM

The equation for ΔI_{L1} and ΔI_{L2} are obtained as in equation (3.37) and (3.38), where L denotes the inductance and f_s represents the switching frequency.

$$\Delta I_{L1} = \frac{1}{L}\int_{t=0}^{t=D_{ST}T_s} V_{L1}\,dt = \frac{1}{L}\int_{D_{ST}T_s}^{T_s} V_{L1}\,dt$$

$$\Delta I_{L1} = \frac{(V_{in} + V_{C2})(D_{ST})}{Lf_s} \tag{3.37}$$

$$\Delta I_{L2} = \frac{1}{L}\int_{t=0}^{t=D_{ST}T_s} V_{L2}\,dt = \frac{1}{L}\int_{D_{ST}T_s}^{T_s} V_{L1}\,dt$$

$$\Delta I_{L2} = \frac{(V_{C1})(D_{ST})}{Lf_s} \tag{3.38}$$

Based on Figure 3.7 above, the boundary inductor current, I_{LB} is half the amplitude of the ripple current as the waveform formed is a triangular shaped. Therefore, the boundary current, I_{LB} can be written as follows:

$$I_{LB} = \frac{1}{2}\Delta I_L \tag{3.39}$$

In section 3.1, it was proven that when the inductor value used in qZSI topology is the same, $I_{L1} = I_{L2}$ in steady-state. Hence, by substituting equations (3.37) and (3.38) into equation (3.39), the boundary current of L_1 and L_2 can be derived as per equation (3.40)

$$I_{LB1} = I_{LB2} = \frac{(V_{in} + V_{C2})(D_{ST})}{2Lf_s} = \frac{(V_{C1})(D_{ST})}{2Lf_s} \tag{3.40}$$

The power converter operates in CCM when $I_L \geq I_{LB}$ and in DCM when $I_L < I_{LB}$. Therefore, to ensure the qZSI to operate in CCM, the following equations must be fulfilled.

$$I_{LB} \geq \frac{(V_{in} + V_{C2})(D_{ST})}{2Lf_s} \; or \; I_{LB} \geq \frac{(V_{C1})(D_{ST})}{2Lf_s} \tag{3.41}$$

Rearranging the equation, we get

$$L \geq \frac{(V_{in} + V_{C2})(D_{ST})}{2I_{LB}f_s} \; or \; L \geq \frac{(V_{C1})(D_{ST})}{2I_{LB}f_s} \tag{3.42}$$

Equation (3.42) indicates the minimum inductor value to be selected to achieve CCM based on switching frequency, shoot-through duty ratio and the output load.

Figure 3.8 shows the inductor voltage and current waveform when qZSI operating in DCM. D_D represents the DCM duty ratio. Assuming 100% efficiency of qZSI topology, the input power would be equal to output power.

$$P_{out} = P_{in} \tag{3.43}$$

Where P_{out} is the output voltage and P_{in} is the input voltage.

$$V_{in}I_{L1} = V_{o_{rms}} * I_{o_{rms}} = \frac{V_{DC}}{\sqrt{2}} * \frac{I_o}{\sqrt{2}} \tag{3.44}$$

Where $V_{o_{rms}}$ and $I_{o_{rms}}$ are the root mean square AC output voltage and current, respectively, and I_o is the peak AC output current.

Solving the equation, we get

$$I_o = \frac{2V_{in}I_L}{V_o} \tag{3.45}$$

The inductor current can be defined by the following equation (3.46), where the derivation can be found in Appendix A.

$$I_{L1} = \frac{1 - D_{ST}}{1 - 2D_{ST}} I_o \tag{3.46}$$

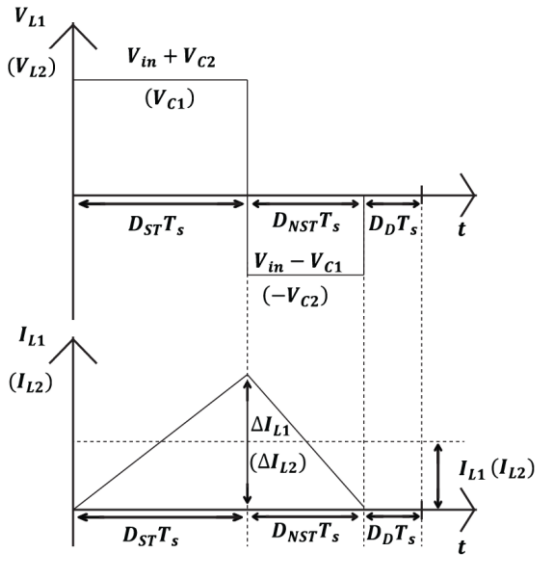

Figure 3.8: Inductor voltage and current waveform in DCM

Substitute equation (3.21) (i.e., $V_o = V_{DC} = \frac{1}{1-2D_{ST}}$) and equation (3.46) into equation (3.45), we get

$$I_o = \frac{D_{ST}(1 - D_{ST})V_{in}}{2Lf_s} \tag{3.47}$$

$$I_{OB} = \frac{D_{ST}(1 - D_{ST})V_{in}}{2Lf_s} \tag{3.48}$$

Where I_{OB} is the boundary output current at which qZSI starts to change from CCM to DCM.

By rearranging equation (3.48), we get equation as per (3.49) to justify the graph shown in Figure 3.9. The blue line shown in Figure 3.9 is the CCM-DCM boundary transition for the qZSI topology in steady-state.

$$\frac{Lf_s I_{OB}}{V_{in}} = D_{ST} - D_{ST}^2 \tag{3.49}$$

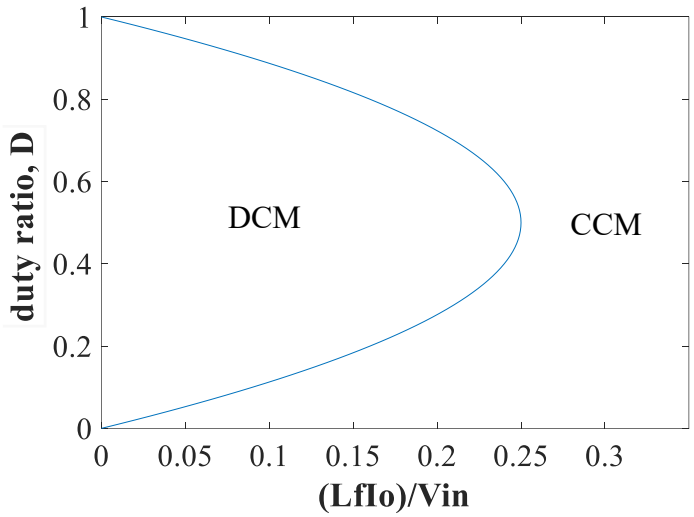

Figure 3.9: DCM and CCM Boundary Transition for qZSI

Based on equation (3.41), equation (3.48) and Figure 3.9, other than the inductor value, qZSI also shows direct impact to the duty ratio and the switching frequency of the system. When the switching frequency is increasing, the interval between each consecutive cycle decreases, the inductor will not likely to be fully discharged before end of one switching cycle. On the other hand, higher duty ratio indicates that the inductors are charged for a longer period and hence it can store more charges. Moreover, the shoot-through time interval increases as duty cycle increases, non-shoot-through state interval will be reduced in proportional. Hence, the time taken for the inductor to discharge reduces, preventing the qZSI to strike into DCM.

Figure 3.10 shows the typical comparison waveform of V_{DC} in CCM and DCM. From previous session, we know that the DC-link voltage in shoot-through state is zero when the upper IGBT of each phase-leg is turned on. In active-state, the DC-link voltage in CCM can be determined using equation (3.21).

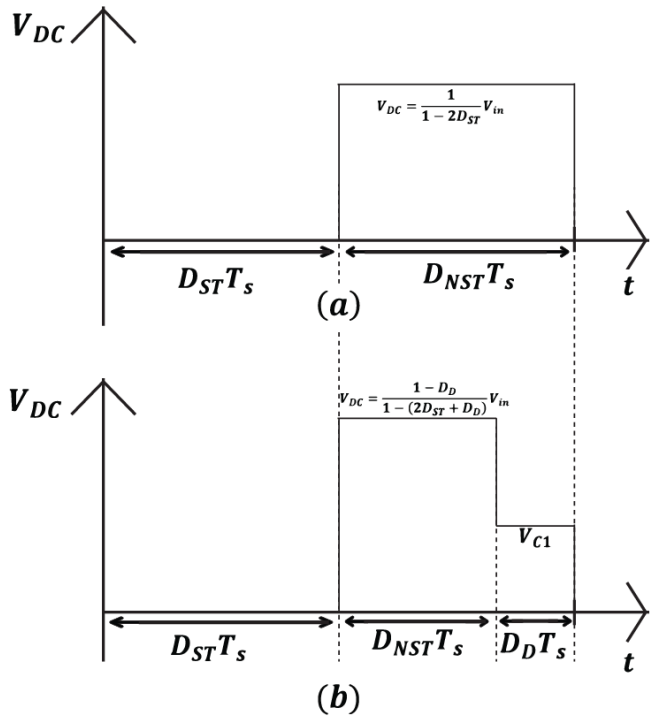

Figure 3.10: Comparison between DC-link voltage in (a) CCM and (b) DCM

In DCM, there are three sub-operating state occurred during the non-shoot-through state interval (i.e., active-state, null state and discontinuous conduction state). However, the null state does no impact to V_{DC} in both CCM and DCM. During active-state, V_{DC} can be calculated using equation (3.34). By referring to Figure *3.5*, the output IGBT and load circuit are disconnected from the input qZS circuit. Hence, during DCM, DC-link voltage will reduce to capacitor 1's voltage, V_{C1}, as shown in Figure 3.10. Note that D_D depends on the amount of time the inductor left uncharged (i.e., inductor current remains zero) before the next shoot-through state. Equation (3.34) shows that as the time taken for discontinuous conduction state increases, the output voltage will increase in proportional. Therefore, when the inductor remains discharged for longer period, the DC-link voltage will become higher during the next active-state.

3.3 Simulation results to verify the derived equation in CCM, BCM and DCM

This section discusses the Matlab/Simulink simulation results to verify the mathematical equation that distinguish the boundary condition between CCM and DCM derived in section 3.1 and section 3.2. Section 3.3 can be categorized into 2 parts; section 3.3.1 consists of the simulation model to determine the inductor value used in qZSI to achieve CCM, BCM and DCM follow by section 3.3.2 which demonstrates the relationship between load and the operating mode of qZSI.

3.3.1 Selection of passive component (inductor)

In this simulation model, several inductor values have been tested to verify the mathematical equation being derived. This section was developed to determine the minimum inductor value required to achieve CCM. The IGBT switching method was performed using SPWM. The system parameters used for simulations are listed in Table 3.1. The fundamental period of this simulation model was selected as $0.02s$. The inductors and capacitors used in qZSI are assumed to be equal value. (i.e., $L_1 = L_2$ and $C_1 = C_2$).

In this work, V_{in} is arbitrarily chosen as $12V$ and the shoot-through duty ratio was chosen to be 0.4 to yield an output DC-link voltage of $60V$. The minimum inductor value to allow the system to stay in CCM was calculated based on equation (3.42). Based on the equation and the system parameters listed in Table 3.1, the theoretical inductor value for the qZSI system to achieve CCM was calculated to be $2e^{-4}H$. In other words, to achieve CCM, the minimum inductor value must be greater or equal to the theoretical value calculated. Please note that there is a $\pm 5\%$ deviation of the simulation result as the equations are derived based on ideal cases.

Table 3.1: System parameters to verify minimum inductor value used to achieve CCM

Input voltage, V_{in}	$12V$
Desired DC-link output voltage, V_{DC}	$60V$
Capacitor C_1 and C_2 value	$1000\mu F$
Switching frequency, f_s	$10kHz$
Shoot-through duty ratio, D_{st}	0.4
Modulation index, M	0.5
Load resistance, Ω	50Ω
System AC output frequency, f_{AC}	$50Hz$

The capacitor value is determined by using a second harmonic $(2w)$ suppression formula, indicates in equation (3.50). a represents the DC-link voltage peak-to-peak ripple ratio and b represents the inductor current ripple.

$$C = \frac{MI_a(1 - 2D_{ST})}{awV_{in}}[bcos\emptyset + 1] \tag{3.50}$$

Figure 3.11(a) and (b) show the inductor current (I_{L1}) and DC-link voltage (V_{DC}) waveform in DCM respectively. The inductance value of the inductor used in this case is $0.5e^{-4}H$. As can be seen from the graph, both V_{DC} and I_{L1} values are higher than expected value in CCM. When DCM occurs, the output DC-link voltage will be deviated from the theoretical value. However, the peak value of DC-link voltage can be verified using equation (3.34). And noticed that there is a slight delayed when DC-link voltage reacts to discontinuous conduction state compare to inductor current. It is because the operating mode of qZSI solely depends on the charging and discharging capacity of the inductor itself. DCM occurs when the inductor has fully discharged before the end of each switching cycle. In Figure 3.11(b), when qZSI turns into DCM, the inductor current drop to zero and remains zero until the next shoot-through state happens. On the other hand, the DC-link voltage drops from $80V$ to $43V$ during this interval.

Figure 3.12 and Figure 3.13 show I_{L1} and V_{DC} waveform in BCM and CCM respectively. The inductor value used in Figure 3.12 is $2e^{-4}H$, while the inductor value used in Figure 3.13 is $3e^{-4}H$. By comparing Figure 3.11, Figure 3.12 and Figure 3.13, noticed that the peak inductor current, I_L become lower as the qZSI topology transformed from DCM to BCM to CCM. Besides, the minimum inductor current is further away from zero as the qZSI switch from DCM to BCM and to CCM. In other words, as the inductor value increases, the inductor tends to carry on with more charges. Hence, large inductor values tend to stay charged for a longer period, preventing qZSI to turn into DCM. On the other hand, since the difference between the maximum and minimum inductor current become smaller with increasingly inductor value, the current stress for the qZSI topology can be reduced in proportional.

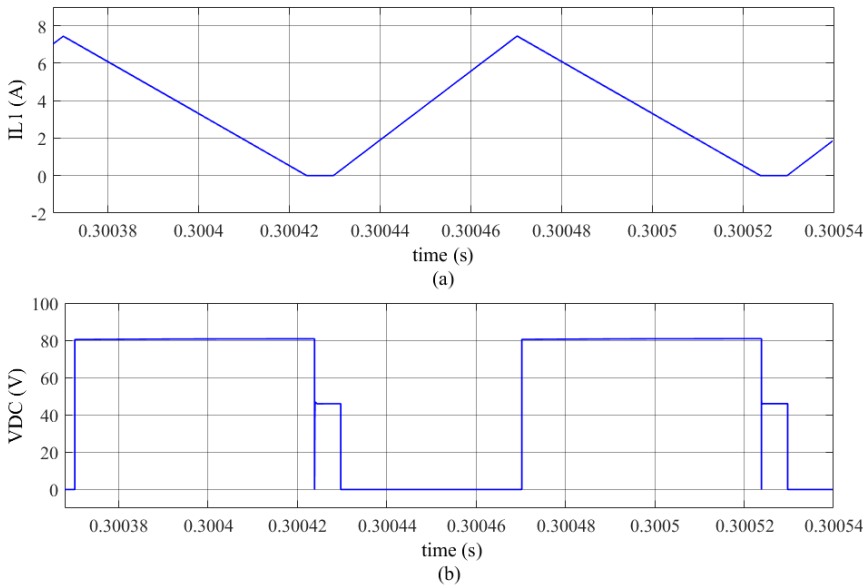

Figure 3.11: (a) I_{L1} and (b) V_{DC} in DCM

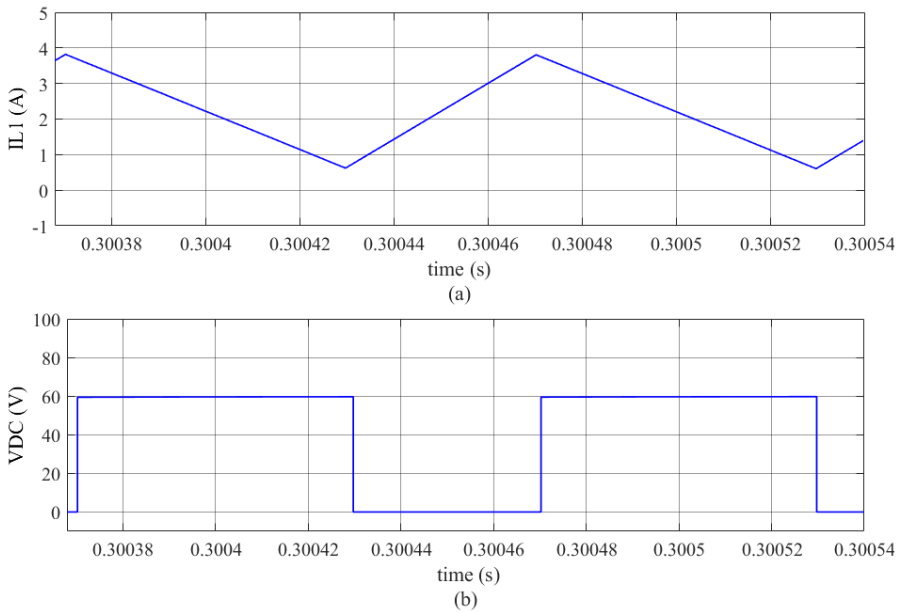

Figure 3.12: (a) I_{L1} and (b) V_{DC} in BCM

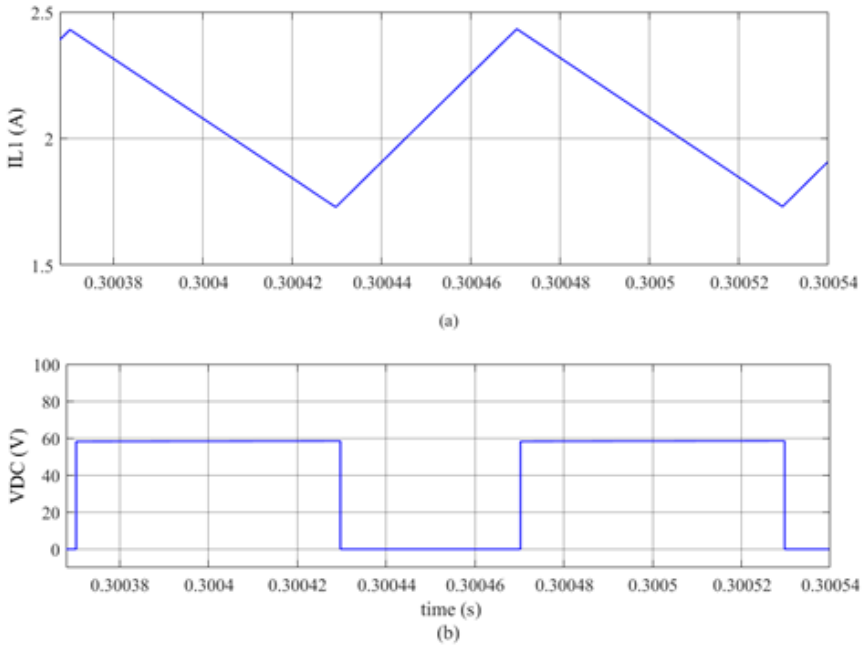

Figure 3.13: (a) I_{L1} and (b) V_{DC} in CCM

Figure 3.14 and Figure 3.15 show the DC-link output current (I_{DC}) waveform and inductor voltage (V_L) waveform in DCM, BCM and CCM, respectively. As predicted from the previous results, DC-link current and the inductor voltage value is expected to be highest when the qZSI is operating in DCM.

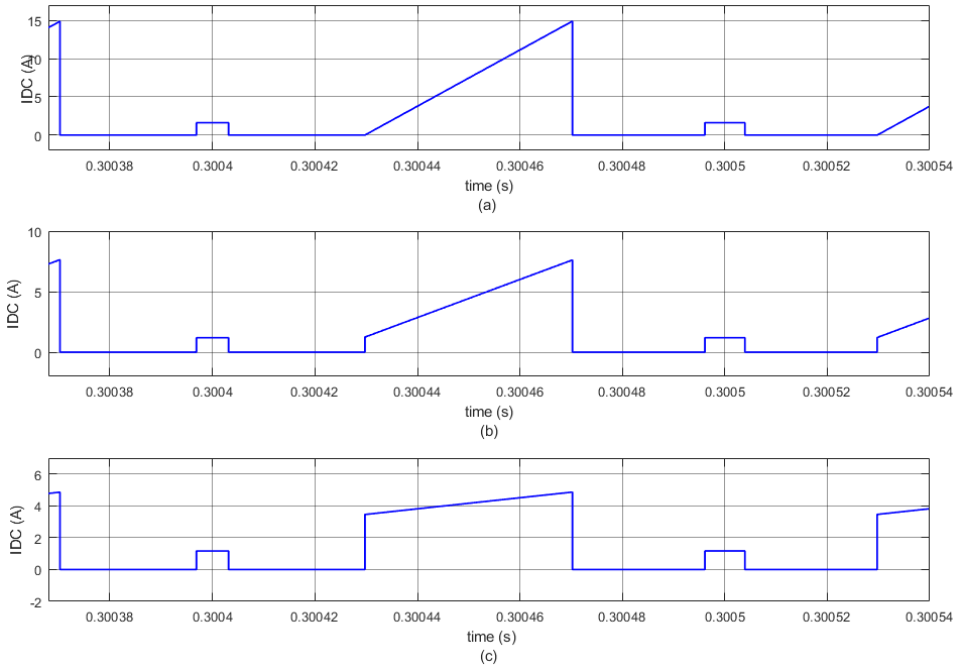

Figure 3.14: I_{DC} in (a) DCM (b) Boundary condition (c) CCM

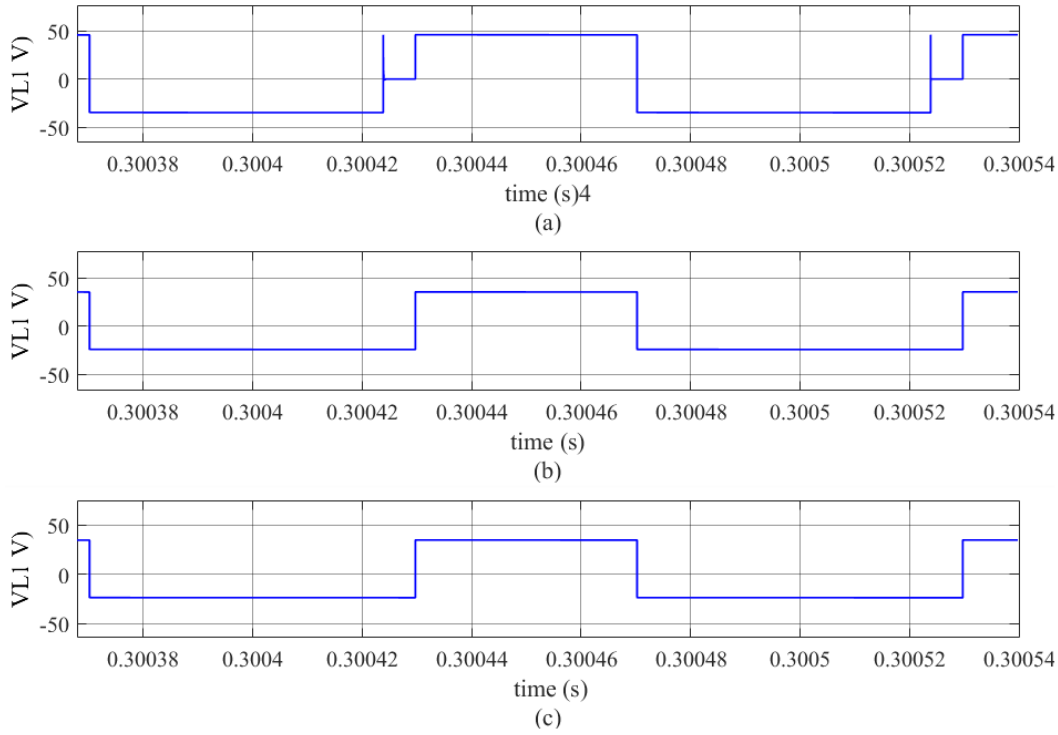

Figure 3.15: V_{L1} in (a) DCM (b) Boundary condition (c) CCM

3.3.2 Verification of boundary condition through varied load

The simulation model has been done to investigate the relationship between the output load with the operating mode of qZSI. This simulation model has been conducted to verify the equation (3.48). From the previous section (i.e., section 3.3.1), the minimum inductor value to achieve CCM is calculated to be $2e^{-4}H$. Therefore, in this simulation model, the minimum inductor value has been taken as a benchmark and was set to be the inductance of qZSI. The selected parameters used in this simulation model are listed in Table 3.2 below. Three different simulation setups with varied load has been conducted to verify the equation (i.e., R=100Ω, 50Ω and 20Ω).

Table 3.2: System parameters to verify the boundary condition with varied load

Input voltage, V_{in}	$12V$
Desired DC-link output voltage, V_{DC}	$60V$
Capacitor C_1 and C_2 value	$1000\mu F$
Switching frequency, f_s	$10kHz$
Shoot-through duty ratio, D_{st}	0.4
Modulation index, M	0.5
System AC output frequency, f_{AC}	$50Hz$

Table 3.3 shows the theoretical calculated results to classify DCM, BCM and CCM with varied load. Notice that for $R = 100\Omega$, $I_L < I_{LB}$, the qZSI supposed to operate in DCM. For $R = 50\Omega$, I_L value is close to I_{LB}, the qZSI supposed to operate at the boundary condition between CCM and DCM. Lastly, for $R = 20\Omega$, notice that I_L has a value which is greatly larger than the I_{LB}, therefore, the qZSI topology is expected to operate in CCM. Figure 3.16 shows the results of I_{L1} and V_{DC} obtained from MATLAB/Simulink.

Table 3.3: Theoretical calculated results to classify DCM, BCM and CCM

Time interval	Resistance (Ω)	Parameters		Theoretical result			Expected operating mode
		L (μH)	C (μF)	V_{DC} (V)	I_{LB} (A)	I_L (A)	
$0-1.0s$	100	300	1000	60	3.3488	1.80	DCM
$1.0-2.0s$	50	300	1000	60	3.3488	3.60	BCM
$2.0-3.0s$	20	300	1000	60	3.3488	9.00	CCM

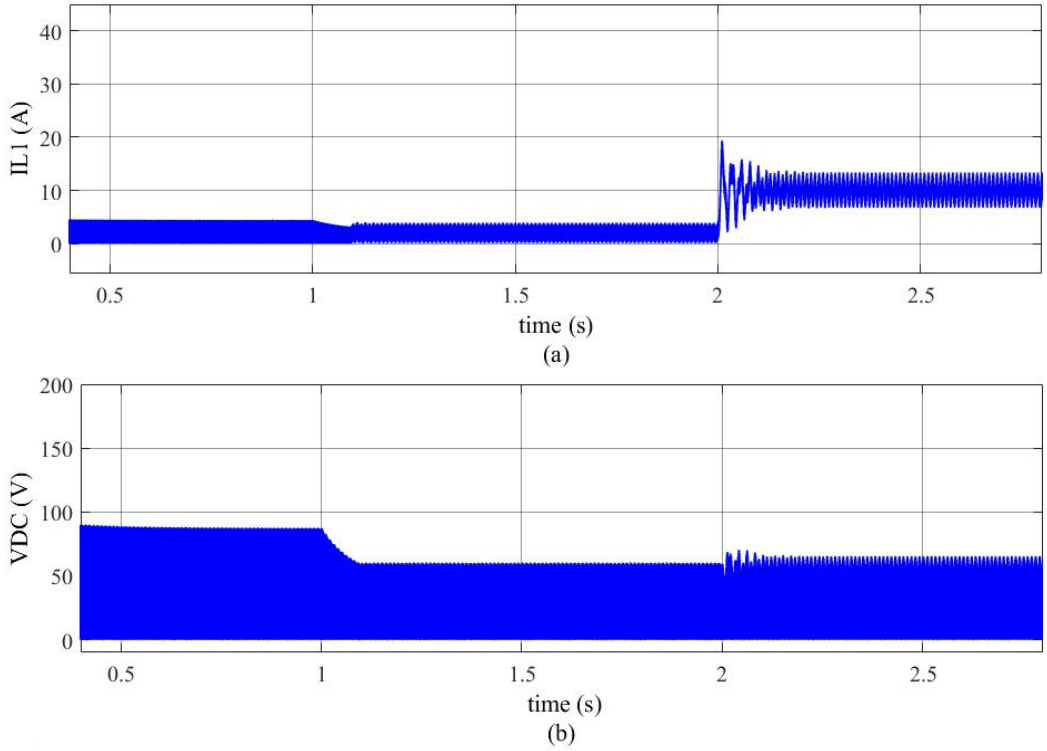

Figure 3.16: Simulated waveform of (a) I_{L1} (b) V_{DC} with varied loads

Simulation results shown in Figure 3.17 are taken when qZSI is operating with load resistance, $R = 100\Omega$ in the time span of $0 \leq t \leq 1.0s$. From the graph, clearly the system is operating in DCM as depicted from the expected outcome in Table 3.3. Zooming into the DC-link voltage, there's a voltage drop when qZSI turn into DCM. In DCM, the obtained simulated results show that qZSI is operating in the region where the CCM steady-state formulae no longer hold. This operating mode causes an over boost effect of

the DC-link and output voltage. To calculate the theoretical output DC-link voltage, equation (3.34) should be used.

Simulation results shown in Figure 3.18 are taken when qZSI is operating with load resistance, $R = 50\Omega$ in the time span of $1.0s \leq t \leq 2.0s$. In Figure 3.18, we can see that inductor current, I_L does not drop to zero, which means that the system is still operating in CCM. However, the inductor current is close to the boundary condition between DCM and CCM, (i.e., its value is close to the zero line). In Figure 3.18(b), the DC-link voltage consists of some incomplete square-shaped waveform which shows that the system is close to the boundary condition.

Simulation results shown in Figure 3.19 were taken when qZSI is operating with load resistance, $R = 20\Omega$ in the time span of $2.0s \leq t \leq 3.0s$. Notice that the lowest point of the current is further away from the y-axis zero line, indicates that the qZSI system is far away from the boundary condition. The results in this simulation model has clearly shown that equation (3.41) is being verified. Both I_{L1} and V_{DC} shown in the simulation results are closely coincide with the calculated theoretical values when qZSI operates in CCM and BCM. However, when qZSI is operating in DCM, the equations are not valid as the inductor current and DC-link voltage values have shown major divergent to the theoretical value. Therefore, the derivation of qZSI transfer function in DCM has been performed and shown in section 3.1.2.

However, the only downside when qZSI operates in CCM (i.e., when qZSI operating mode is further away from boundary condition), the DC-link votage, V_{DC} ripples amplitude is becoming higher and higher. To summarize, DCM offers lowest ripples amplitude on the inductor current and DC-link voltage. The ripples amplitude increases as qZSI goes from DCM to BCM to CCM.

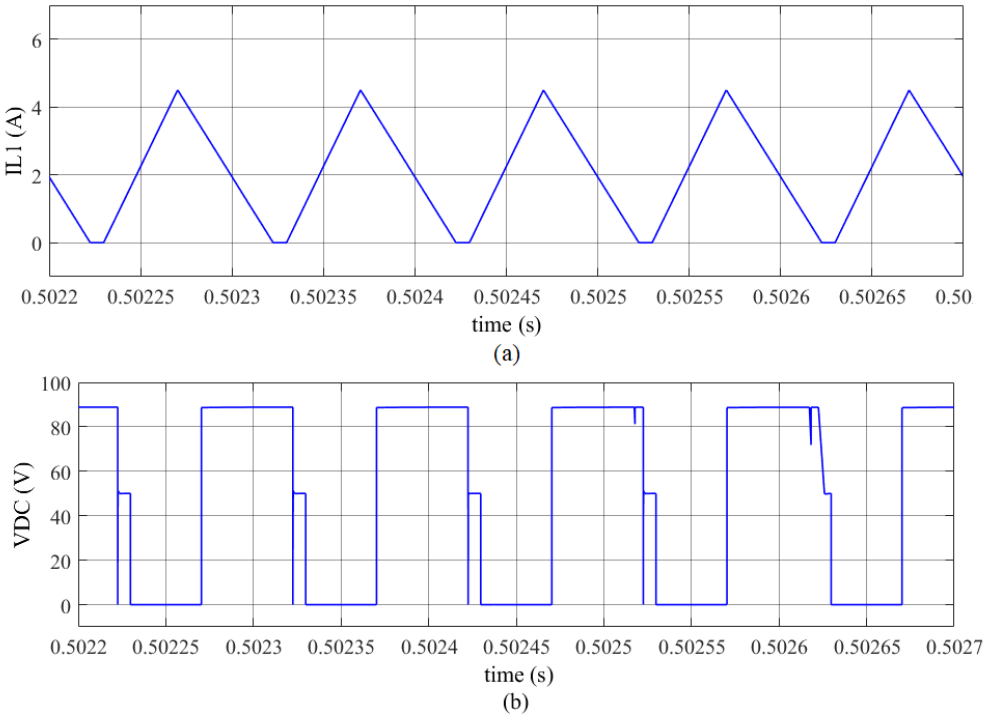

Figure 3.17: Simulated waveform of (a) I_{L1} in DCM (b) V_{DC} in DCM when R=100Ω

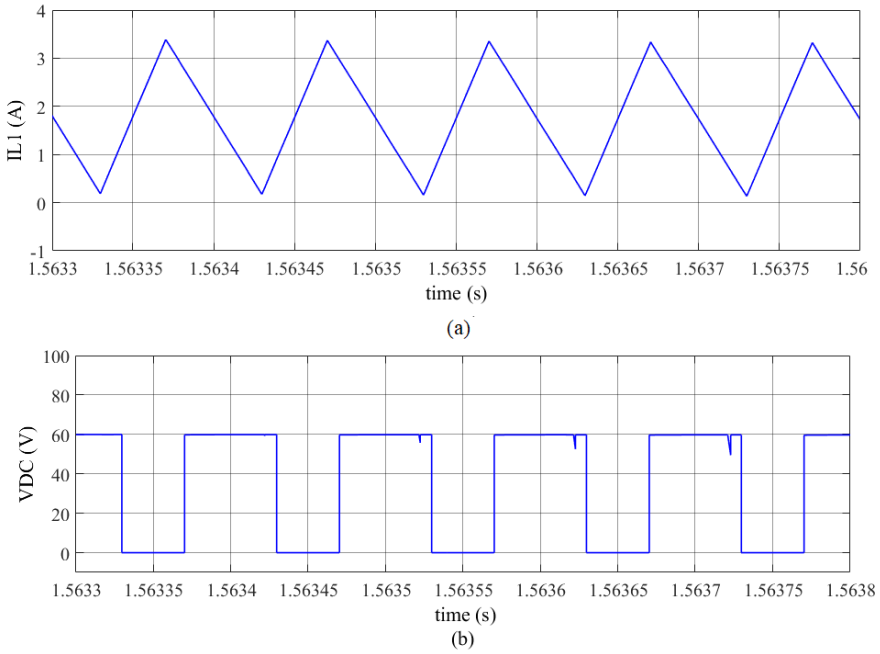

Figure 3.18: Simulated waveform of (a) I_{L1} in BCM (b) V_{DC} in BCM when R=50Ω

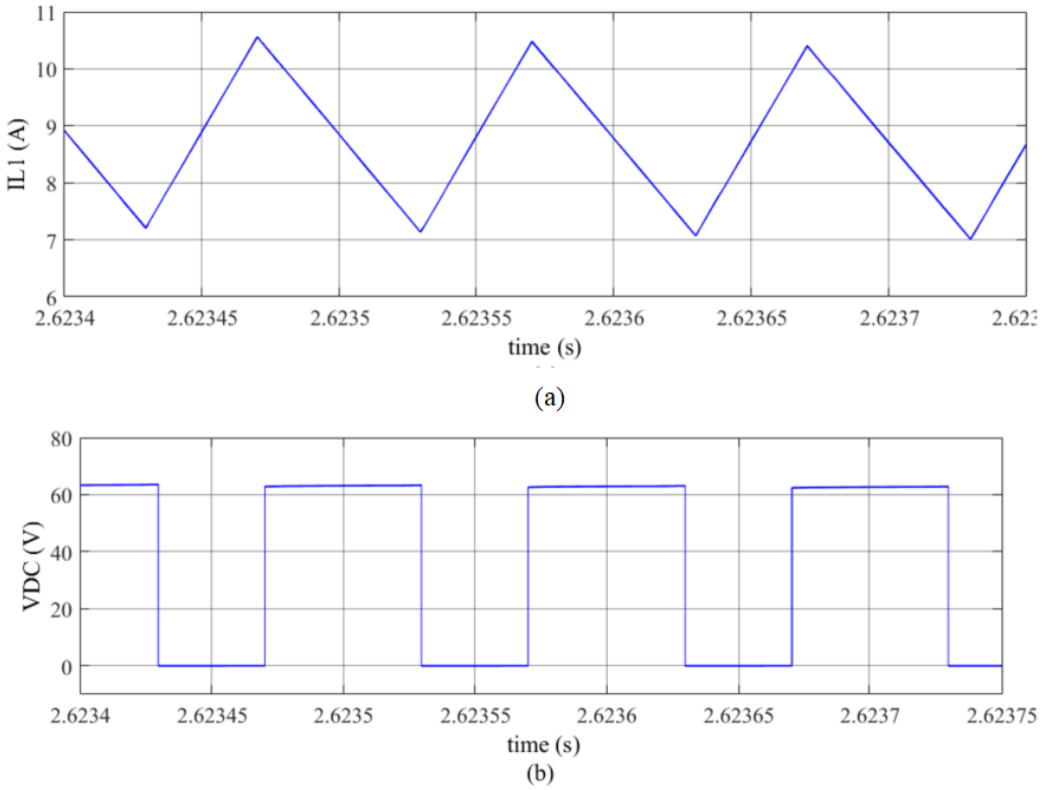

Figure 3.19: Simulated waveform of (a) I_{L1} in CCM (b) V_{DC} in CCM when R=20Ω

3.4 Summary

To conclude this chapter, the simulation results have shown that the derived equations are accurate with the accomplishment of first objective of this research work. There are few parameters that have direct effects on the operating mode of qZSI. These parameters include the inductor value, switching frequency and the duty cycle. Knowing the correlation between these parameters can provide researchers solution to prevent qZSI from turning into DCM, avoiding large voltage stress to the system components. Also, the equations that represents the transfer function of qZSI in DCM have been derived in section 3.2. With these equations, even when the qZSI is operating in DCM, the controller can track the DC-link voltage without significant discrepancies.

Chapter 4 : Proposed Controller Design for qZSI

This chapter presents the detail mathematical derivation of the qZSI small-signal transfer function (i.e., section 4.1.1) and controller design (i.e., section 4.1.2) to achieve a balanced generated output voltage. In this chapter, lead controller is proposed as DC-link controller to realize fast and stable dynamic transient response in qZSI. The derived small-signal transfer function is complied with the proposed controller and merged it into a control system block diagram shown in section 4.1.2. Section 4.1.3 demonstrates the PWM method used to control the switching pulses in qZSI's IGBTs. Using the presented SPWM technique, the shoot-through duty ratio is sent to the modulator system to perform switching in IGBT.

Simulation has been conducted to investigate the proposed design using MATLAB/SIMULINK software. Section 4.2 presents the simulation results conducted to investigate the superiority and the effectiveness of the proposed controller. Section 4.2.1 shows the simulation results when a step change of DC-link voltage reference is applied to the system. The simulation was conducted when qZSI is operating in DCM. On the other hand, section 4.2.2 presents the simulation results when qZSI is operating in CCM. In this section, different loading condition has been applied to qZSI in a specific interval. Lastly, the multilevel output voltage and current were generated based on the PWM method listed in section 4.1.3.

4.1 qZSI Control Scheme

4.1.1 Small-Signal Analysis and Derivation of qZSI Transfer Function

Figure 4.1 shows the small-signal model of qZSI to derive its transfer function. In small-signal analysis of converter topology, the stray resistance (i.e., r_1 and r_2) are included in inductors L_1 and L_2 and the equivalent series resistance (i.e., R_1 and R_2) are included in the capacitors C_1 and C_2.

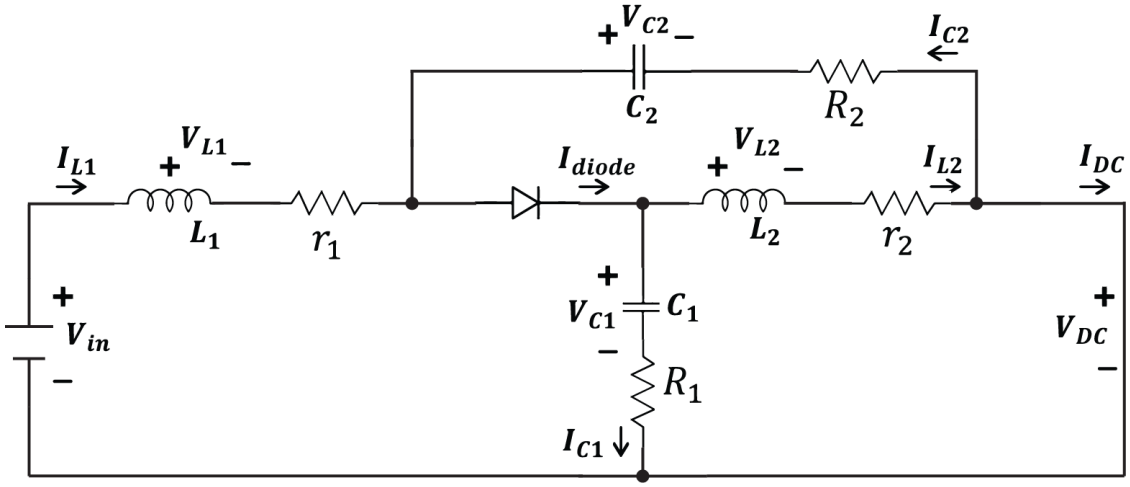

Figure 4.1: Small-signal model of qZSI

Assume that $r = r_1 = r_2$ and $R = R_1 = R_2$, the mathematical equation of small-signal model in shoot-through state can be defined as per equation (4.1) to equation (4.4).

$$\frac{di_{L2}}{dt} = -\frac{R+r}{L} i_{L2} + \frac{1}{L} v_{C1} \tag{4.1}$$

$$\frac{di_{L1}}{dt} = -\frac{R+r}{L} i_{L1} + \frac{v_{C2}}{L} + \frac{v_{in}}{L} \tag{4.2}$$

$$\frac{dv_{C1}}{dt} = -\frac{i_{L2}}{C} \tag{4.3}$$

$$\frac{dv_{C2}}{dt} = -\frac{i_{L1}}{C} \tag{4.4}$$

Where i_{L1} represents the inductor current of L_1. i_{L2} represents the inductor current of L_2. v_{C1} and v_{C2} defines the capacitor voltage for C_1 and C_2 respectively. V_{in} defines the DC input voltage and i_{DC} represents the DC-link output current. Note that the assumption of $L_1 = L_2 = L$ and $C_1 = C_2 = C$ has been made to simplify the derivation of equation.

Hence, the dynamic state equation of qZSI small-signal analysis in shoot-through state can be written as:

$$\begin{bmatrix} \frac{di_{L1}(t)}{dt} \\ \frac{di_{L2}(t)}{dt} \\ \frac{dv_{C1}(t)}{dt} \\ \frac{dv_{C2}(t)}{dt} \end{bmatrix} = \begin{bmatrix} -\frac{r+R}{L} & 0 & 0 & \frac{1}{L} \\ 0 & -\frac{r+R}{L} & \frac{1}{L} & 0 \\ 0 & -\frac{1}{C} & 0 & 0 \\ -\frac{1}{C} & 0 & 0 & 0 \end{bmatrix} \begin{bmatrix} i_{L1}(t) \\ i_{L2}(t) \\ v_{C1}(t) \\ v_{C2}(t) \end{bmatrix} + \begin{bmatrix} \frac{1}{L} & 0 \\ 0 & 0 \\ 0 & 0 \\ 0 & 0 \end{bmatrix} \begin{bmatrix} v_{in}(t) \\ i_{DC}(t) \end{bmatrix} \tag{4.5}$$

Equation (4.5) can be represented with the following simplified equation.

$$\frac{dx}{dt} = A_1 x + B_1 u \tag{4.6}$$

Where

$$x = \begin{bmatrix} i_{L1}(t) \\ i_{L2}(t) \\ v_{C1}(t) \\ v_{C2}(t) \end{bmatrix} \tag{4.7}$$

$$A_1 = \begin{bmatrix} -\frac{r+R}{L} & 0 & 0 & \frac{1}{L} \\ 0 & -\frac{r+R}{L} & \frac{1}{L} & 0 \\ 0 & -\frac{1}{C} & 0 & 0 \\ -\frac{1}{C} & 0 & 0 & 0 \end{bmatrix} \tag{4.8}$$

$$B_1 = \begin{bmatrix} \frac{1}{L} & 0 \\ 0 & 0 \\ 0 & 0 \\ 0 & 0 \end{bmatrix} \tag{4.9}$$

$$u = \begin{bmatrix} v_{in}(t) \\ i_{DC}(t) \end{bmatrix} \tag{4.10}$$

In non-shoot-through state, the relationship between capacitors current and inductor current, the relationship between capacitor voltage, inductor voltage, DC-link voltage and current can be summarized as follows:

$$\frac{dv_{C1}}{dt} = \frac{i_{L1}}{C} - \frac{i_{DC}}{C} \tag{4.11}$$

$$\frac{dv_{C2}}{dt} = \frac{i_{L2}}{C} - \frac{i_{DC}}{C} \tag{4.12}$$

$$\frac{di_{L1}}{dt} = -\frac{r+R}{L} i_{L1} - \frac{v_{C1}}{L} + \frac{R}{L} i_{DC} + \frac{v_{in}}{L} \tag{4.13}$$

$$\frac{di_{L2}}{dt} = -\frac{r+R}{L} i_{L2} - \frac{v_{C2}}{L} + \frac{R}{L} i_{DC} \tag{4.14}$$

Hence, the dynamic state equation of qZSI small-signal analysis in non-shoot-through state can be written as:

$$\begin{bmatrix} \frac{di_{L1}(t)}{dt} \\ \frac{di_{L2}(t)}{dt} \\ \frac{dv_{C1}(t)}{dt} \\ \frac{dv_{C2}(t)}{dt} \end{bmatrix} = \begin{bmatrix} -\frac{r+R}{L} & 0 & -\frac{1}{L} & 0 \\ 0 & -\frac{r+R}{L} & 0 & -\frac{1}{L} \\ \frac{1}{C} & 0 & 0 & 0 \\ 0 & \frac{1}{C} & 0 & 0 \end{bmatrix} \begin{bmatrix} i_{L1}(t) \\ i_{L2}(t) \\ v_{C1}(t) \\ v_{C2}(t) \end{bmatrix} + \begin{bmatrix} \frac{1}{L} & \frac{R}{L} \\ 0 & \frac{R}{L} \\ 0 & -\frac{1}{C} \\ 0 & -\frac{1}{C} \end{bmatrix} \begin{bmatrix} v_{in}(t) \\ i_{DC}(t) \end{bmatrix} \tag{4.15}$$

Equation (4.15) can be represented with the following simplified equation.

$$\frac{dx}{dt} = A_2 x + B_2 u \tag{4.16}$$

Where

$$A_2 = \begin{bmatrix} -\frac{r+R}{L} & 0 & -\frac{1}{L} & 0 \\ 0 & -\frac{r+R}{L} & 0 & -\frac{1}{L} \\ \frac{1}{C} & 0 & 0 & 0 \\ 0 & \frac{1}{C} & 0 & 0 \end{bmatrix} \tag{4.17}$$

$$B_2 = \begin{bmatrix} \frac{1}{L} & \frac{R}{L} \\ 0 & \frac{R}{L} \\ 0 & -\frac{1}{C} \\ 0 & -\frac{1}{C} \end{bmatrix} \tag{4.18}$$

By using equations (4.8), (4.9), (4.17) and (4.18), the dynamic state average equation can be obtained as follows:

$$A = d_{ST}A_1 + (1 - d_{ST})A_2 \tag{4.19}$$

Substitute equation (4.8) and equation (4.17) into equation (4.19), we get

$$A = \begin{bmatrix} -\frac{r+R}{L} & 0 & \frac{(d_{ST}-1)}{L} & \frac{d_{ST}}{L} \\ 0 & -\frac{r+R}{L} & \frac{d_{ST}}{L} & \frac{(d_{ST}-1)}{L} \\ \frac{(1-d_{ST})}{C} & -\frac{d_{ST}}{C} & 0 & 0 \\ -\frac{d_{ST}}{C} & \frac{(1-d_{ST})}{C} & 0 & 0 \end{bmatrix} \tag{4.20}$$

$$B = d_{ST}B_1 + (1 - d_{ST})B_2 \tag{4.21}$$

Substitute equation (4.9) and equation (4.18) into equation (4.21), we get

$$B = \begin{bmatrix} \frac{1}{L} & \frac{R(1-d_{ST})}{L} \\ 0 & \frac{R(1-d_{ST})}{L} \\ 0 & -\frac{1-d_{ST}}{C} \\ 0 & -\frac{1-d_{ST}}{C} \end{bmatrix} \tag{4.22}$$

Hence, the dynamic state average equation can be written as per equation (4.23).

$$\begin{bmatrix} \frac{di_{L1}(t)}{dt} \\ \frac{di_{L2}(t)}{dt} \\ \frac{dv_{C1}(t)}{dt} \\ \frac{dv_{C2}(t)}{dt} \end{bmatrix} = \begin{bmatrix} -\frac{r+R}{L} & 0 & \frac{(d_{ST}-1)}{L} & \frac{d_{ST}}{L} \\ 0 & -\frac{r+R}{L} & \frac{d_{ST}}{L} & \frac{(d_{ST}-1)}{L} \\ \frac{(1-d_{ST})}{C} & -\frac{d_{ST}}{C} & 0 & 0 \\ -\frac{d_{ST}}{C} & \frac{(1-d_{ST})}{C} & 0 & 0 \end{bmatrix} \begin{bmatrix} i_{L1}(t) \\ i_{L2}(t) \\ v_{C1}(t) \\ v_{C2}(t) \end{bmatrix} + \begin{bmatrix} \frac{1}{L} & \frac{R(1-d_{ST})}{L} \\ 0 & \frac{R(1-d_{ST})}{L} \\ 0 & -\frac{1-d_{ST}}{C} \\ 0 & -\frac{1-d_{ST}}{C} \end{bmatrix} \begin{bmatrix} v_{in}(t) \\ i_{DC}(t) \end{bmatrix} \tag{4.23}$$

In small-signal analysis of qZSI topology, the perturbations of small-signal include v_{in}, i_{DC}, d_{ST}, v_{C1}, v_{C2}, i_{L1} and i_{L2} as shown in equation (4.24) to equation (4.30)

$$v_{in} = V_{in} + \widehat{v_{in}} \tag{4.24}$$

$$i_{DC} = I_{DC} + \widehat{i_{DC}} \tag{4.25}$$

$$d_{ST} = D_{ST} + \widehat{d_{ST}} \tag{4.26}$$

$$v_{C1} = V_{C1} + \widehat{v_{C1}} \tag{4.27}$$

$$v_{C2} = V_{C2} + \widehat{v_{C2}} \tag{4.28}$$

$$i_{L1} = I_{L1} + \widehat{i_{L1}} \tag{4.29}$$

$$i_{L2} = I_{L2} + \widehat{i_{L2}} \tag{4.30}$$

Where $\widehat{v_{in}}$ represents the DC-input voltage perturbation, $\widehat{i_{DC}}$ represents the DC-link current perturbation, $\widehat{d_o}$represents the small-signal duty ratio perturbation, $\widehat{v_{C1}}$ and $\widehat{v_{C2}}$ represents the small-signal perturbation of capacitor voltage across C_1 and C_2 respectively, $\widehat{i_{L1}}$ and $\widehat{i_{L2}}$ represents the small-signal perturbation of inductor current flowing through of L_1 and L_2 respectively. On the other hand, V_{in} represents the peak DC-input voltage, I_{DC} represents the peak DC-link current, D_o represents the peak duty ratio, V_{C1} and V_{C2}

represents the peak capacitor voltage of C_1 and C_2 respectively, I_{L1} and I_{L2} represents the peak inductor current flowing through of L_1 and L_2 respectively.

Substituting equation (4.24) to equation (4.30) into equation (4.23), the dynamic state average equation with small-signal perturbations can be written as

$$\begin{bmatrix} \frac{d(I_{L1}(t)+\widehat{\imath_{L1}}(t))}{dt} \\ \frac{d(I_{L2}(t)+\widehat{\imath_{L2}}(t))}{dt} \\ \frac{d(V_{C1}(t)+\widehat{v_{C1}}(t))}{dt} \\ \frac{d(V_{C2}(t)+\widehat{v_{C2}}(t))}{dt} \end{bmatrix} = \begin{bmatrix} -\frac{r+R}{L} & 0 & \frac{(D_{ST}+\widehat{d_{ST}}-1)}{L} & \frac{D_{ST}+\widehat{d_{ST}}}{L} \\ 0 & -\frac{r+R}{L} & \frac{D_{ST}+\widehat{d_{ST}}}{L} & \frac{(D_{ST}+\widehat{d_{ST}}-1)}{L} \\ \frac{(1-D_{ST}-\widehat{d_{ST}})}{C} & -\frac{D_{ST}+\widehat{d_{ST}}}{C} & 0 & 0 \\ -\frac{D_{ST}+\widehat{d_{ST}}}{C} & \frac{(1-D_{ST}-\widehat{d_{ST}})}{C} & 0 & 0 \end{bmatrix} \begin{bmatrix} I_{L1}(t)+\widehat{\imath_{L1}}(t) \\ I_{L2}(t)+\widehat{\imath_{L2}}(t) \\ V_{C1}(t)+\widehat{v_{C1}}(t) \\ V_{C2}(t)+\widehat{v_{C2}}(t) \end{bmatrix} + \begin{bmatrix} \frac{1}{L} & \frac{R(1-D_{ST}-\widehat{d_{ST}})}{L} \\ 0 & \frac{R(1-D_{ST}-\widehat{d_{ST}})}{L} \\ 0 & -\frac{1-D_{ST}-\widehat{d_{ST}}}{C} \\ 0 & -\frac{1-D_{ST}+\widehat{d_{ST}}}{C} \end{bmatrix} \begin{bmatrix} V_{in}(t)+\widehat{v_{in}}(t) \\ I_{DC}(t)+\widehat{\imath_{DC}}(t) \end{bmatrix} \quad (4.31)$$

By doing linearization and Laplace transform on equation (4.31), the following equations can be established.

$$\begin{aligned} \widehat{\imath_L}(s)\big(Ls+(r+R)\big) &= \widehat{d_{ST}}(s)(V_{C1}+V_{C2}-RI_{DC})+\widehat{v_C}(s)(2D_{ST}-1) \\ &\quad +\widehat{\imath_{DC}}(s)(R-RD_{ST})+\widehat{v_{in}}(s) \end{aligned} \quad (4.32)$$

$$\widehat{\imath_L}(s)=\frac{Cs\widehat{v_C}(s)+\widehat{d_{ST}}(s)(I_{L1}+I_{L2}-I_{DC})+\widehat{\imath_{DC}}(s)(1-D_{ST})}{1-2D_{ST}} \quad (4.33)$$

$$\begin{aligned} \widehat{v_C}(s)[(LCs^2+C(r+R)s)+(1-2D_{ST})^2] &= \widehat{d_{ST}}(s)\big[(I_{DC}-I_{L1}-I_{L2})\big(Ls+(r+R)\big) \\ &\quad +(V_{C1}+V_{C2}-RI_{DC})(1-2D_{ST})\big] \\ &\quad +\widehat{\imath_{DC}}(s)\big[(D_{ST}-1)\big(Ls+(r+R)\big) \\ &\quad +(R-RD_{ST})(1-2D_{ST})\big]+\widehat{v_{in}}(s)(1-2D_{ST}) \end{aligned} \quad (4.34)$$

From equation (4.34), the capacitor voltage to duty cycle transfer function can be expressed as:

$$G_{\widehat{v_c}\widehat{d_{ST}}} = \frac{\widehat{v_C}(s)}{\widehat{d_{ST}}(s)} \tag{4.35}$$

$$G_{\widehat{v_c}\widehat{d_{ST}}} = \frac{\left[(I_{DC} - I_{L1} - I_{L2})\big(Ls + (r+R)\big) + (V_{C1} + V_{C2} - RI_{DC})(1 - 2D_{ST})\right]}{[LCs^2 + C(R+r)s + (1 - 2D_{ST})^2]} \tag{4.36}$$

Using equation (4.32) and equation (4.33) The open-loop transfer function for current inner loop of qZSI topology (i.e., the inductor current to duty cycle transfer function) can be derived as:

$$G_{\widehat{i_L}\widehat{d_{ST}}} = \frac{Cs(V_{C1} + V_{C2} - RI_o) + (I_{L1} + I_{L2} - I_o)(1 - 2D_{ST})}{\big[(Ls + R + r)[LCs^2 + (R+r)Cs + (1 - 2D_{ST})^2]\big]} \tag{4.37}$$

The transfer function of the DC-link voltage to inductor current is derived as:

$$G_{\widehat{i_L}\widehat{v_{DC}}} = \left(\frac{D_{ST}}{L}\right)\left(\frac{1}{s}\right) \tag{4.38}$$

All the components stated in equation (4.36) to equation (4.38) are DC components.

During DCM mode, an extra interval of discontinuous current in qZSI circuit is formed. The inductor current falls to zero causing distortion to the DC-link output voltage. DCM occurs after the completion of discharging of the inductor current (i.e., active-state). With the present of DCM, the following equation can be established.

$$d_{NST} = d_D + d_{active} \tag{4.39}$$

Where d_{NST} is the duty ratio for non-shoot-through state, d_D is the duty ratio for DCM, d_{active} is the duty ratio for active-state.

Over a switching cycle, the summation of shoot-through duty ratio and the non-shoot-through duty ratio will equal to zero. Therefore,

$$1 - d_{NST} - d_{ST} = 0 \tag{4.40}$$

Substitute equation (4.39) into equation (4.40), obtained equation (4.41) as follows:

$$d_{active} = 1 - d_D - d_{ST} \tag{4.41}$$

Referring to equation (4.23) and by substituting equation (4.41) into equation (4.23), the dynamic state space equation of qZSI in active-state of a discontinuous conduction system can be written as per equation (4.42).

$$\begin{bmatrix} \frac{di_{L1}(t)}{dt} \\ \frac{di_{L2}(t)}{dt} \\ \frac{dv_{C1}(t)}{dt} \\ \frac{dv_{C2}(t)}{dt} \end{bmatrix} = \begin{bmatrix} \frac{(r+R)(-1+d_D)}{L} & 0 & \frac{-1+d_{ST}+d_D}{L} & \frac{d_{ST}}{L} \\ 0 & \frac{(r+R)(-1+d_D)}{L} & \frac{d_{ST}}{L} & \frac{-1+d_{ST}+d_D}{L} \\ \frac{(1-d_{ST}-d_D)}{C} & -\frac{d_{ST}}{C} & 0 & 0 \\ -\frac{d_{ST}}{C} & \frac{(1-d_{ST}-d_D)}{C} & 0 & 0 \end{bmatrix} \begin{bmatrix} i_{L1}(t) \\ i_{L2}(t) \\ v_{C1}(t) \\ v_{C2}(t) \end{bmatrix} + \begin{bmatrix} \frac{1}{L} & \frac{R(1-d_{ST}-d_D)}{L} \\ 0 & \frac{R(1-d_{ST}-d_D)}{L} \\ 0 & -\frac{1-d_{ST}-d_D}{C} \\ 0 & -\frac{1-d_{ST}-d_D}{C} \end{bmatrix} \begin{bmatrix} v_{in}(t) \\ i_{DC}(t) \end{bmatrix} \tag{4.42}$$

Substituting equation (4.24) to equation (4.30) into equation (4.42), and by doing linearization, the following equations are established:

$$\begin{bmatrix} \frac{d\widehat{i_{L1}}(t)}{dt} \\ \frac{d\widehat{i_{L2}}(t)}{dt} \\ \frac{d\widehat{v_{C1}}(t)}{dt} \\ \frac{d\widehat{v_{C2}}(t)}{dt} \end{bmatrix} = \begin{bmatrix} \frac{(r+R)(-1+d_D)}{L}\widehat{i_{L1}} + \frac{V_{C1}+V_{C2}-I_{DC}R}{L}\widehat{d_{ST}} + \frac{-1+D_{ST}+d_D}{L}\widehat{v_{C1}} + \frac{D_{ST}}{L}\widehat{v_{C2}} + \frac{R(1-D_{ST}-d_D)}{L}\widehat{i_{DC}} + \frac{1-d_D}{L}\widehat{v_{in}} \\ \frac{(r+R)(-1+d_D)}{L}\widehat{i_{L2}} + \frac{V_{C1}+V_{C2}-I_{DC}R}{L}\widehat{d_{ST}} + \frac{-1+D_{ST}+d_D}{L}\widehat{v_{C2}} + \frac{D_{ST}}{L}\widehat{v_{C1}} + \frac{R(1-D_{ST}-d_D)}{L}\widehat{i_{DC}} \\ \frac{1-D_{ST}-d_D}{C}\widehat{i_{L1}} - \frac{D_{ST}}{C}\widehat{i_{L2}} + \frac{-I_{L1}-I_{L2}+I_{DC}}{C}\widehat{d_{ST}} + \frac{-1+D_{ST}+d_D}{C}\widehat{i_{DC}} \\ -\frac{D_{ST}}{C}\widehat{i_{L1}} + \frac{1-D_{St}-d_D}{C}\widehat{i_{L2}} + \frac{-I_{L1}-I_{L2}+I_{DC}}{C}\widehat{d_{ST}} + \frac{-1+D_{ST}+d_D}{C}\widehat{i_{DC}} \end{bmatrix} \tag{4.43}$$

By taking Laplace transform to equation (4.43), the following transfer function that indicates the relationship between capacitor voltage and duty cycle in DCM can be derived as:

$$G_{\widehat{v_c}\widehat{d_{ST}}} = \frac{[(sL+(R+r)(1-d_D))(-I_{L1}-I_{L2}+I_{DC})+(V_{C1}+V_{C2}-RI_{DC})(1-(2D_{ST}+d_D))]}{[LCs^2+C(R+r)(1-d_D)s+(1-2D_{ST}-d_D)^2]} \tag{4.44}$$

4.1.2 The Design of DC-link Voltage Controller (Lead Compensator)

The transfer function derived in section 4.1.1 above can be drawn into signal-flow graph as shown in Figure 4.2 below. The signal-flow graph is drawn to eliminate some of the external disturbances that can be ignored and simplified it into control system block diagram as shown in Figure 4.3.

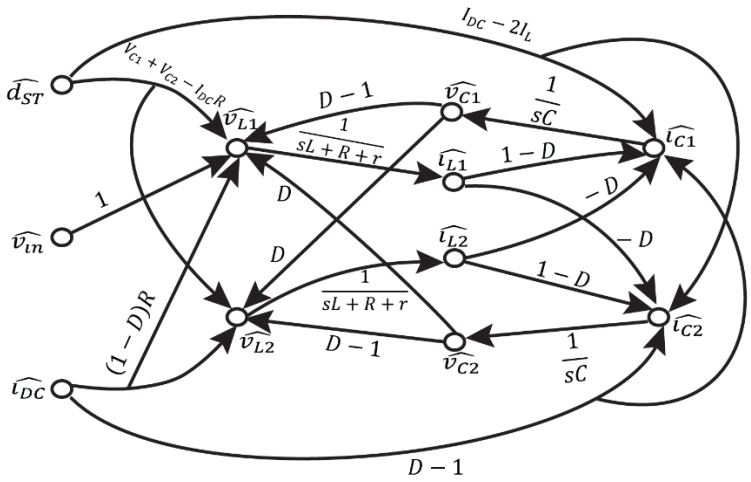

Figure 4.2: Signal-flow graph of qZSI transfer function

Lead compensator can effectively reduce the overshoot percentage and increase the gain crossover frequency of a system to realize fast transient response. In other words, with lead compensator, the bandwidth of the system's frequency response can be increased in proportional with the increased of gain crossover frequency. On the other hand, reduction of overshoot percentage can also be attained by increasing the phase stability margin at the crossover frequency. Figure 4.3 illustrates the proposed voltage-current closed-loop control system that generates the shoot-through duty ratio to acquire the desire buck and boost capabilities of qZSI. It is designed based on qZSI small-signal equivalent circuit and the signal-flow graph shown in Figure 4.2. To achieve DC-link voltage control, the difference between the DC-link voltage reference value, V_{DC}^{*} will pass through a lead compensator with transfer function $G_C(s)$ to generate a corresponding shoot-through duty ratio, d_{ST} towards the unipolar sinusoidal PWM technique.

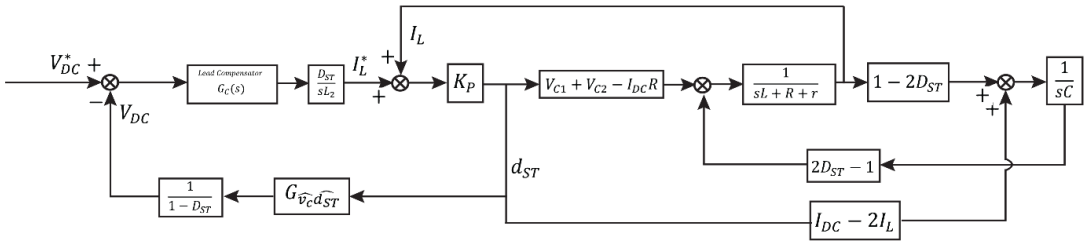

Figure 4.3: Voltage-current closed-loop control strategy using lead compensator

Figure 4.4 shows the conventional PI controller voltage-current closed-loop control strategy. Notice that in the lead compensator control strategy diagram, equation (4.38) is derived as a transfer function of the DC-link voltage to inductor current and it is used to replace the integral terms in PI controller. As a result, it provides more flexibility to the design process of the DC-link control system.

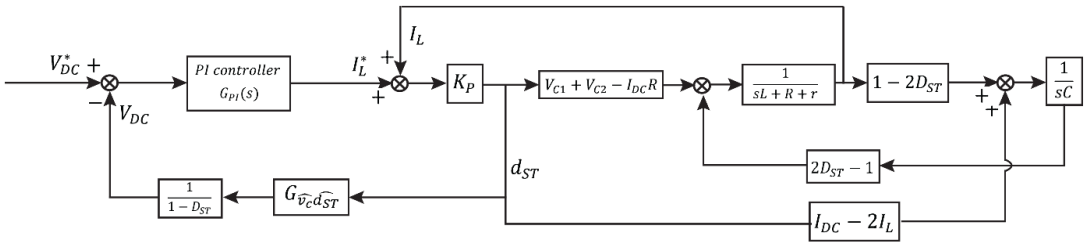

Figure 4.4: Voltage-current closed-loop control strategy using PI controller

Both the control strategy in Figure 4.3 and Figure 4.4 consists of a voltage loop and a current inner loop. The proportional control (i.e., K_p) regulates the difference between the current reference with the actual inductor current. The two-control loop strategy is employed to handle the presence of non-minimum phase. The main purpose of inner current control is to regulates the dynamic response speed and at the same time reducing the overshoot percentage. Desired shoot-through duty cycle (i.e., d_{st}) is generated according to the DC-link voltage reference. The shoot-through duty cycle then passes through a control strategy block (i.e., to calculate the capacitor voltage.)

The lead compensator general equation is defined as:

$$G_C(s) = \frac{\frac{1}{\gamma}\left(s + \frac{1}{T}\right)}{s + \frac{1}{\gamma T}} \tag{4.45}$$

The following summarized are the sequences to obtain all the parameters in equation (4.45)

Step 1: Determine the system type of a unity feedback system to calculate the steady-state error from its closed-loop or the open-loop transfer function.

Step 2: Determine the closed-loop bandwidth to meet peak time and settling time requirement. By setting a desired overshoot percentage, the damping ratio of the system is calculated by equation (4.46).

$$\xi = \frac{-\ln\left(\frac{\%OS}{100}\right)}{\sqrt{\pi^2 + \ln^2\left(\frac{\%OS}{100}\right)}} \tag{4.46}$$

Where ξ is the damping ratio and %OS is the overshoot percentage of the uncompensated system.

The bandwidth of the system is defined as:

$$\omega_{BW} = \frac{\pi}{T_p\sqrt{1-\xi^2}}\sqrt{(1-2\xi^2) + \sqrt{4\xi^4 - 4\xi^2 + 2}} \tag{4.47}$$

Where T_p is the peak time of the uncompensated system.

Step 3: Increase the low frequency magnitude responses to reduce the steady-state error. In other words, the gain *K* should be varied to attain the desired steady-state error.

Step 4: Plot a bode plot and determine the uncompensated system's phase margin.

Step 5: Choose the phase margin which can meet the required damping ratio and overshoot percentage via equation (4.48) as follows:

$$\emptyset_{PM} = \tan^{-1}\frac{2\xi}{\sqrt{-2\xi^2 + \sqrt{1 + 4\xi^4}}} \tag{4.48}$$

Step 6: Calculate the desired phase contribution of the lead compensator by adding a correction factor to compensate for the lower uncompensated system's phase angle.

Step 7: Determine γ from the lead compensator's required phase contribution and determine the magnitude of the compensator at the peak of the phase curve. γ can be determined using equation as follows:

$$\gamma = \frac{1 - sin\, \emptyset_{max}}{1 + sin\, \emptyset_{max}} \tag{4.49}$$

Where Φ_{max} is the total phase contribution required from the lead compensator. The magnitude of the compensator is derived as:

$$|G_c(j\omega_{max})| = \frac{1}{\sqrt{\gamma}} \tag{4.50}$$

Step 8: From the bode plot, the new phase margin frequency, w_{max} can be determined by selecting the frequency at which the uncompensated system's magnitude is the negative of the magnitude of the compensator; the magnitude is in logarithm scale.

Step 9: Determine the value *T* of the compensator.

$$T = \frac{1}{w_{max}\sqrt{\gamma}} \tag{4.51}$$

Step 10: Redesign of the compensator by repeating the procedure using different correction factor if the requirement is not met.

Once the controller can achieve encouraging performance in theoretical simulation model, a real-time simulation model will be carried on by feeding the DC-link voltage and inductor current values from qZSI into the controller block diagram.

Figure 4.5 illustrates the real-time control system block diagram. During real-time simulation, two qZSI parameters will be obtained and to be fed into the controller (i.e., V_{DC} and I_{L1}). The controller then calculates the difference between the reference DC-link voltage (i.e., V_{DC}^{*}) and the actual DC-link voltage (i.e., V_{DC}). These differences are then compensated by using lead compensator. Through equation (4.38), the compensated signal will be transformed to the inductor current reference signal and it is used to compare

with the actual inductor current value. Lastly, passing the signal through the proportional gain in the inner current loop, the desired shoot-through duty ratio is obtained.

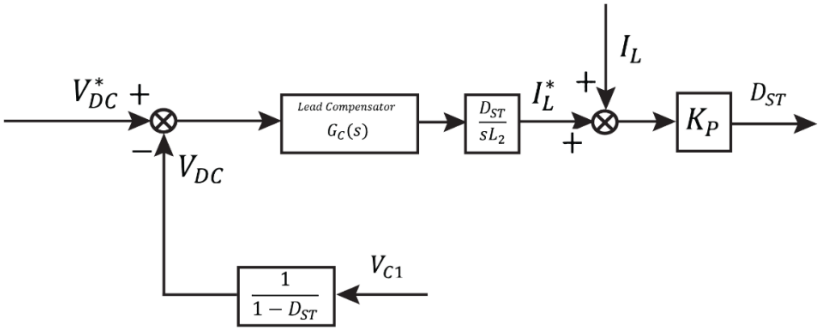

Figure 4.5: Real-time controller block diagram (Lead Compensator)

4.1.3 Sinusoidal Pulse Width Modulation Technique

Different type of PWM method has been proposed for qZSI to achieve wider modulation range and provide lower voltage stress on the semiconductor switches, include SPWM and SVM technique. Three traditional SPWM method were introduced for qZSI which include simple boost control, maximum boost control and maximum constant boost control. The difference between these SPWM techniques are the voltage gain and the frequency ripples.

The principle of the SPWM for the two-level qZSI is illustrated in Figure 4.6. The fundamental frequency component in the qZSI output can be controlled by the amplitude modulation index:

$$m_a = \frac{V_m}{V_{carrier}} \tag{4.52}$$

Where V_m is the sinusoidal modulating waves and $V_{carrier}$ is the triangular carrier wave.

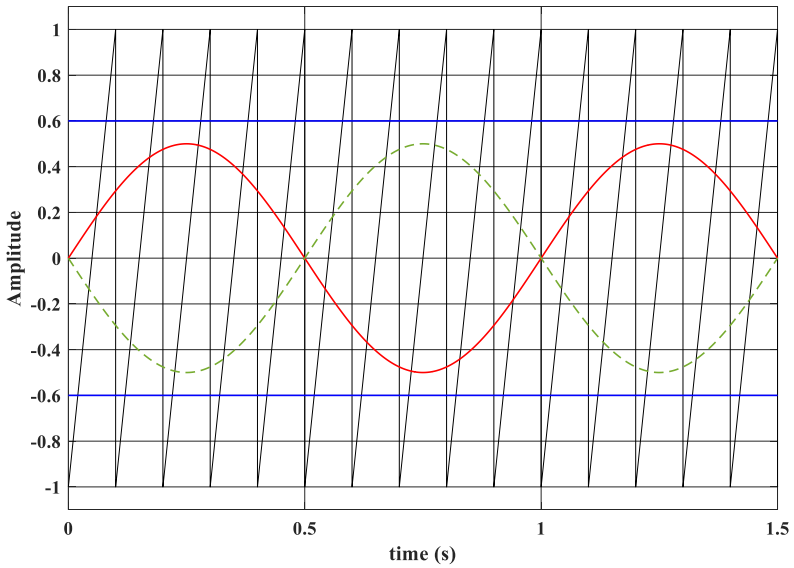

Figure 4.6: Simple Boost Control SPWM

Figure 4.7 shows the block diagram to generate SPWM waveform. The blue straight line in Figure 4.6 represents the shoot-through duty ratio reference generated by

the DC-link voltage controller. There are two different type of carrier wave used for SPWM (i.e., sawtooth or triangle waveform); each generating slightly different output voltage. The sinusoidal waveforms represent the modulation signal. Noticed in simple boost SPWM, two modulating signals are required. The shoot-through reference of simple boost control is a straight line equal or higher than the top envelope of modulation waves, or equal to or lower than the bottom envelope of the modulation waves. When the carrier signal is greater than the positive shoot-through reference line or smaller than the negative shoot-through reference line, the switching signal for shoot-through state will be generated. Therefore, $IGBT_1$ and $IGBT_2$ are switched ON (as shown in Figure 4.7). In active-state, when the sinusoidal signal is greater than the carrier signal, $IGBT_1$ and $IGBT_4$ will be turned on. When the carrier signal is larger than the carrier signal, $IGBT_2$ and $IGBT_3$ will be switched on.

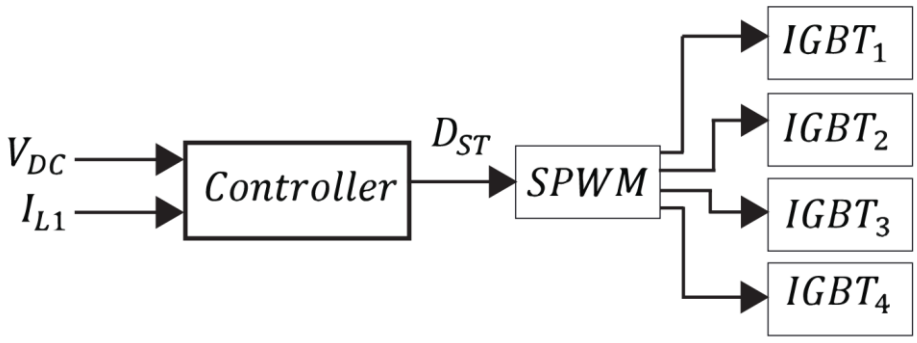

Figure 4.7: Block diagram of SPWM

Conventional SPWM technique is unable to generate multilevel output waveform. To generate multilevel output voltage, PS-SPWM (shown in Figure 4.8) is introduced. In general, a multilevel inverter with *n* voltage levels requires (n-1) triangular carrier. In PS-SPWM, all the triangular carriers have the same frequency and the same peak-to-peak amplitude. However, there is a phase-shift between any two adjacent carrier waves, which can be calculated by using the formula:

$$\emptyset_{carrier} = \frac{360°}{n-1} \tag{4.53}$$

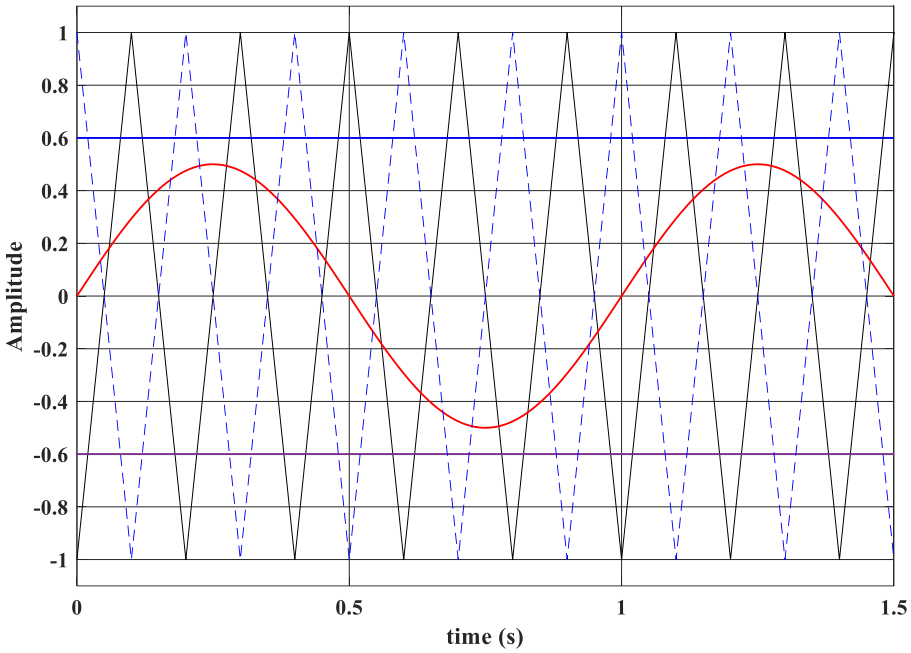

Figure 4.8: Phase-shifted SPWM

The sinusoidal waveform in the Figure 4.8 represents the modulating signal, which is the same as conventional SPWM. However, in PS-SPWM, only requires one sinusoidal waveform. To generate multilevel stepped voltage waveform, the carriers of different H-bridge modules are shifted 60° to each other.

4.2 Simulation Results

Intensive simulation works are performed using MATLAB/SIMULINK for the proposed qZSI and its associated control scheme in both CCM and DCM. This section can be categorized into 2 parts:

- Section 4.2.1: Simulation results of DC-link control scheme in DCM with step changes in DC-link voltage reference.
- Section 4.2.2: Simulation results of DC-link control scheme with varied loading condition in CCM.

4.2.1 Step Change of DC-link Voltage Reference in DCM

In this section, the simulation model is conducted when the qZSI is operating in DCM. To demonstrate the effectiveness and feasibility of the proposed controller with constant modulation index, qZSI topology was tested in response to a step change of DC-link reference voltage (i.e., $35V$ to $50V$). The equations (3.21) does not hold as the qZSI is operating in DCM. Therefore, in this simulation model, the equation that govern the DC-link voltage in DCM can be referred to equation (3.34). Table 4.1 below shows the system parameters used in this simulation model. From simulation results shown in section 3.3.1, the minimum inductor value to achieve CCM is roughly calculated to be around $200\mu H$. Therefore, in this simulation model, to achieve DCM, an inductor which is smaller than that value is chosen (i.e., $100\mu H$) to achieve DCM for all time interval. The proposed controller's steady-state error, dynamic and transient responses were analysed with different DC voltage references. This section also demonstrates the controller performance comparison between lead compensator and PI controller.

Table 4.1: System parameters for qZSI topology with step-change in DC-link reference voltage

Input voltage	$12V$
Switching frequency, f_s	$10kHz$
Step up voltage	$35V$ to $50V$
Capacitor C_1 and C_2 value	$1000\mu F$
Inductance L_1 and L_2 value	$100\mu H$
Load resistance, Ω	30Ω
System AC output frequency, f_{AC}	$50Hz$
Modulation index, M	0.5

The proposed lead controller can reach a step change of $35V$ to $50V$ with very fast and stable dynamic response. The design of DC-link voltage loop and inner current loop transfer function can be found in Appendix B. Few parameters have been chosen when designing the controller, the desired percentage overshoot value to design lead compensator is set to be less than 5% and the peak time was set to be less than $0.1s$. Table 4.2 shows the controller parameters for both lead compensator and PI controller. Also, the current inner loop proportional gain for both designs were included. The parameter of the PI controller used in control loop and P controller in the current inner loop were obtained by tuning the response speed for P controller and both response speed and transient behaviour for PI controller. The tuning procedure of the controller can be found in Appendix C.

Table 4.2: Lead compensator and PI controller parameters

Lead compensator		PI controller $\left(P + I\left(\frac{1}{s}\right)\right)$	
Lead compensator gain	19.9785	Proportional gain	46.462
Current inner loop proportional gain	$7.79x10^{-4}$	Integral Coefficient	30756.516
Transfer function of lead compensator	$19.9785 * \frac{s + 13334.15}{s + 266395.76}$	Current inner loop proportional gain	1.519

Figure 4.9 shows the dynamic response of capacitors' voltage (V_{C1} and V_{C2}). It proved that the equation derived in section 4.1.1 is accurate; showing that the magnitude of capacitor C_1 voltage (i.e., V_{C1}) is larger when compared to capacitor C_2 voltage (i.e., V_{C2}) in equation (3.19) and (3.20). By using the derived equation (3.19) and (3.20), V_{C1} and V_{C2} are calculated to be 12V and 23V respectively, to generate a 35V output DC-link voltage.

From Figure 4.10, equation (3.34) was realized to describe the relationship between the shoot-through duty ratio D_{ST} and the DC-link voltage, V_{DC} as shown in Figure 4.11. Figure 4.11 indicates the dynamic response of the DC-link voltage and its average value in real-time simulation (i.e., V_{mean} stated in Figure 4.11). For instance, large shoot-through duty ratio was required to achieve higher DC-link voltage and vice versa. Notice that in DCM, the DC-link voltage transfer function listed in equation (3.21) no longer holds; as depicted from section 3.3.1 and section 3.3.2. The discontinuous conduction duty cycle (i.e., D_D) can be calculated using the following formula (i.e., $D_D = \frac{V_{C1} - V_{in} + D_{ST}(V_{in} - 2V_{C1})}{V_{C1} - V_{in}}$) listed in equation (3.36).

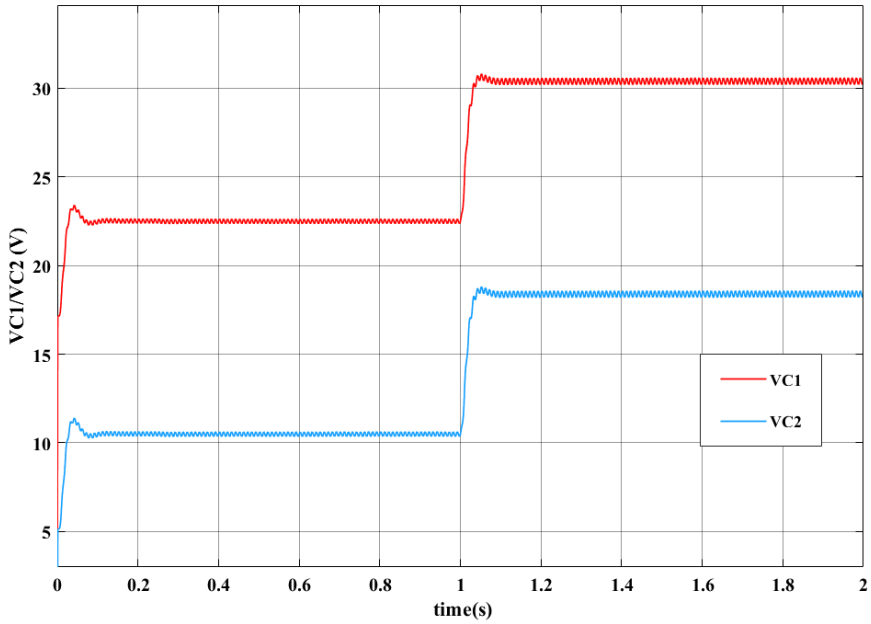

Figure 4.9: qZS DC capacitors' voltages V_{C1} and V_{C2}

Figure 4.9 and Figure 4.11 show how the proposed controller responded to a step change of voltage reference with a very fast dynamic response (i.e., within $50ms$), which has met the expectation of our research objective (i.e., dynamic response within $200ms$). The relationship between DC-link voltage V_{DC} and capacitor voltage (i.e., V_{C1} and V_{C2}) shown in Figure 4.11 and Figure 4.9 can be proven using equation (3.14) in active-state. By examining the percentage overshoot of Figure 4.11, notice that the proposed controller can maintain a very a low percentage overshoot at the beginning of the simulation and during the step change interval. The first overshoot has accounted for approximately 3% while the second overshoot that occured when the step change in the DC-link reference voltage is applied has accounted for a value less than 1%.

Figure 4.12 (a) and (b) demonstrates AC output voltage, V_{AC} and current, I_o waveform respectively. The voltage and current distortion in DCM would be higher comparing to when it operates in CCM. By having a closer look at the generated output voltage waveform, observed that there are some incomplete wave patterns occurred which indicates that the system is operating in DCM. Also, the inductor current value falls to

zero during some interval in non-shoot-through state. Figure 4.13 shows the zoomed-in version of AC output voltage and current (i.e., V_{AC} and I_o).

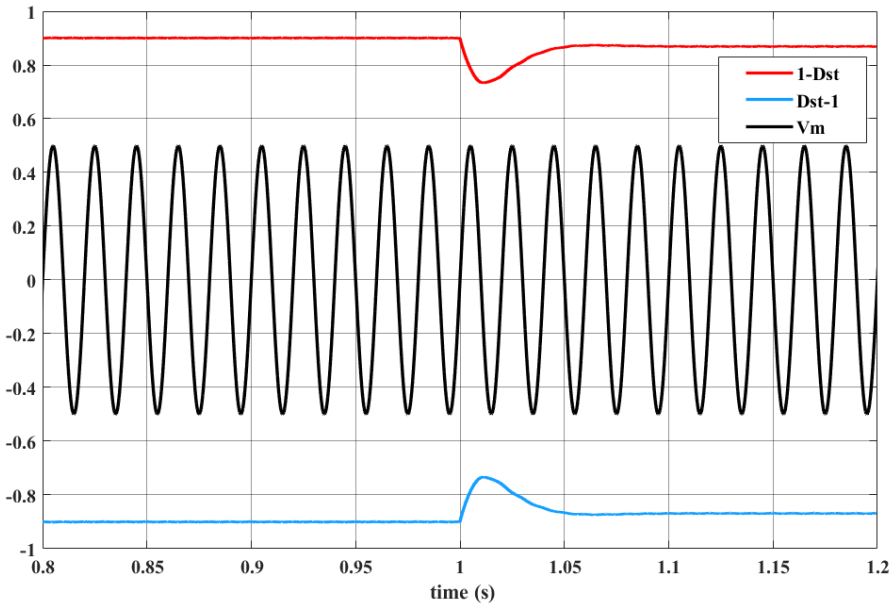

Figure 4.10: Shoot-through duty cycle with modulation signal waveform

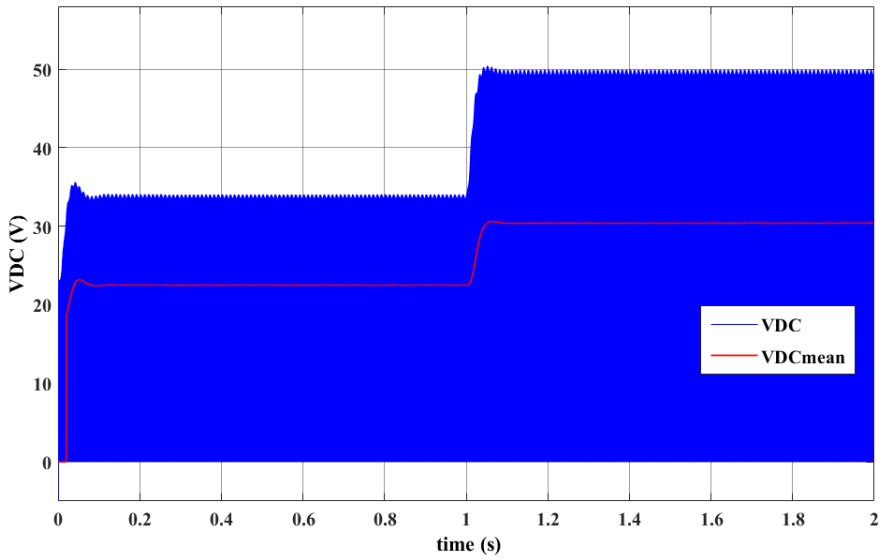

Figure 4.11: DC-link output voltage (V_{DC}) waveform

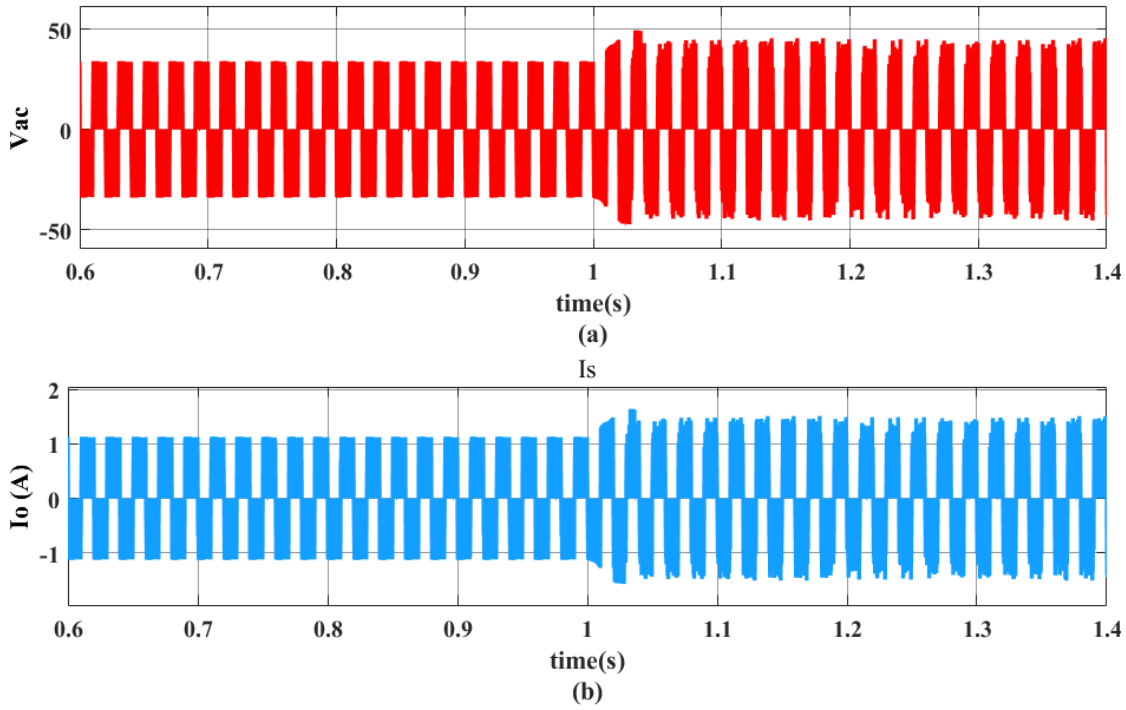

Figure 4.12: (a) AC output voltage, V_{AC} (b) AC output current, I_o

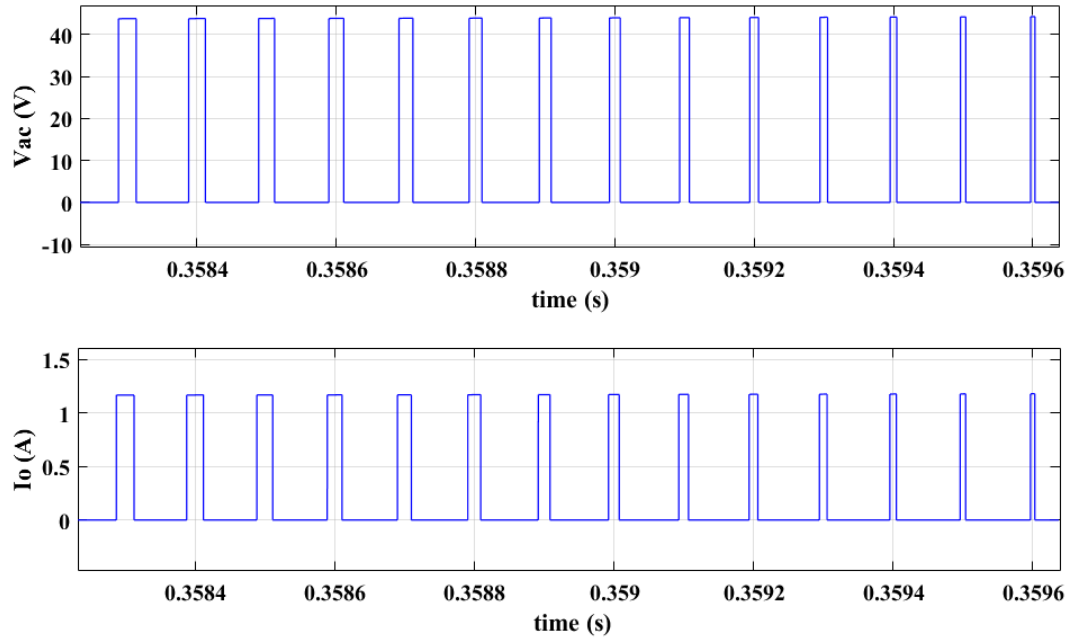

Figure 4.13: Zoomed in of (a) AC output voltage, VAC (b) AC output current, Io

Figure 4.14(a) shows the theoretical DC-link voltage control using lead compensator without the current inner loop. The waveform is generated based on the derived small-signal transfer function. A closer "zoomed-in" look of Figure 4.14(a) was presented clearly to analyse system damping and steady-state error. The step change for theoretical analysis was performed when the time reach the interval of $0.05s$ to show a closer and clearer view. Notice that when current inner loop is absent, the theoretical DC-link voltage has a very high percentage overshoot and damping ratio. Also, it shows a steady-state error of about 1% as depicted in Figure 4.14(b).

To resolve the steady-state error and reduce the overshoot in DC-link voltage, current inner loop is added to the DC-link control system. The theoretical simulation result was presented in Figure 4.15. With the proportional gain in the current inner loop, it allows the system damping ratio to be reduced and so its percentage overshoot. However, since the damping ratio has been reduced, the setting time has been increased in proportional. Nevertheless, the dynamic response is still within a very good and fast manner.

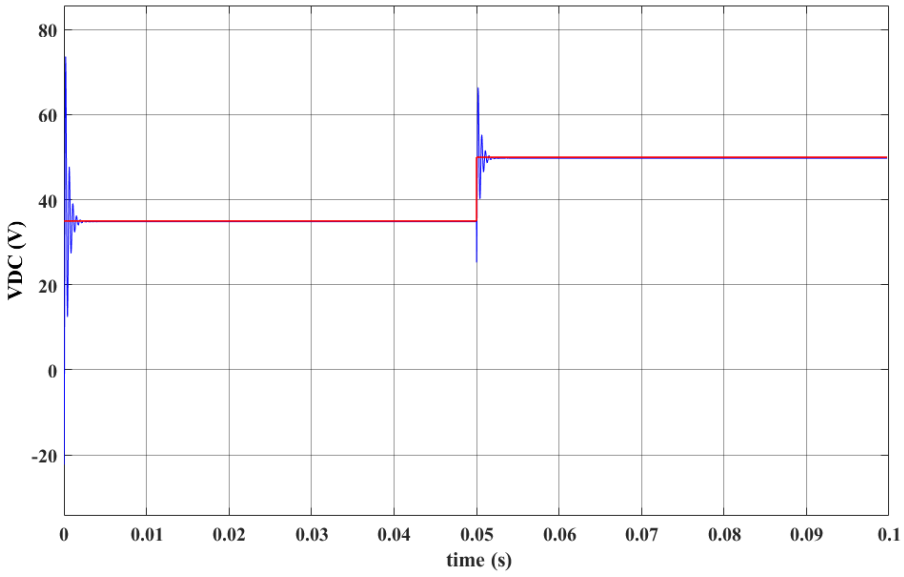

(a)

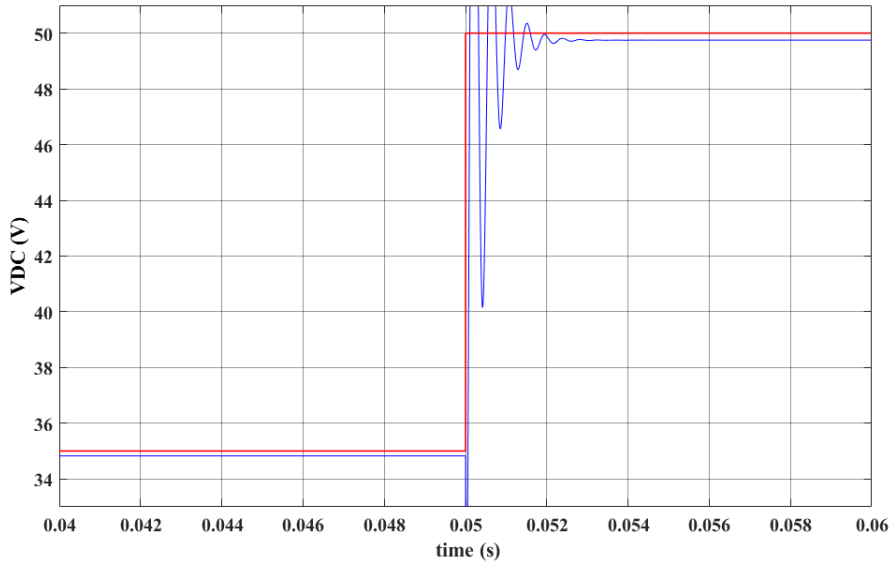

(b)

Figure 4.14: (a) DC-link control system without current inner loop (b) Closer view (steady-state error)

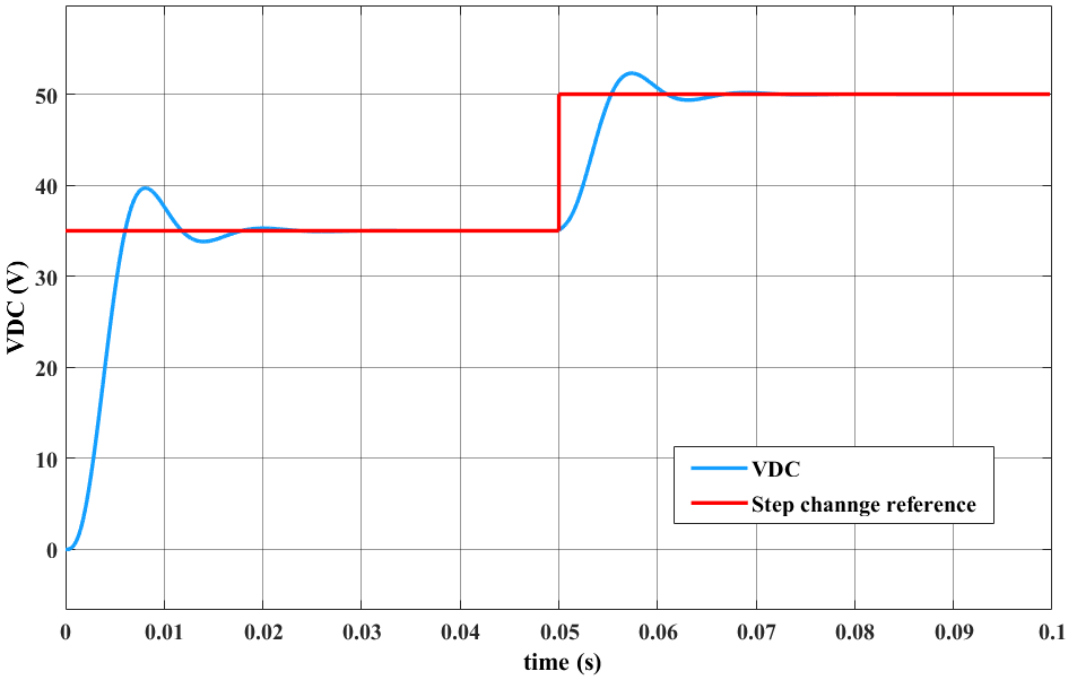

Figure 4.15: Step change of DC-link voltage based on mathematical model with current inner loop

Figure 4.16 shows the frequency response of the original system and the compensated system. The phase margin and gain margin of the uncompensated and compensated system was listed in Table 4.3. From the bode plot, the phase margin and gain margin of the original system were $-26.6°$ and $-16.6dB$ respectively. Negative gain and phase margin indicates that the system is unstable. However, after the system has been compensated by using lead compensator, the phase margin and the gain margin can be improved and increased to $10.7°$ and $5.74dB$ respectively. The positive gain indicated in the lead compensator transfer function (i.e., 19.9785), shifted the crossover frequency of both magnitude and phase waveform to the right, improving the gain and phase margin. Adding the current inner loop to the compensated system further improve the frequency response. The phase margin and gain margin were further improved to $62.3°$ and $12.74dB$ respectively. The phase margin improvement reduces the overshoot percentage, which is corresponding to the desired phase margin calculated during the design of the lead compensator. However, after inserting current inner loop, the gain crossover

frequency has been greatly reduced. Despite, from Figure 4.15, the peak time and settling time obtained from the system is still encouraging. The reduction of the gain crossover frequency might due to the gain of the proportional (P) controller in the inner current loop, which is incredibly small.

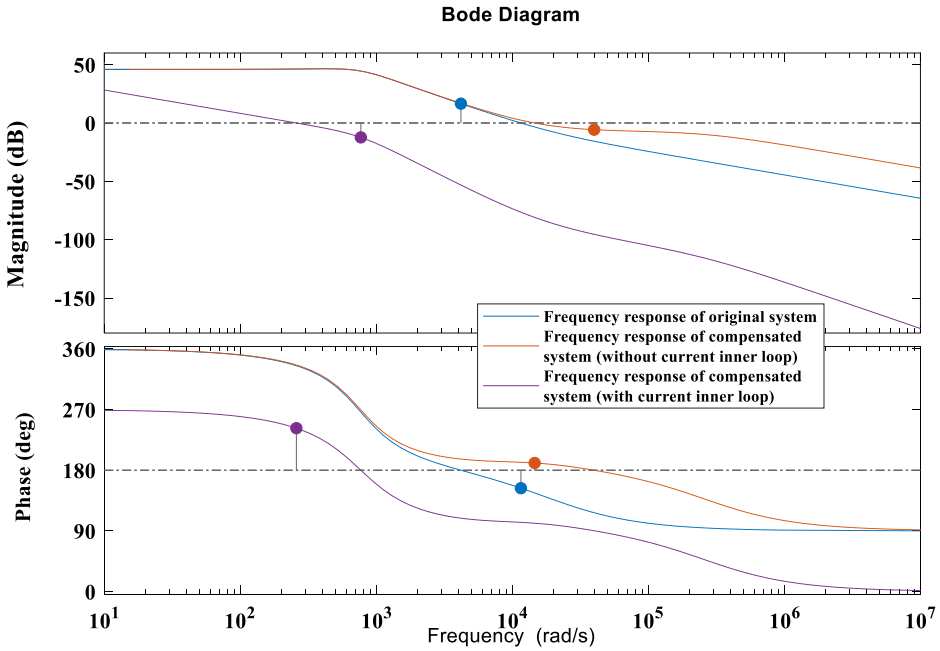

Figure 4.16: Bode plot

Table 4.3: Stability Margin

	Original system	Compensated system (without current inner loop)	Compensated system (with current inner loop)
Gain margin (dB)	-16.6	5.74	12.4
Phase margin (°)	-26.6	10.7	62.3

Figure 4.17 shows the dynamic response of DC-link voltage when PI controller is used. By comparing Figure 4.17 with Figure 4.11, it has shown that PI controller can achieve a fast dynamic response in DC-link voltage when a step change of $35V$ to $50V$ was applied. However, the performance is not as good as lead compensator. PI controller offers higher percentage overshoot during the start-up process and when step change was applied. Moreover, the settling time required to reach steady-state is about $300\ ms$, which is longer than lead compensator. Table 4.4 shows the stability margin comparison between lead compensator and PI controller. Without the inner current loop, PI controller can achieve positive gain and phase margin. In other words, the system is already stable after the compensation. However, comparing the gain and phase margin of both controllers, it shows that lead compensator can achieve better transient response, which lead to a lower overshoot and faster settling time.

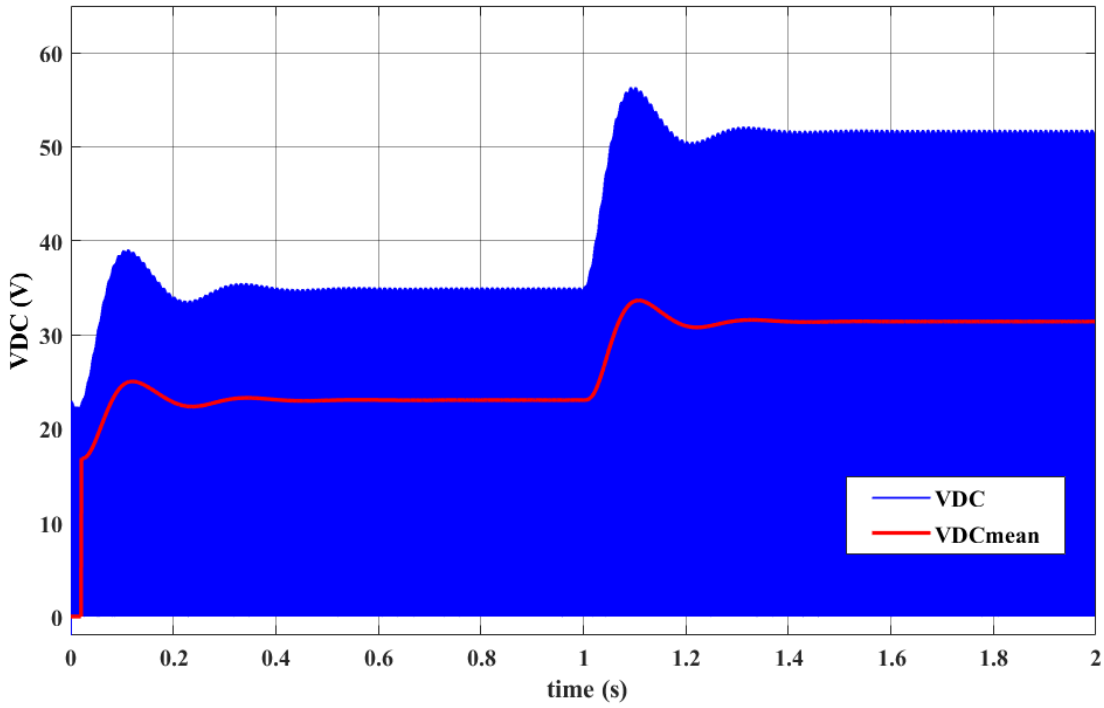

Figure 4.17: DC-link output voltage (V_{DC}) using PI controller

Table 4.4: Stability margin comparison between lead compensator and PI controller

	Compensated system using Lead Compensator (without current inner loop)	Compensated system using PI controller (without current inner loop)
Gain margin (dB)	5.74	0.702
Phase margin (°)	10.7	7.25

4.2.2 Multilevel Output Voltage Control with Different Loading Condition in CCM

All system parameters of the proposed controller (i.e., Lead Compensator) applied on the qZSI were tabulated in Table 4.5. In this section, the output voltage is kept constant, the only changes are the load resistance. A CCM system is used in this section therefore, to generate a system that operates in CCM, the inductor value has been chosen which in such a way that it could be stay as far away from the boundary condition as possible. Moreover, to reduce the ripple effect of the output voltage, the capacitor value is chosen based on equation (3.50).

Table 4.5: System Parameter

Input voltage	12V
Switching frequency, f_s	$10kHz$
Step up voltage	40V
Capacitor C_1 and C_2 value	$5.6mF$
Inductance L_1 and L_2 value	$2mH$
System AC output frequency, f_{AC}	$50Hz$
Modulation index, M	0.5

The simulation model is performed by starting out with an output load of 50 ohm. The load changed to 100 Ω at 1s and to 30 Ω at 2s. Figure 4.18 illustrates the measured qZSI DC-link voltage, V_{DC} to inhibit the external disturbances (i.e., different loading condition). It is noticed that when the AC load changed from 50 Ω to 100 Ω and from 100 Ω to 30 Ω, the DC-link voltage can be kept invariable. Noticed that the amplitude of the voltage ripple in these three cases have slight variation. When the system is operating further away from the boundary condition, the voltage ripple amplitude tends to be higher. In other words, when the system moves closer to the boundary condition, the voltage ripple tends to reduce in proportional.

Figure 4.19 shows the inductor current waveform. The graph has shown that the dynamic response of the inductor current was satisfied in accordance to the expectation. The current overshoot was low, indicates that the current stress can be remained low when lead compensator is used as the controller. When the AC load changed from 50Ω to 100Ω, the system tends to move closer to DCM, noticed that how's the inductor current react to the situation. According to Ohm's law, having a bigger load tends to reduce the inductor current, which move the system closer to the boundary condition as depicted in equation (3.41).

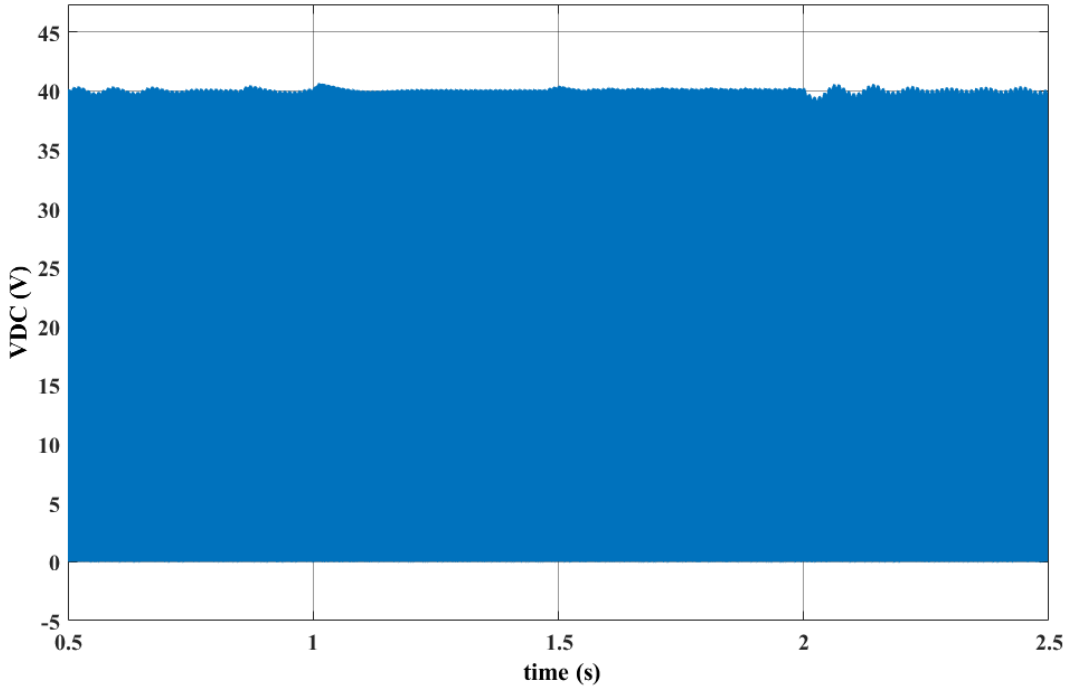

Figure 4.18: DC-link voltage with varied load loading condition

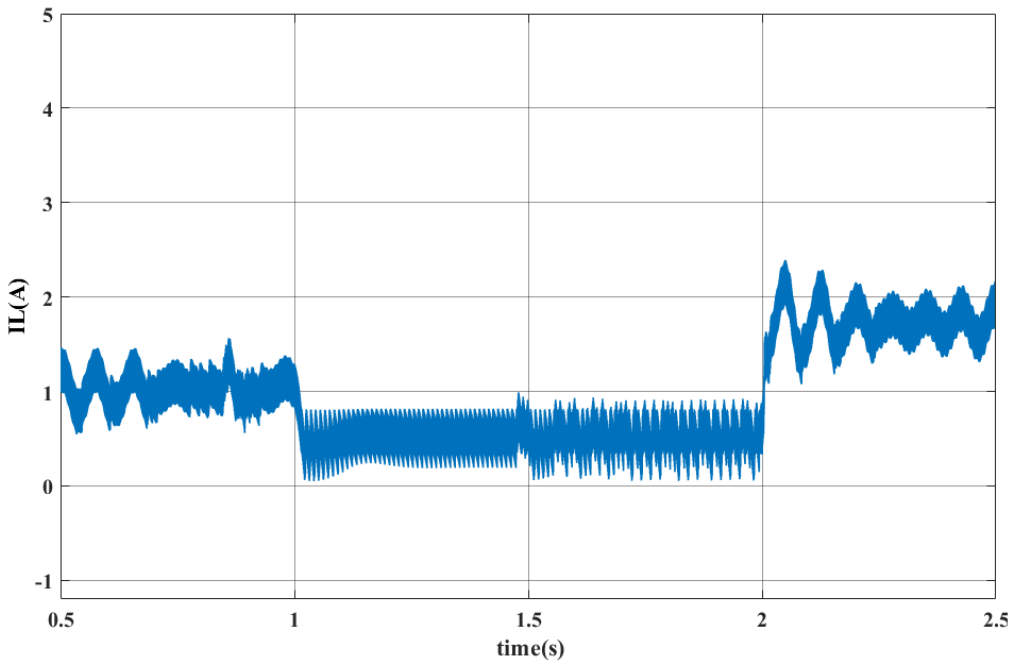

Figure 4.19: Inductor current waveform

Figure 4.20 shows how the lead compensator DC-link voltage reacts to the voltage reference. In the real-time simulation model, capacitor voltage value is obtained and fed into a control block with equation (3.23) to obtain the DC-link voltage. The reason to obtained capacitor voltage instead of DC-link voltage is because, during shoot-through interval, DC-link voltage tends to drop to zero and this might cause the entire system to turn unstable. The control system block diagram is demonstrated in Figure 4.3 in section 4.1.2.

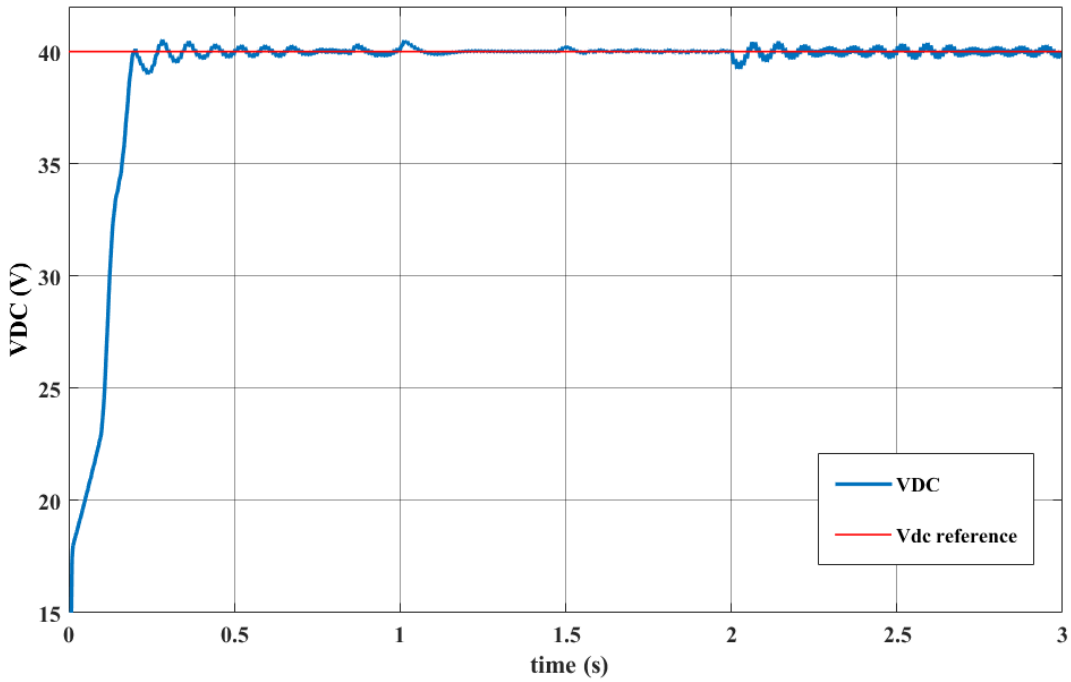

Figure 4.20: V_{DC} and V_{DC} reference waveform

Figure 4.21 shows the shoot-through duty ratio waveform. By using equation (3.21), to generate an output voltage of $40V$ from $12V$ input voltage, the shoot-through duty ratio is expected to be 0.35. The graph indicates that the shoot-through duty ratio can be maintained at a steady and constant value during the step change in loading condition. It also proven that the derived equation (3.21) is accurate.

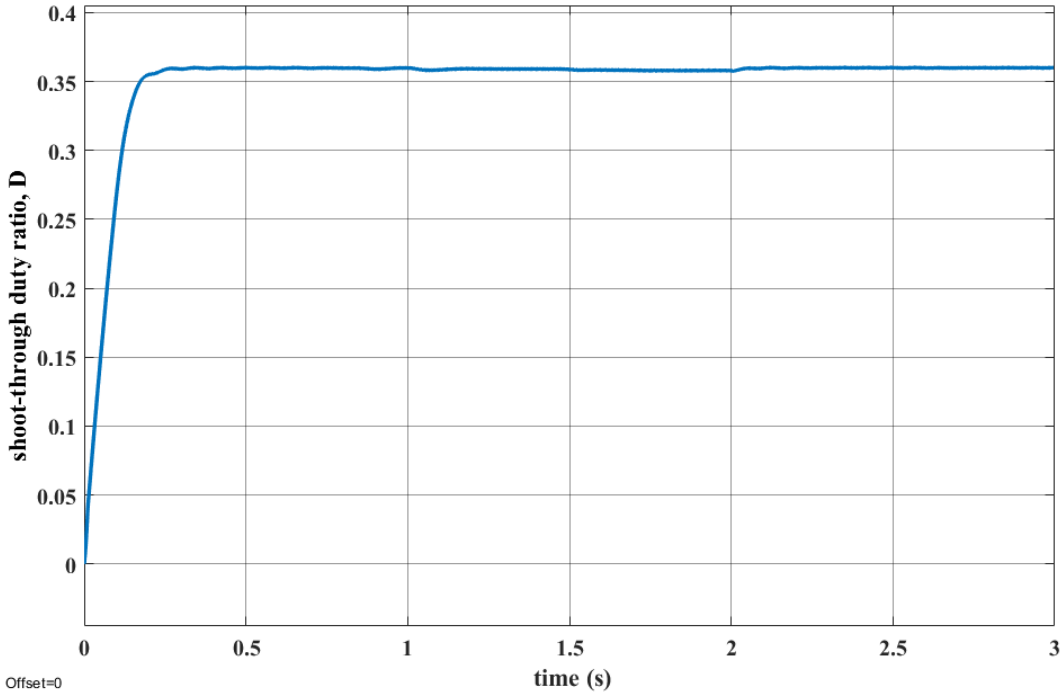

Figure 4.21: Shoot-through duty ratio waveform

A multilevel output voltage waveform has been generated by using PS-SPWM as depicted in Figure 4.23. The multilevel model is constructed according to Figure 2.1 in Simulink. Figure 4.24 shows the zoomed-in version of the output voltage waveform. In this simulation model, five-level output voltage with $80V$ peak voltage has been obtained by using two qZSI module, each with $40V$ output voltage. Each of the qZSI module is individually controlled by own DC-link voltage controller (i.e., lead compensator). The same loading condition has been applied to the circuit. The simulation results shown in Figure 4.23 has demonstrated the effectiveness of the controller in maintaining the shoot-through duty ratio and providing a smooth and stable output voltage. There is only slight distortion in the output voltage at time interval of $1s$ when the loading condition changed from 50Ω to 100Ω. At $2s$, the AC voltage distortion increased when the load changed from 100Ω to 30Ω. Nevertheless, the controller can trace the changes in the output voltage and bring it back to steady-state within a very short time interval.

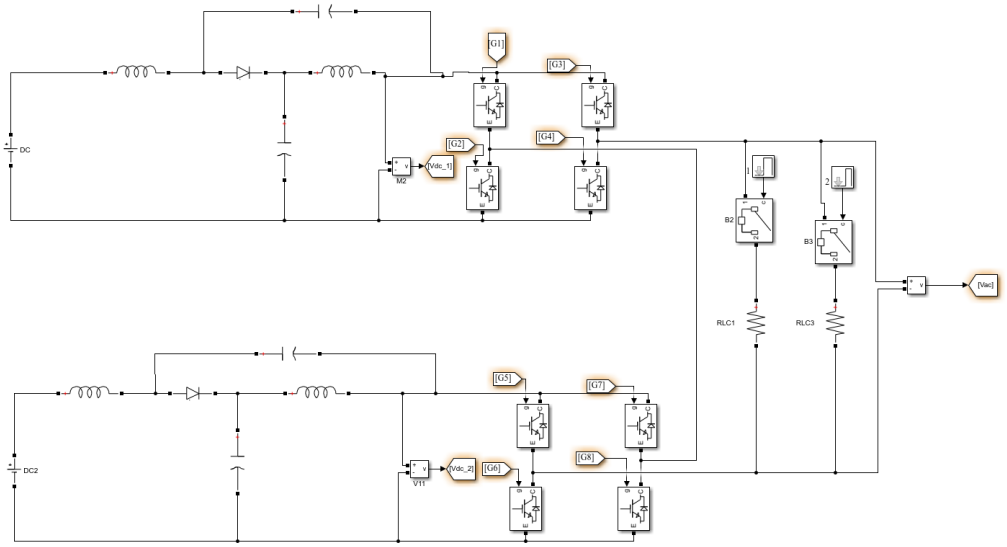

Figure 4.22: Simulink Model of multilevel qZSI

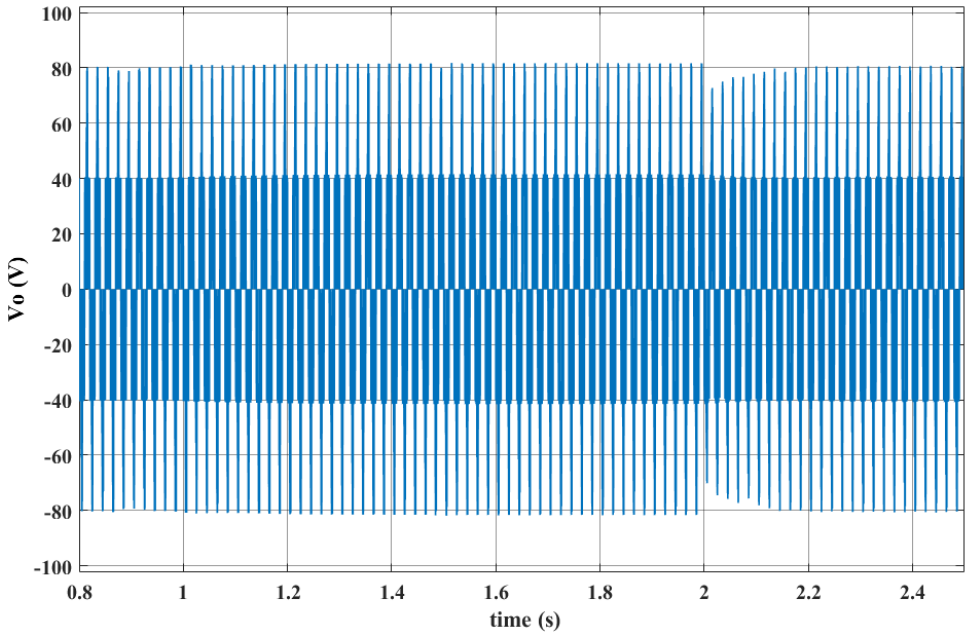

Figure 4.23: AC output voltage, V_{AC}

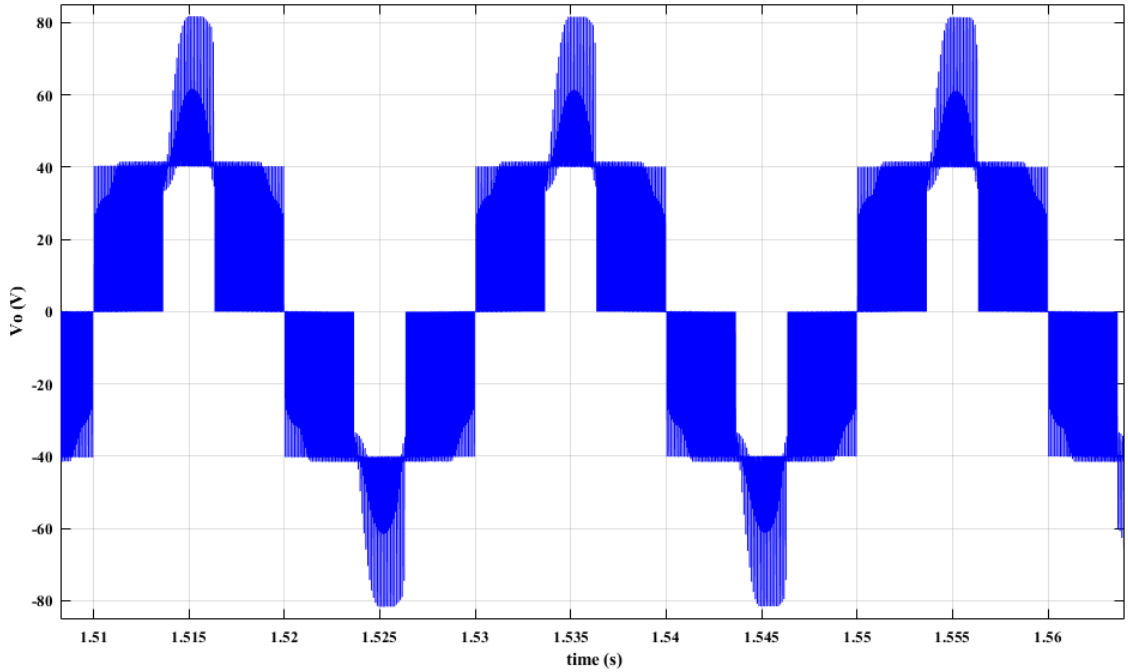

Figure 4.24: Zoomed-in of AC output voltage

Figure 4.25 shows the AC output current waveform. The waveform indicates that the controller has performed an excellent job, not only maintaining a stable DC-link voltage, but also keeps the AC output current stable. Notice how the AC current reacts to the changes in the loading condition. Ohm's law is applied when calculating the output AC current value. The larger the load, the lower the output AC current. Referring to equation (3.46), AC current has direct impact to the inductor current. Hence, it also proofs that the principle behind equation (3.41) is valid; qZSI which operates in larger loading condition tends to move closer to DCM zone.

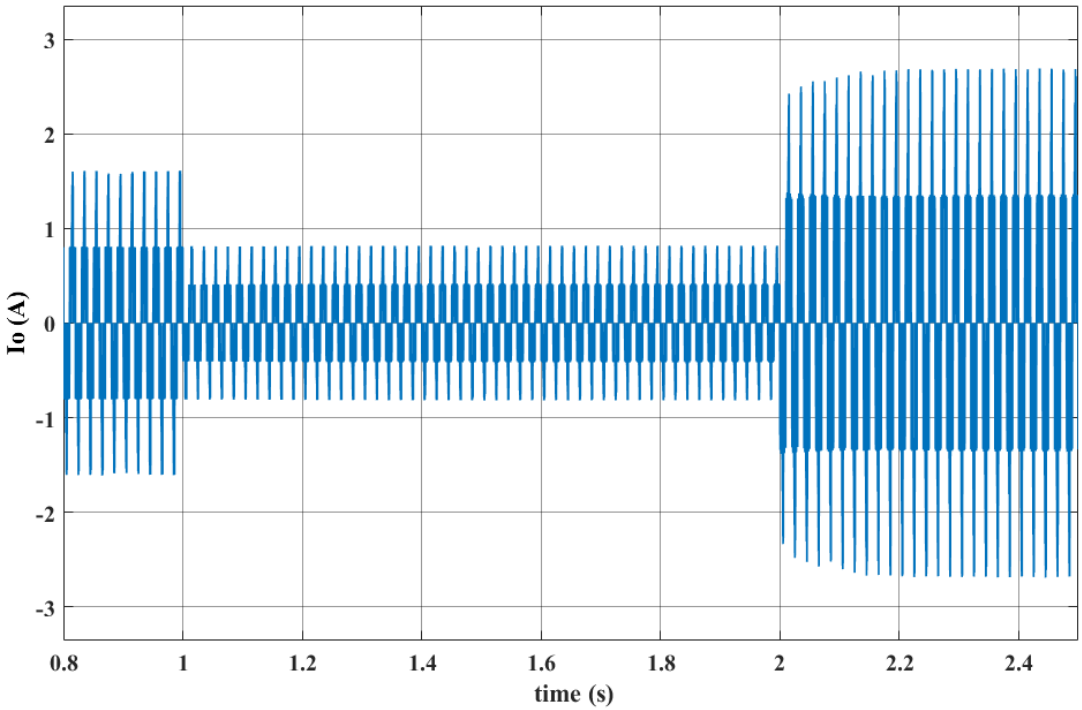

Figure 4.25: AC output current, I_o

4.3 Summary

This chapter presents the detail mathematical derivation of qZSI large and small-signal models. To achieve robust dynamic and transient response, lead compensator is chosen as the controller to be used in DC-link voltage control. The performance of the lead compensator has shown improvement over PI controller and the result is demonstrated in section 4.2.1. The controller performance has been performed and reviewed in different circumstances. The presented results include when qZSI operates in DCM and CCM mode, which are shown in section 4.2.1 and section 4.2.2, respectively. The controller was tested with step change in the DC-link voltage reference and the results were satisfying. Dynamic response can be achieved within $50ms$, which has far beyond the expected dynamic response stated in objective (i.e., $200ms$). Later, in section 4.2.2, the simulation model was tested with a step change in loading condition. The controller has achieved a very fast response when the step change is applied. The topology is later extended to multilevel qZCHI to generate multilevel output voltage/current.

Chapter 5 : Power Quality Improvement in qZSI

Since qZSI is an emerging topology that is normally applied to PV power system, it is utmost important to ensure unity power factor as well as low harmonic distortion from the generated output voltage and current when integrating qZSI to the grid. The foregoing topology might inherent voltage and power imbalance to the grid. In this chapter, the mathematical modelling of PV-based qZSI STATCOM system is prosecuted.

First, in section 5.1, the basic MPPT algorithms are introduced to balance the fluctuation of PV power. The basic MPPT algorithm has been integrated to qZSI module and the simulation results are shown in section 5.5.1. In this section, the MPPT algorithm is applied based on the previous literature [46-49] to adjust the shoot-through duty cycle of the converter. However, in future simulation work, instead of tuning the duty cycle of the converter, the MPPT algorithm will be merged with converter STATCOM system to generate the modulation index of the converter's IGBT switches. Several literatures have demonstrated different approaches to tune the modulation index using linear control (i.e., PI controller) [28, 49].

Secondly, section 5.2 introduces the qZSI based STATCOM system control scheme to improve the power quality of the inverter as well as regulating the output current/voltage. The STATCOM controller is synthesized and combined with DC-link voltage controller mentioned in chapter 4 (i.e., lead compensator) to advocate and limit the fluctuation of the output voltage/current. Also, the main feature of the STATCOM system is to minimize the phase angle difference between the grid voltage and grid current (i.e., before the PCC). In other words, the purpose of the entire system is to make sure that the power factor distributed can be compensated to as closed to unity as possible. The simulation results are illustrated in section 5.5.2.

Section 5.3 describes the modelling of two energy storing battery-based qZSI. This includes the derivation of qZSI transfer function in both large (i.e., section 5.3.1) and small-signal analysis (i.e., section 5.3.2). The verification of the derived transfer function will be done in future work. Finally, to fully develop a PV-based qZSI model with

STATCOM system, MPPT algorithm, STATCOM and DC-link voltage controller must be combined and operates concurrently. Section 5.4 covers the system modelling of the referred control system.

5.1 MPPT algorithm

In a PV system, the changes in solar irradiance and temperature of the environment causes intensive fluctuation of the input power. MPPT algorithms are implemented to resolve the power fluctuation issues when power conditioning circuit is connected between the PV system and the load. In other words, the algorithms are used to extract maximum power from the PV system based on different solar irradiance and temperature, then inject it to the load side. Several MPPT algorithms have been proposed to extract the maximum power from the PV-panel, includes Perturb and Observe (P&O) algorithm [50], Incremental and conductance (I&C) algorithm [47], constant voltage and parasitic capacitance algorithm [46, 48] etc.

In a grid-connected PV system, to track the MPP of a PV-array, the capacitor voltage of qZSI is controlled to be constant. The output voltage of a PV-array decreases from the set value of DC-link reference voltage to the MPP by increasing the shoot-through duty ratio [2]. At constant temperature, the changes of solar irradiance will result in a large change in PV current at MPP [51]. With a little variation in the temperature, the MPPT controller ensures that the DC-link voltage can be remained in a stable environment. Contrarily, at MPP, PV voltage changes according to the changes of temperature [51]. The resultant of PV current will ultimately distort the amplitude DC-link peak voltages, resulting in unstable system to occur. Figure 5.1 shows the P&O method block diagram for converter topology.

In Figure 5.1, the shoot-through duty ratio of qZSI is increased when the power of current cycle is larger than the power of qZSI, one switching cycle before. This switching cycle can be referred to how much the time taken for the MPPT to react to the changes in irradiance or temperature. The *i*-term from Figure 5.1 defines the cycle number. In this

chapter, P&O algorithm is chosen due to its structural simplicity and easy to be implemented. Nevertheless, further literature reviews must be taken to evaluate the performance of each method and a more detail and in-depth study has to be taken in the future work.

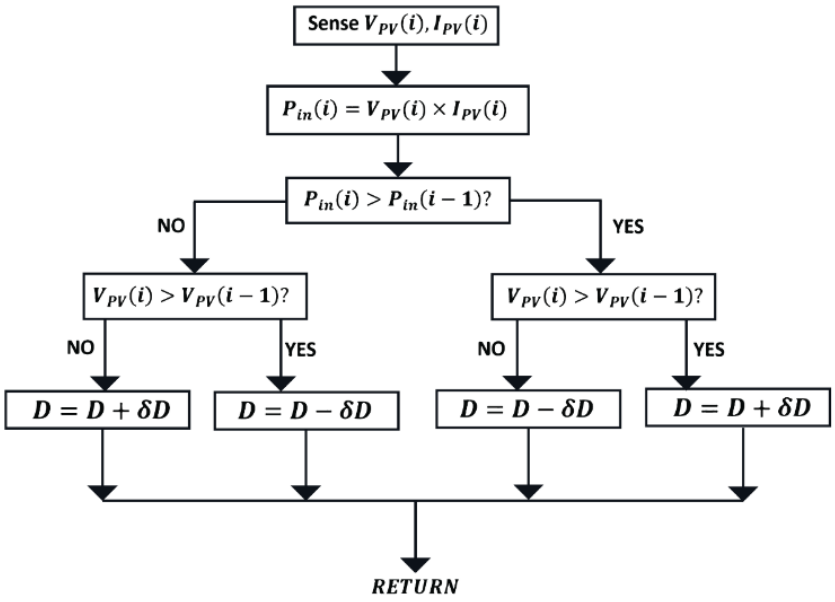

Figure 5.1: P&O method for qZSI [48]

5.2 qZSI based STATCOM system

Power quality and efficiency issues has becoming one of the major concern in recent years. Low power factor, excessive harmonic and transient oscillations that occurred in the power transmission and distributions are common adversity in conventional power inverter. The AC output that consists of reactive loads, which naturally provide with low power factor, will draw excessive reactive power (VAR) restricting the maximum active power transfer and hence resulting in a low efficiency, yet high power losses to the power transmission and distribution systems. Therefore, it is crucial to improve the voltage stability as well as power quality of the power inverter under both contingency and normal operating conditions. The conventional voltage-source inverter-based STATCOM has been one of the most predominant solution to provide the VAR compensation [52]. Among different multilevel STATCOM topologies, cascade H-bridge Based (CHB) configuration has received a lot of attention from researchers [53].

Several methods have been reported in literature, including the classical linear control strategies to others non-linear control scheme [53]. For the linear control strategies, the most common way to perform power quality control is to use Park Transformation to map the system to the Synchronous Reference Frame (SRF) and then apply traditional linear controller such as PI or PID controller. In a STATCOM based converter network, the amplitude and phase angle of the inverter's output voltage and current is measured and will be controlled with respect to the AC-source voltage reference.

In [54], the author presented a STATCOM based inverter system using i_{oq}^{*} algorithm and the associate control scheme is presented in Figure 5.2. The proposed algorithm enhances the transient performance of the closed-loop system by using only P controller and minimizes the STATCOM reactive current ripples. The STATCOM system is implemented to control the reactive power (VAR) compensation and the grid power factor correction at the PCC. The output current will be converted into dq vector and implemented into reactive current reference algorithm proposed by Law in [55]. The

algorithm is incorporated as STATCOM main system to generate the desired modulation index, m_a as in equation (5.1).

$$m_a = \frac{v_o^*}{2} = \frac{\sqrt{(v_{od}^*)^2 + \left(v_{oq}^*\right)^2}}{2} \tag{5.1}$$

Where

$$\begin{aligned} v_{od}^*(k) = v_{pccd}(k) - R_f i_{od}(k) + \frac{wL_f}{2}\left[i_{oq}(k) + i_{lq}(k)\right] \\ + \frac{wL_f}{2}\left[i_{oq}(k) + i_{lq}(k)\right] - K_{p_{id}}[-i_{od}(k)] \end{aligned} \tag{5.2}$$

$$\begin{aligned} v_{oq}^*(k) = -R_f i_{oq}(k) - \frac{wL_f}{2}[i_{od}(k) + i_{od}^*(k)] \\ - K_{p_{iq}}[\left(i_{lq}(k) + i_{oq}^*\right) - i_{oq}(k)] \end{aligned} \tag{5.3}$$

i_{od} and i_{oq} are the active and reactive current passing through the coupling impedance Z_f (i.e., $Z_f = L_f + r_f$). w is the grid voltage angular frequency and v_{pccd} is the d-axis grid voltage.

The P controller in equation (5.3) has a transfer function as stated in (5.4).

$$K_{p_{i(d,q)}} = \frac{L_f}{T_{i(d,q)}} + \frac{R_f}{2} \tag{5.4}$$

Equation (5.5) represents the reactive current reference algorithm proposed in [56].

$$i_{oq}^* = \frac{1 - \left(wL_f i_{cd}^*\right)^2 - \left(wL_f i_{lq}\right)^2 - v_{pccd}^2}{2V_{pccd} wL_f} \tag{5.5}$$

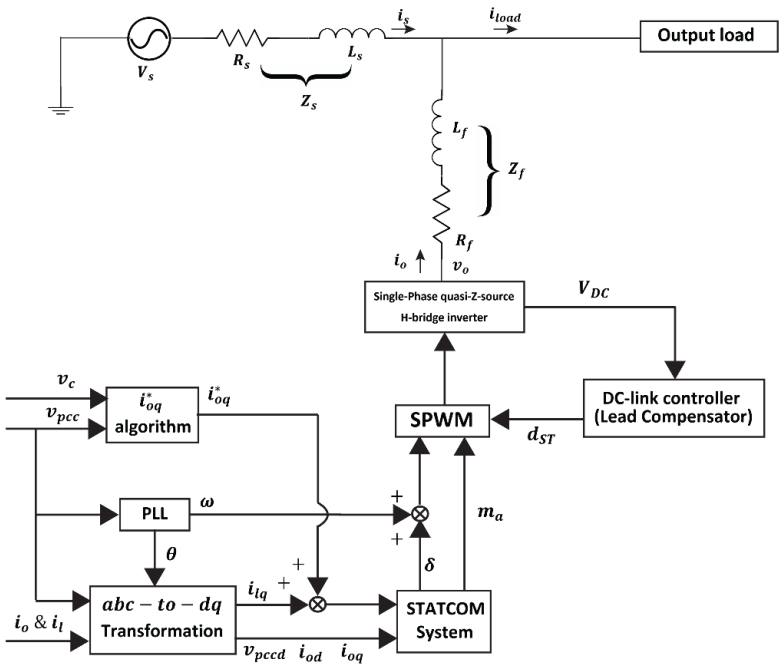

Figure 5.2: Single-phase qZSI based STATCOM system with i_{oq} current control algorithm

5.3 Modelling of Two Energy Storing Battery-based qZSI model

The fluctuations of solar power in nature leads to numerous power quality issues in power transmission system. The variation in solar irradiation and temperature causes large diversity of the output DC-link voltage and lead to high voltage stress to the inverter, as well as the output network. To domesticate this issue, energy storing battery-based system is incorporated into the power converter topology to buffer and smoothen the fluctuations of PV power. The incorporation of the energy storing battery to the inverter system allows the qZS to smoothen the grid-tie power and compensate the difference between PV power and the load demand. Also, the extra unused energy can be stored in the battery for later usage. However, there is an issue when implementing energy storing battery in inverter topology; overcharge or discharge to the level below the battery limits [57]. [57] and [58] have documented different approaches to solve the stated problem. However, all the ever-presented literature only included one energy storing battery to qZS, non-of them have utilized both the capacitors to perform compensation on the PV power. This section consists of the modelling of two energy storing battery-based qZSI model. For application-wise, the proposed energy storing battery-based qZS topology can be adopted into a power bank system for household or domestic usage (i.e., charging of EVs). The following section includes the modelling of two battery-based qZS transfer function as well as its small-signal analysis.

5.3.1 Derivation of two energy storing battery-based qZSI transfer function

Figure 5.3 below shows the two energy storing battery-based qZS model.

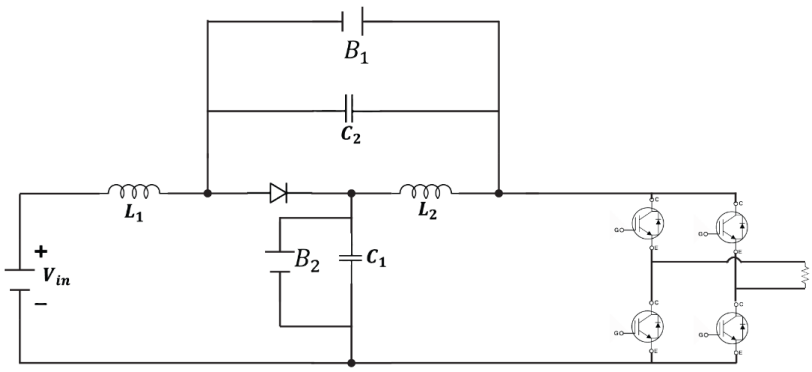

Figure 5.3: Two energy storing battery-based qZS model

Figure 5.4 depicts the battery-based qZS model in shoot-through state. During this state, the diode will be open-circuited. The foregoing diagram is redrawn in Figure 5.5 for simplicity and better understanding.

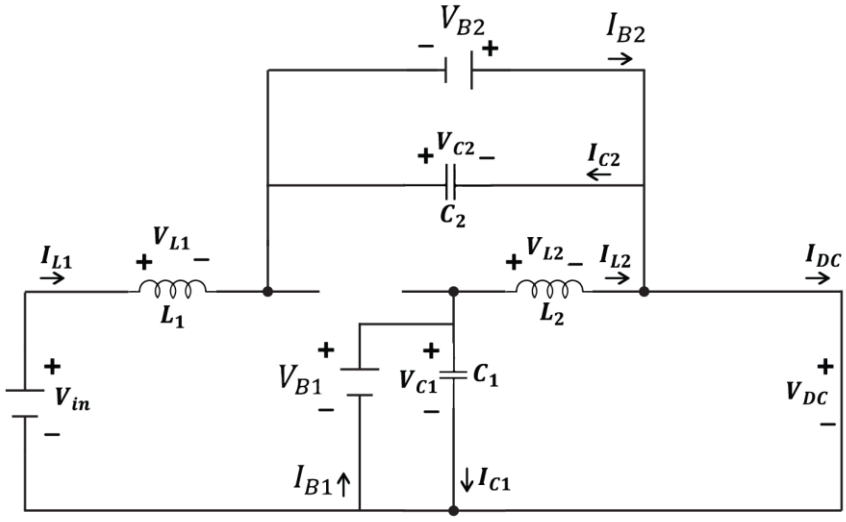

Figure 5.4: Two battery-based qZSI in shoot-through state

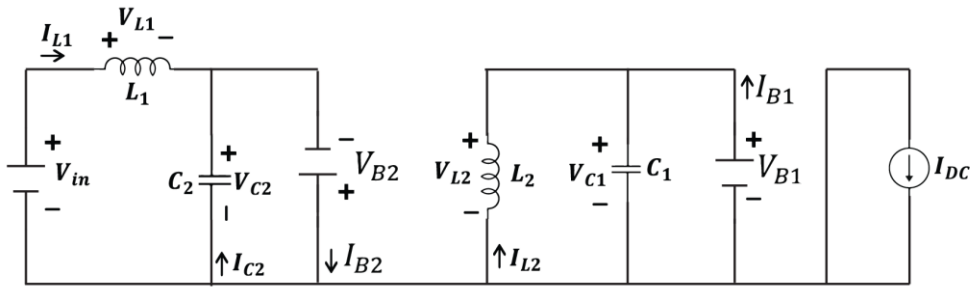

Figure 5.5: Simplified version of two battery-based qZSI model in shoot-through state

Applying KCL to the left-hand node in Figure 5.5 (i.e., the voltage loop on the left-hand side of the circuit diagram), obtained the following equations:

$$I_{L1} = I_{B2} - I_{C2}$$

$$C_2\left(\frac{dV_{C2}}{dt}\right) = I_{B2} - I_{L1} \tag{5.6}$$

Where I_{L1} is the current flowing through inductor L_1, I_{C2} is the current flowing through capacitor C_2, I_{B2} is the current generated or absorbed by the energy storing battery B_2 and V_{C2} is the capacitor C_2 voltage. Notice all the parameters included in this section are represented in their peak value.

Applying KCL to the right-hand node in Figure 5.5.

$$I_{L2} + I_{C1} = I_{B1}$$

$$C_1\left(\frac{dV_{C1}}{dt}\right) = I_{B1} - I_{L2} \tag{5.7}$$

Where I_{L2} is the current flowing through inductor L_2, I_{C1} is the current flowing through capacitor C_1, I_{B1} is the current generated or absorbed by the energy storing battery B_1 and V_{C1} is the capacitor C_1 voltage.

Applying KVL to loop 1,

$$V_{in} - V_{L1} + V_{C2} = 0$$

$$V_{L1} = V_{in} + V_{C2} \tag{5.8}$$

$$V_{C2} = V_{B2} \tag{5.9}$$

$$V_{L1} = V_{in} + V_{B2} \tag{5.10}$$

$$L_1\left(\frac{dI_{L1}}{dt}\right) = V_{in} + V_{B2} \tag{5.11}$$

Applying KVL to loop 2, obtained,

$$V_{L2} = V_{C1} = V_{B1} \tag{5.12}$$

$$L_2\left(\frac{dI_{L2}}{dt}\right) = V_{C1} = V_{B1} \tag{5.13}$$

Applying KCL to the output current node,

$$I_{DC} = I_{B2} - I_{C2} + I_{L2} \tag{5.14}$$

And substitute equation (5.6) into equation (5.14)

$$I_{DC} = I_{L1} + I_{L2} \tag{5.15}$$

We know that

$$V_{DC} + V_{L2} - V_{C1} = 0$$

$$V_{L2} = V_{C1}$$

Therefore, in shoot-through state,

$$V_{DC} = 0 \tag{5.16}$$

Rearranging equation (5.6), (5.7), (5.11) and (5.13) obtained the following state space equations,

$$\begin{bmatrix} L_1 & 0 & 0 & 0 \\ 0 & L_2 & 0 & 0 \\ 0 & 0 & C_1 & 0 \\ 0 & 0 & 0 & C_2 \end{bmatrix} \begin{bmatrix} \dot{\imath_{L1}}(t) \\ \dot{\imath_{L2}}(t) \\ \dot{v_{C1}}(t) \\ \dot{v_{C2}}(t) \end{bmatrix} = \begin{bmatrix} 0 & 0 & 0 & 1 \\ 0 & 0 & 1 & 0 \\ 0 & -1 & 0 & 0 \\ -1 & 0 & 0 & 0 \end{bmatrix} \begin{bmatrix} i_{L1}(t) \\ i_{L2}(t) \\ v_{C1}(t) \\ v_{C2}(t) \end{bmatrix} + \begin{bmatrix} 1 & 0 \\ 0 & 0 \\ 0 & 0 \\ 0 & 0 \end{bmatrix} \begin{bmatrix} v_{in}(t) \\ i_{DC}(t) \end{bmatrix} + \begin{bmatrix} 0 & 0 \\ 0 & 0 \\ 1 & 0 \\ 0 & 1 \end{bmatrix} \begin{bmatrix} i_{B1}(t) \\ i_{B2}(t) \end{bmatrix} \quad (5.17)$$

In non-shoot-through state, the qZSI battery system can be drawn in Figure 5.6 below.

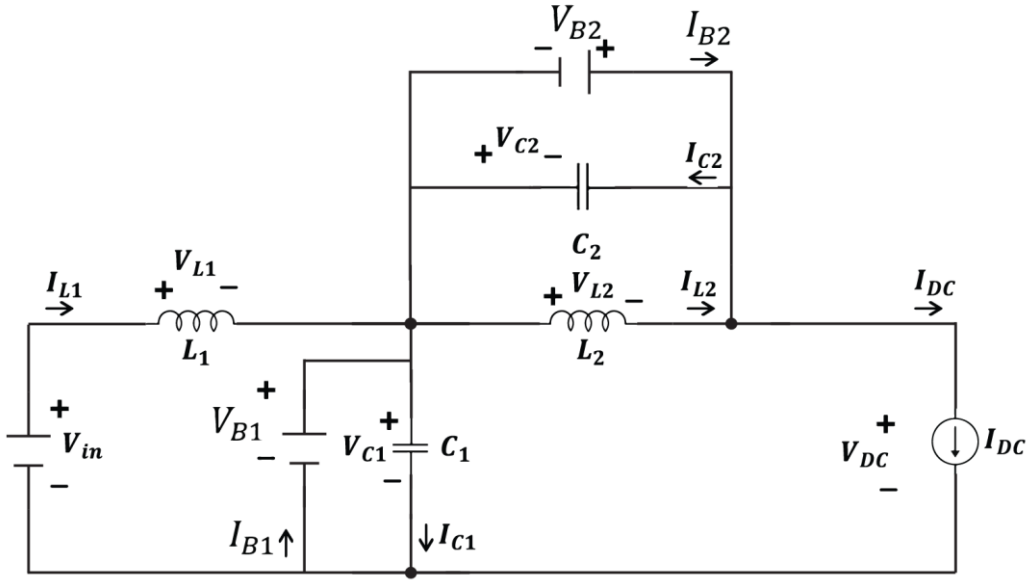

Figure 5.6: Two battery-based qZSI in non-shoot-through state

Applying KCL to node where I_{L2}, I_{B2}, I_{C2} and I_{DC} present, obtained equation (5.18) as follows.

$$I_{L2} + I_{B2} - I_{C2} - I_{DC} = 0$$

$$C_2\left(\frac{dV_{C2}}{dt}\right) = I_{L2} + I_{B2} - I_{DC} \quad (5.18)$$

Applying KCL to node where I_{B1}, I_{L1}, I_{C1} and I_{DC} present, the following equation is established.

$$I_{B1} + I_{L1} - I_{C1} - I_{DC} = 0$$

$$C_1\left(\frac{dV_{C1}}{dt}\right) + I_{L1} + I_{B1} - I_{DC} = 0 \tag{5.19}$$

Applying KVL to Figure 5.6, equation (5.20) to equation (5.22) are formed.

$$V_{B1} = V_{C1} \tag{5.20}$$

Applying KVL to the input side of Figure 5.6, obtained equation (5.21) and (5.22).

$$V_{in} - V_{L1} - V_{C1} = 0$$

$$V_{in} = V_{L1} + V_{C1}$$

$$L_1\left(\frac{dI_{L1}}{dt}\right) = V_{in} - V_{C1} \tag{5.21}$$

$$V_{L2} = -V_{C2} = -V_{B2}$$

$$L_2\left(\frac{dI_{L2}}{dt}\right) = -V_{C2} = -V_{B2} \tag{5.22}$$

Applying KCL to the node where I_{diode} is present,

$$I_{diode} + I_{B1} - I_{C1} - I_{L2} = 0$$

$$I_{diode} = I_{C1} + I_{L2} - I_{B1} \tag{5.23}$$

Substitute equation (5.19) into equation (5.23), we get

$$I_{diode} = I_{L1} + I_{DC} + I_{L2} \tag{5.24}$$

Rearranging the equation (5.18), (5.19), (5.21) and (5.22), the state space equation of battery-based qZSI in non-shoot-through state can be written as:

$$\begin{bmatrix} L_1 & 0 & 0 & 0 \\ 0 & L_2 & 0 & 0 \\ 0 & 0 & C_1 & 0 \\ 0 & 0 & 0 & C_2 \end{bmatrix} \begin{bmatrix} \dot{i_{L1}}(t) \\ \dot{i_{L2}}(t) \\ \dot{v_{C1}}(t) \\ \dot{v_{C2}}(t) \end{bmatrix} = \begin{bmatrix} 0 & 0 & -1 & 0 \\ 0 & 0 & 0 & -1 \\ 1 & 0 & 0 & 0 \\ 0 & 1 & 0 & 0 \end{bmatrix} \begin{bmatrix} i_{L1}(t) \\ i_{L2}(t) \\ v_{C1}(t) \\ v_{C2}(t) \end{bmatrix} + \begin{bmatrix} 1 & 0 \\ 0 & 0 \\ 0 & -1 \\ 0 & -1 \end{bmatrix} \begin{bmatrix} v_{in}(t) \\ i_{DC}(t) \end{bmatrix} + \begin{bmatrix} 0 & 0 \\ 0 & 0 \\ 1 & 0 \\ 0 & -1 \end{bmatrix} \begin{bmatrix} i_{B1}(t) \\ i_{B2}(t) \end{bmatrix} \quad (5.25)$$

Throughout one switching cycle, the average equation of capacitor current (i.e., I_{C1} and I_{C2}) are equate to zero. Therefore:

$$\langle I_{C1} \rangle = (I_{B1} - I_{L2}) D_{ST} T_S + (1 - D_{ST}) T_S (I_{L1} + I_{B1} - I_{DC}) = 0$$

$$I_{B1} - I_{L2} D_{ST} + (1 - D_{ST}) I_{L1} - (1 - D_{ST})(I_{DC}) = 0 \quad (5.26)$$

Where D_{ST} is the duty ratio over one switching cycle, whereas T_S is the time taken to complete one switching cycle.

$$\langle I_{C2} \rangle = D_{ST} (I_{B2} - I_{L1}) T_S + (1 - D_{ST}) T_S (I_{L2} + I_{B2} - I_{DC}) = 0$$

$$I_{DC} = \frac{I_{B2} - D_{ST} I_{L1} + (1 - D_{ST}) I_{L2}}{1 - D_{ST}} \quad (5.27)$$

Substitute equation (5.27) into equation (5.26), the equation can be simplified to

$$I_{L1} = I_{L2} + (I_{B2} - I_{B1}) \quad (5.28)$$

Throughout one switching cycle, the average equation of the inductor voltage (i.e., V_{L1} and V_{L2}) are equate to zero. Therefore:

$$\langle V_{L1} \rangle = D_{ST} T_S (V_{in} + V_{C2}) + (1 - D_{ST}) T_S (V_{in} - V_{C1}) = 0$$

$$V_{C1} - V_{in} = D_{ST} (V_{C1} + V_{C2}) \quad (5.29)$$

$$\langle V_{L2} \rangle = D_{ST} T_S (V_{C1}) + (1 - D_{ST}) T_S (-V_{C2}) = 0$$

$$V_{C2} = D_{ST} V_{C1} + D_{ST} V_{C2} \quad (5.30)$$

Substitute equation (5.30) into equation (5.29), we get

$$V_{C1} - V_{in} = V_{C2} \quad (5.31)$$

$$V_{in} = V_{C1} - V_{C2} \quad (5.32)$$

$$V_{C1} = V_{C2} + V_{in} \tag{5.33}$$

Substitute equation (5.31) into equation (5.30),

$$\frac{V_{C1}}{V_{in}} = \frac{1 - D_{ST}}{1 - 2D_{ST}} \tag{5.34}$$

And by substitute equation (5.33) into equation (5.34), obtained the following equations

$$\frac{V_{C2}}{V_{in}} = \frac{D_{ST}}{1 - 2D_{ST}} \tag{5.35}$$

In non-shoot-through state, the DC-link voltage can be defined as

$$V_{DC} = V_{C1} + V_{C2} \tag{5.36}$$

Therefore,

$$\frac{V_{DC}}{V_{in}} = \frac{1}{1 - 2D_{ST}} \tag{5.37}$$

By looking at equation (5.34), (5.35) and (5.37) and compare with the equation (3.19) to equation (3.21) in section 3.1.1, noticed that by adding two batteries to the qZSI model, the qZSI DC-link transfer function remained unchanged. In other words, with additional two energy storing battery, it does not affect the qZSI in generating the DC-link output voltage based on the shoot-through duty cycle.

5.3.2 Small-signal analysis of two energy storing battery-based qZSI

Figure 5.7 shows the small-signal model of battery-based qZSI model in shoot-through state to derive its transfer function. In small-signal analysis of qZSI model, the stray resistance (i.e., r_1 and r_2) are included in inductors L_1 and L_2 and the equivalent series resistance (i.e., R_1 and R_2) are included in the capacitors C_1 and C_2. It is assumed that, $r = r_1 = r_2$ and $R = R_1 = R_2$.

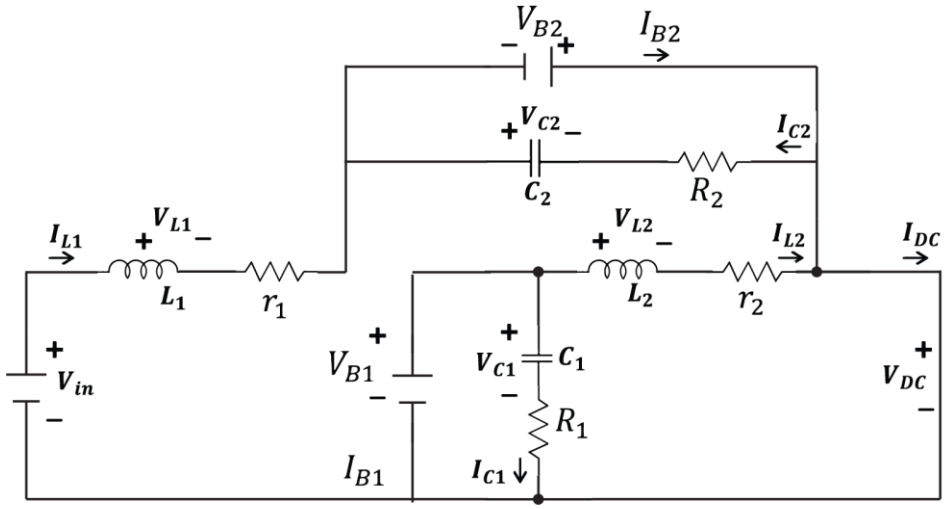

Figure 5.7: Small-signal model of two battery-based qZSI in shoot-through state

Applying KVL to Figure 5.7:

$$V_{C1} + I_{C1}R - V_{DC} - I_{L2}r - V_{L2}$$

$$\frac{di_{L2}}{dt} = -\frac{R+r}{L} i_{L2} + \frac{1}{L} V_{C1} + \frac{R}{L} I_{B1} \tag{5.38}$$

Applying KVL to second loop in Figure 5.7:

$$V_{C1} + I_{C1}R - V_{B1} = 0$$

$$V_{B1} = V_{C1} + I_{C1}R \tag{5.39}$$

Applying KVL to the loop that contains the second battery,

$$V_{in} - V_{L1} - I_{L1}r + V_{C2} + I_{C2}R = 0$$

$$\frac{di_{L1}}{dt} = -\frac{r+R}{L}i_{L1} + \frac{V_{C2}}{L} + \frac{V_{in}}{L} + \frac{R_2}{L}I_{B2} \tag{5.40}$$

Applying KVL

$$V_{C2} + I_{C2}R - V_{B2} = 0$$

$$V_{B2} = V_{C2} + I_{C2}R \tag{5.41}$$

Applying KCL:

$$I_{C1} = -I_{L2} + I_{B1}$$

$$\frac{dV_{C1}}{dt} = -\frac{1}{C}I_{L2} + \frac{1}{C}I_{B1} \tag{5.42}$$

Writing equation (5.38) to (5.42) into state space equation, we obtained

$$\begin{bmatrix} L_1 & 0 & 0 & 0 \\ 0 & L_2 & 0 & 0 \\ 0 & 0 & C_1 & 0 \\ 0 & 0 & 0 & C_2 \end{bmatrix} \begin{bmatrix} \dot{i_{L1}}(t) \\ \dot{i_{L2}}(t) \\ \dot{v_{C1}}(t) \\ \dot{v_{C2}}(t) \end{bmatrix} = \begin{bmatrix} -\frac{r+R}{L} & 0 & 0 & \frac{1}{L} \\ 0 & -\frac{r+R}{L} & \frac{1}{L} & 0 \\ 0 & -\frac{1}{C} & 0 & 0 \\ -\frac{1}{C} & 0 & 0 & 0 \end{bmatrix} \begin{bmatrix} i_{L1}(t) \\ i_{L2}(t) \\ v_{C1}(t) \\ v_{C2}(t) \end{bmatrix} + \begin{bmatrix} \frac{1}{L} & 0 \\ 0 & 0 \\ 0 & 0 \\ 0 & 0 \end{bmatrix} \begin{bmatrix} v_{in}(t) \\ i_{DC}(t) \end{bmatrix} + \begin{bmatrix} 0 & \frac{R}{L} \\ \frac{R}{L} & 0 \\ 0 & \frac{1}{C} \\ \frac{1}{C} & 0 \end{bmatrix} \begin{bmatrix} i_{B1}(t) \\ i_{B2}(t) \end{bmatrix} \tag{5.43}$$

Figure 5.8 shows the two battery-based qZSI small-signal model in non-shoot-through state (i.e., active-state).

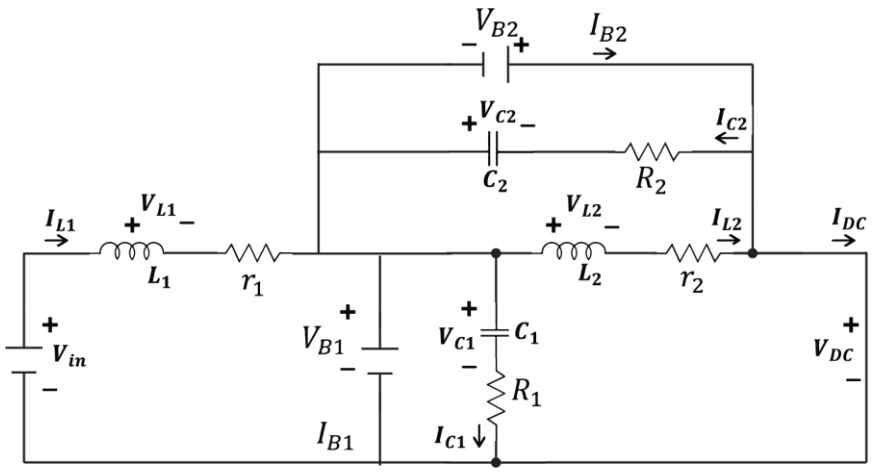

Figure 5.8: Small-signal model of two battery-based qZSI in non-shoot-through state

Applying KCL and KVL to the small-signal model in Figure 5.8, we can obtain the equations as below.

$$I_{C1} - I_{B1} + I_{DC} - I_{L1} = 0$$

$$\frac{dV_{C1}}{dt} = \frac{1}{C}I_{L1} - \frac{1}{C}I_{DC} + \frac{1}{C}I_{B1} \tag{5.44}$$

$$I_{DC} - I_{L2} + I_{C2} - I_{B2} = 0$$

$$\frac{dV_{C2}}{dt} = \frac{1}{C}I_{L2} - \frac{1}{C}I_{DC} + \frac{1}{C}I_{B2} \tag{5.45}$$

$$V_{in} - V_{L1} - I_{L1}r - V_{C1} - I_{C1}R = 0$$

$$\frac{di_{L1}}{dt} = -\frac{r+R}{L}I_{L1} - \frac{V_{C1}}{L} + \frac{R}{L}I_{DC} - \frac{R}{L}I_{B1} + \frac{V_{in}}{L} \tag{5.46}$$

$$V_{L2} + I_{L2}r + I_{C2}R + V_{C2} = 0$$

$$\frac{di_{L2}}{dt} = -\frac{r+R}{L}I_{L2} - \frac{V_{C2}}{L} + \frac{R}{L}I_{DC} - \frac{R}{L}I_{B2} \tag{5.47}$$

Writing equation (5.44) to (5.47) into state-space equation, obtained as per (5.48) below.

$$\begin{bmatrix} L_1 & 0 & 0 & 0 \\ 0 & L_2 & 0 & 0 \\ 0 & 0 & C_1 & 0 \\ 0 & 0 & 0 & C_2 \end{bmatrix} \begin{bmatrix} \dot{i_{L1}}(t) \\ \dot{i_{L2}}(t) \\ \dot{v_{C1}}(t) \\ \dot{v_{C2}}(t) \end{bmatrix} = \begin{bmatrix} -\frac{r+R}{L} & 0 & -\frac{1}{L} & 0 \\ 0 & -\frac{r+R}{L} & 0 & -\frac{1}{L} \\ \frac{1}{C} & 0 & 0 & 0 \\ 0 & \frac{1}{C} & 0 & 0 \end{bmatrix} \begin{bmatrix} i_{L1}(t) \\ i_{L2}(t) \\ v_{C1}(t) \\ v_{C2}(t) \end{bmatrix} + \begin{bmatrix} \frac{1}{L} & \frac{R}{L} \\ 0 & \frac{R}{L} \\ 0 & -\frac{1}{C} \\ 0 & -\frac{1}{C} \end{bmatrix} \begin{bmatrix} v_{in}(t) \\ i_{DC}(t) \end{bmatrix} + \begin{bmatrix} -\frac{R}{L} & 0 \\ 0 & -\frac{R}{L} \\ \frac{1}{C} & 0 \\ 0 & \frac{1}{C} \end{bmatrix} \begin{bmatrix} i_{B1}(t) \\ i_{B2}(t) \end{bmatrix} \quad (5.48)$$

Equation (5.43) and (5.48) can be represented with the following simplified equation.

$$\frac{dx}{dt} = A_1 x + B_1 u$$
$$\frac{dx}{dt} = A_2 x + B_2 u \quad (5.49)$$

Where

$$x = \begin{bmatrix} i_{L1}(t) \\ i_{L2}(t) \\ v_{C1}(t) \\ v_{C2}(t) \end{bmatrix} \quad (5.50)$$

$$u = \begin{bmatrix} v_{in}(t) \\ i_{DC}(t) \\ i_{B1}(t) \\ i_{B2}(t) \end{bmatrix} \quad (5.51)$$

$$A_1 = \begin{bmatrix} -\frac{r+R}{L} & 0 & -\frac{1}{L} & 0 \\ 0 & -\frac{r+R}{L} & 0 & -\frac{1}{L} \\ \frac{1}{C} & 0 & 0 & 0 \\ 0 & \frac{1}{C} & 0 & 0 \end{bmatrix} \quad (5.52)$$

$$B_1 = \begin{bmatrix} \frac{1}{L} & \frac{R}{L} & 0 & \frac{R}{L} \\ 0 & \frac{R}{L} & \frac{R}{L} & 0 \\ 0 & -\frac{1}{C} & 0 & \frac{1}{C} \\ 0 & -\frac{1}{C} & \frac{1}{C} & 0 \end{bmatrix} \quad (5.53)$$

$$A_2 = \begin{bmatrix} -\frac{r+R}{L} & 0 & 0 & \frac{1}{L} \\ 0 & -\frac{r+R}{L} & \frac{1}{L} & 0 \\ 0 & -\frac{1}{C} & 0 & 0 \\ -\frac{1}{C} & 0 & 0 & 0 \end{bmatrix} \tag{5.54}$$

$$B_2 = \begin{bmatrix} \frac{1}{L} & \frac{R}{L} & -\frac{R}{L} & 0 \\ 0 & \frac{R}{L} & 0 & -\frac{R}{L} \\ 0 & -\frac{1}{C} & \frac{1}{C} & 0 \\ 0 & -\frac{1}{C} & 0 & \frac{1}{C} \end{bmatrix} \tag{5.55}$$

The dynamic average equation can be obtained:

$$A = d_{ST}A_1 + (1 - d_{ST})A_2 \tag{5.56}$$

Substitute equation (5.52) and equation (5.54) into equation (5.56), we get

$$A = \begin{bmatrix} -\frac{r+R}{L} & 0 & \frac{d_{ST}-1}{L} & \frac{d_{ST}}{L} \\ 0 & -\frac{r+R}{L} & \frac{d_{ST}}{L} & -\frac{d_{ST}-1}{L} \\ \frac{1-d_{ST}}{C} & -\frac{d_{ST}}{C} & 0 & 0 \\ -\frac{d_{ST}}{C} & \frac{1-d_{ST}}{C} & 0 & 0 \end{bmatrix} \tag{5.57}$$

The dynamic average equation of B can be obtained using the following equation:

$$B = d_{ST}B_1 + (1 - d_{ST})B_2 \tag{5.58}$$

Substitute equation (5.53) and (5.55) into equation (5.58)

$$B = \begin{bmatrix} \frac{1}{L} & \frac{(1-d_{ST})R}{L} & \frac{R(d_{ST}-1)}{L} & \frac{d_{ST}R}{L} \\ 0 & \frac{(1-d_{ST})R}{L} & \frac{d_{ST}}{L} & \frac{(d_{ST}-1)R}{L} \\ 0 & \frac{d_{ST}-1}{C} & \frac{1-d_{ST}}{C} & \frac{d_{ST}}{C} \\ 0 & \frac{d_{ST}-1}{C} & \frac{d_{ST}}{C} & \frac{d_{ST}-1}{C} \end{bmatrix} \tag{5.59}$$

Therefore, the overall dynamic average equation of qZSI transfer function can be written as:

$$\frac{dx}{dt} = Ax + Bu$$

$$\begin{bmatrix} \frac{di_{L1}(t)}{dt} \\ \frac{di_{L2}(t)}{dt} \\ \frac{dv_{C1}(t)}{dt} \\ \frac{dv_{C2}(t)}{dt} \end{bmatrix} = \begin{bmatrix} -\frac{r+R}{L} & 0 & \frac{(d_{ST}-1)}{L} & \frac{d_{ST}}{L} \\ 0 & -\frac{r+R}{L} & \frac{d_{ST}}{L} & \frac{(d_{ST}-1)}{L} \\ \frac{(1-d_{ST})}{C} & -\frac{d_{ST}}{C} & 0 & 0 \\ -\frac{d_{ST}}{C} & \frac{(1-d_{ST})}{C} & 0 & 0 \end{bmatrix} \begin{bmatrix} i_{L1}(t) \\ i_{L2}(t) \\ v_{C1}(t) \\ v_{C2}(t) \end{bmatrix} + \begin{bmatrix} \frac{1}{L} & \frac{(1-d_{ST})R}{L} & \frac{R(d_{ST}-1)}{L} & \frac{d_{ST}R}{L} \\ 0 & \frac{(1-d_{ST})R}{L} & \frac{d_{ST}}{L} & \frac{(d_{ST}-1)R}{L} \\ 0 & \frac{d_{ST}-1}{C} & \frac{1-d_{ST}}{C} & \frac{d_{ST}}{C} \\ 0 & \frac{d_{ST}-1}{C} & \frac{d_{ST}}{C} & \frac{d_{ST}-1}{C} \end{bmatrix} \begin{bmatrix} v_{in}(t) \\ i_{DC}(t) \\ i_{B1}(t) \\ i_{B2}(t) \end{bmatrix} \tag{5.60}$$

In small-signal analysis of qZSI topology, the perturbations of the small-signal include $v_{in}, i_{DC}, d_{ST}, v_{C1}, v_{C2}, i_{L1}$ and i_{L2} as shown in equation (5.61) to (5.67).

$$v_{in} = V_{in} + \widehat{v_{in}} \tag{5.61}$$

$$i_{DC} = I_{DC} + \widehat{i_{DC}} \tag{5.62}$$

$$d_{ST} = D_{ST} + \widehat{d_{ST}} \tag{5.63}$$

$$v_{C1} = V_{C1} + \widehat{v_{C1}} \tag{5.64}$$

$$v_{C2} = V_{C2} + \widehat{v_{C2}} \tag{5.65}$$

$$i_{L1} = I_{L1} + \widehat{i_{L1}} \tag{5.66}$$

$$i_{L2} = I_{L2} + \widehat{\imath_{L2}} \tag{5.67}$$

Where $\widehat{v_{in}}$ represents the DC-input voltage perturbation, $\widehat{\imath_{DC}}$ represents the DC-link current perturbation, $\widehat{d_o}$represents the small-signal duty ratio perturbation, $\widehat{v_{C1}}$ and $\widehat{v_{C2}}$ represents the small-signal perturbation of capacitor voltage across C_1 and C_2 respectively, $\widehat{\imath_{L1}}$ and $\widehat{\imath_{L2}}$ represents the small-signal perturbation of capacitor current flowing through inductor L_1 and L_2 respectively. On the other hand, V_{in} represents the peak DC-input voltage, I_{DC} represents the peak DC-link current, D_o represents the peak duty ratio, V_{C1} and V_{C2} represents the peak capacitor voltage of C_1 and C_2 respectively, I_{L1} and I_{L2} represents the peak capacitor current flowing through of L_1 and L_2 respectively.

Substituting equation (5.61) til equation (5.67) into equation (5.60), the dynamic state average equation with small-signal perturbations can be written as:

$$\begin{bmatrix} \frac{d(I_{L1}(t)+\widehat{\imath_{L1}}(t))}{dt} \\ \frac{d(I_{L2}(t)+\widehat{\imath_{L2}}(t))}{dt} \\ \frac{d(V_{C1}(t)+\widehat{v_{C1}}(t))}{dt} \\ \frac{d(V_{C2}(t)+\widehat{v_{C2}}(t))}{dt} \end{bmatrix} = \begin{bmatrix} -\frac{r+R}{L} & 0 & \frac{(D_{ST}+\widehat{d_{ST}}-1)}{L} & \frac{D_{ST}+\widehat{d_{ST}}}{L} \\ 0 & -\frac{r+R}{L} & \frac{D_{ST}+\widehat{d_{ST}}}{L} & \frac{(D_{ST}+\widehat{d_{ST}}-1)}{L} \\ \frac{(1-D_{ST}-\widehat{d_{ST}})}{C} & -\frac{D_{ST}+\widehat{d_{ST}}}{C} & 0 & 0 \\ -\frac{D_{ST}+\widehat{d_{ST}}}{C} & \frac{(1-D_{ST}-\widehat{d_{ST}})}{C} & 0 & 0 \end{bmatrix} \begin{bmatrix} I_{L1}(t)+\widehat{\imath_{L1}}(t) \\ I_{L2}(t)+\widehat{\imath_{L2}}(t) \\ V_{C1}(t)+\widehat{v_{C1}}(t) \\ V_{C2}(t)+\widehat{v_{C2}}(t) \end{bmatrix} + \begin{bmatrix} \frac{1}{L} & \frac{R(1-D_{ST}-\widehat{d_{ST}})}{L} & \frac{R(D_{ST}+\widehat{d_{ST}}-1)}{L} & \frac{(D_{St}+\widehat{d_{ST}})R}{L} \\ 0 & \frac{R(1-D_{ST}-\widehat{d_{ST}})}{L} & \frac{(D_{ST}+\widehat{d_{ST}})R}{L} & \frac{(D_{ST}+\widehat{d_{ST}}-1)R}{L} \\ 0 & -\frac{1-D_{ST}-\widehat{d_{ST}}}{C} & \frac{1-D_{ST}-\widehat{d_{ST}}}{C} & \frac{D_{ST}+\widehat{d_{ST}}}{C} \\ 0 & -\frac{1-D_{ST}+\widehat{d_{ST}}}{C} & \frac{D_{ST}+\widehat{d_{ST}}}{C} & \frac{D_{ST}+\widehat{d_{ST}}-1}{C} \end{bmatrix} \begin{bmatrix} V_{in}(t)+\widehat{v_{in}}(t) \\ I_{DC}(t)+\widehat{\imath_{DC}}(t) \\ I_{B1}(t)+\widehat{\imath_{B1}}(t) \\ I_{B2}(t)+\widehat{\imath_{B2}}(t) \end{bmatrix} \tag{5.68}$$

By doing linearization and applied Laplace transform on equation (5.68), only taking the first order AC terms while eliminates others, the following equations (5.69) can be obtained. Also, assuming that, $\widehat{\imath_{L1}} = \widehat{\imath_{L2}}$ and $\widehat{v_{C1}} = \widehat{v_{C2}}$.

$$\begin{aligned} &[Ls + (r+R)]\widehat{I_L}(s) \\ &\quad = \widehat{d_{ST}}(s)(V_{C1} + V_{C2} - RI_{DC} + RI_{B1} + RI_{B2}) \\ &\quad + \widehat{v_{C1}}(s)(2D_{ST} - 1) + \widehat{I_{DC}}(s)(R - D_{ST}R) + \widehat{v_{in}}(s) \end{aligned} \tag{5.69}$$

$$Cs\widehat{v_{C1}}(s) = \widehat{\imath_L}(s)(1 - 2D_{ST}) + \widehat{d_{ST}}(s)(-I_{L1} - I_{L2} + I_{DC} - I_{B1} + I_{B2}) + \widehat{\imath_{DC}}(s)(D_{ST} - 1) + \widehat{\imath_{B1}}(s)(1 - D_{ST}) \quad (5.70)$$

By rearranging equation (5.70), we obtained the following simplified equation.

$$\widehat{\imath_L}(s) = \frac{Cs\widehat{v_{C1}}(s) + \widehat{d_{ST}}(s)(I_{L1} + I_{L2} - I_{DC} + I_{B1} - I_{B2}) + \widehat{\imath_{DC}}(1 - D_{ST}) + \widehat{\imath_{B1}}(s)(D_{ST} - 1)}{1 - 2D_{ST}} \quad (5.71)$$

Substitute equation (5.71) into equation (5.69), we obtained the capacitor to shoot-through duty ratio transfer function as per equation (5.72) below

$$G_{\widehat{v_c}\widehat{d_{ST}}} = \frac{[(I_o - I_{L1} - I_{L2} - I_{B1} + I_{B2})(Ls + (r + R)) + (V_{C1} + V_{C2} - RI_{DC} + RI_{B1} + RI_{B2})(1 - 2D_{ST})]}{[LCs^2 + C(R + r)s + (1 - 2D_{ST})^2]} \quad (5.72)$$

5.4 Modelling of MPPT and grid-tie qZS Cascaded Multilevel Inverter-based STATCOM system

Figure 5.9 shows the qZCHI based grid-tie PV power system in real-time. Each qZSI model is fed by an independent PV-panel. To abstract the maximum power, the MPPT algorithm is implemented to the PV-panel. The total AC output voltage of the inverter is a series summation of cascaded of n^{th} independent qZSI controlled by its individual DC-link voltage controller. Each of the individual PV power source consists of identical PV cells that internally connected in parallel and series. A complete qZCHI based PV systems consists of two different controller modules. The first module consists of the DC-link voltage control to accomplish DC-link voltage balance and hence providing a smooth and equal AC voltage to the grid. This module is responsible to stabilize and generate shoot-through duty ratio for the qZSI to increase or decrease the output voltage. Another module consists of the power quality control of the input and the output side of the PV-based qZSI which include the MPPT control of the PV-panel and the VAR compensation at the PCC. In this module, the controller outputs desired modulation index to the power inverters switches to achieve maximum power extraction from each of the PV-array and to ensure the power injection to the grid at unity power factor with low harmonic distortion. The following section includes the derivation and modelling of the whole PV-based grid-tie qZCHI based STATCOM system.

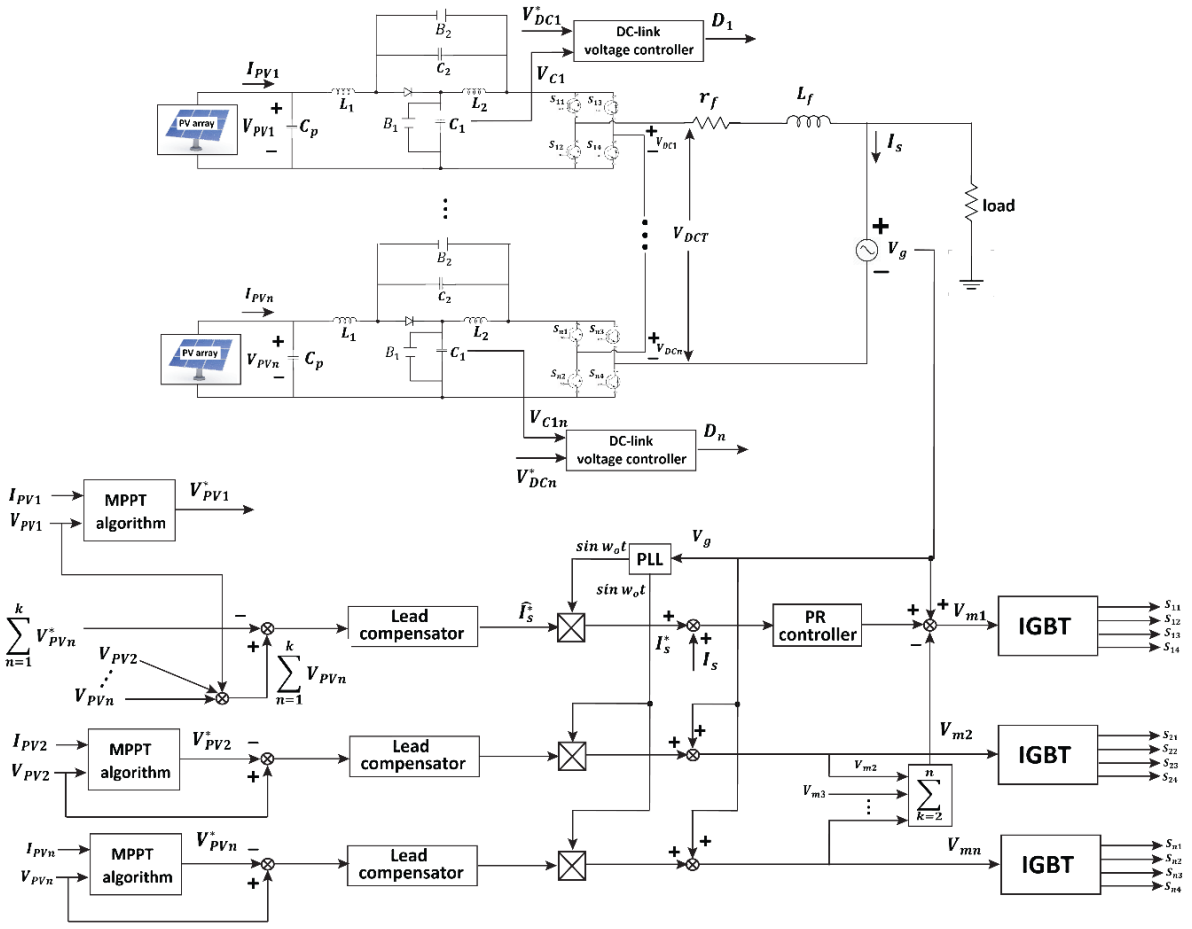

Figure 5.9: qZCHI based grid-tie PV power system

5.4.1 System modelling of grid-tie current loop

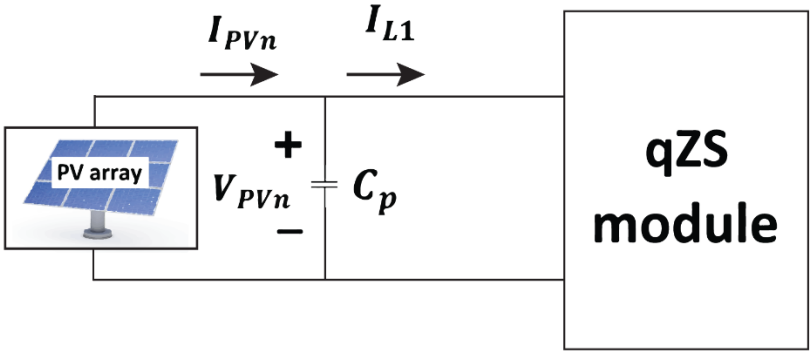

Figure 5.10: PV-based qZSI module

Figure 5.10 shows the PV-based qZSI module. Applying KCL to Figure 5.10, the n^{th} qZSI-HBI module has the following equation:

$$I_{PVn} - I_{CPn} = I_{L1n} \tag{5.73}$$

Where I_{PVn} is the n^{th} PV-array's current, I_{CPn} is the current that passes through the capacitor of the PV-array terminal capacitor that fence the PV-array to the qZS network. I_{L1n} is the first inductor's current of the qZS network. The n in each component symbol represents the n^{th} module of the qZSI.

$$I_{L1n} = I_{PVn} - C_p\left(\frac{dV_{PVn}}{dt}\right) \tag{5.74}$$

Where C_p is the capacitance of the PV-array terminal capacitor. Using KVL to define the equation at the AC output side of the qZSI, obtained the equation (5.75).

$$V_{DCT} = V_g + L_f\frac{dI_s}{dt} + r_f I_s \tag{5.75}$$

Where V_{DCT} is the summation of DC-link voltage of n^{th} modules. V_g is the grid voltage, I_s is the grid-injected current, L_f is the filter inductance and r_f is the parasitic resistance of the filter inductor. By performing laplace transform to equation (5.75), obtained the transfer function as per (5.76) below.

$$V_{DCT}(s) = V_g(s) + sL_f I_s(s) + r_f I_s(s) \tag{5.76}$$

Rearranging equation (5.76), obtained the following transfer function of the grid-injected current:

$$G_f(s) = \frac{I_s(s)}{V_{DCT}(s) - V_g(s)} = \frac{1}{L_f s + r_f} \tag{5.77}$$

A PR-controller is commonly used in grid-tie closed-loop control system to track the desired reference of a AC voltage/current [59]. The transfer function of the PR-controller can be defined as:

$$G_{PR}(s) = k_P + \frac{k_R w_o}{s^2 + w_o^2} \tag{5.78}$$

There is no work has been done to implement current reference algorithm (as shown in section 5.2 above) when the qZSI consists of both MPPT control and grid-tie current control (i.e., STATCOM). However, in [2], the author demonstrates the combination of MPPT control, grid-tie current control and DC-link voltage control to monopolize the DC-link voltage as well as power control implementation. According to [60], the implementation of ideal PR-controller is not practical due to the infinite quality factor. An approximated PR-controller is proposed in [60] and its transfer function is demonstrated in equation (5.79). The approximated PR-controller has broader bandwidth around the pre-set fundamental frequencies. In other words, the controller is less sensitive to the frequency outside of the preferred zone and hence providing a more robust system to frequency variations around these targeted frequencies.

$$G_{PR}(s) = k_p + \frac{2k_R w_c s}{s^2 + 2w_c s + w^2} \tag{5.79}$$

The n^{th} qZSI-CHB module has the modulation signal defined in equation (5.80).

$$V_{mn} = V'_{mn} + V_g(s) \left[\frac{V_{mn}(s)}{nV_{DCT}(s)}\right] \tag{5.80}$$

Where V_{mn} is the n^{th} module modulating signal, while V'_{mn} is the regulated modulating signal from separate voltage control of n^{th} module. Knowing that the modulating signal plays an important role in the generation of AC output voltage. The relationship between the modulating signal and the DC-link voltage is defined as per equation (5.81).

$$V_{DCn} = \frac{V_{DCT}(s)}{V_{mn}(s)} \tag{5.81}$$

Where V_{DCn} is the DC-link voltage in n^{th} module.

From equation (5.81),

$$V_{DCT}(s) = \sum_{n=1}^{k} V_{mn}(s) \cdot V_{DCn}$$

$$V_{DCT}(s) = \sum_{n=1}^{k} [V'_{mn}(s) \cdot V_{DCn} + \frac{V_g(s)}{n\,\widehat{v_{DCn}}} \cdot V_{DCn}] \tag{5.82}$$

Assume that the DC-link voltage for each module is kept being the same. Hence, by rearranging equation (5.82), obtained the following equation:

$$V_g(s) = (V_{mn} - V'_{mn}) n V_{DCn} \tag{5.83}$$

Substitute equation (5.83) into equation (5.77) and simplify it, transfer function in equation (5.84) can be obtained.

$$G_f(s) = \frac{I_s(s)}{\sum_{n=1}^{k} V'_{mn}(s) \cdot V_{DCn}}$$

$$I_s(s) = G_f(s) V_{DCn} \sum_{n=1}^{k} V'_{mn}(s) \tag{5.84}$$

5.4.2 System modelling of PV voltage loop

Rearranging equation (5.74) and apply Laplace transform, obtained the following transfer function:

$$V_{PVn}(s) = \frac{1}{C_p s}\left(I_{PVn}(s) - I_{L1n}(s)\right) \tag{5.85}$$

Assuming a 100% efficiency system, the output power of the entire system will be equal to its input power. In equation (5.86), P_{grid} represents the grid power, P_{out} represents the DC-link output power, and P_{in} represents the input power generated by the PV-array.

$$P_{grid} = P_{out} = P_{in}$$
$$\frac{I_s V_{DCn}}{2} = V_{DCn} I_{DCn} = V_{PVn} I_{L1n_{nst}} \tag{5.86}$$

Where $I_{L1n_{nst}}$ represents the current that passes through the first inductor in nth qZS network during the non-shoot-through state.

Using equation (3.21) and replace V_{in} in equation (3.21) with V_{PVn} in this case, the inductor current in non-shoot-through state has the following transfer function.

$$I_{L1_{nst}} = \frac{I_s V_{DCn}}{2V_{DCn}(1 - 2D_n)} \tag{5.87}$$

During shoot-through state, the inductor current can be written as:

$$I_{L1n_{st}} = I_{PVn} \tag{5.88}$$

Using the same analogy of inductor current described in chapter 3 and chapter 4, the average inductor current (i.e., I_{L1n}) in one switching cycle can be defined as:

$$I_{L1n} = D_n I_{L1n_{st}} + (1 - D_n) I_{L1n_{nst}}$$
$$I_{L1n} = D_n I_{PVn} + \frac{I_s (1 - D_n) V_{DCn}}{2V_{DCn}(1 - 2D_n)} \tag{5.89}$$

Figure 5.11 shows a bode plot example of the grid-tie current loop before and after the AC current compensation by PR-controller. The following bode plot is designed based on the parameters in section 4.2.1. The orange line represents the frequency response of the system before compensation, while the blue line represents the frequency response of

the system after compensation. The PR-controller parameters are designed to get a fast dynamic and provide zero steady-state error at the fundamental frequency. The symbol ω_n represents the corner frequency of the closed-loop transfer function of the grid-tie current loop; ω_F represents the fundamental frequency of the grid voltage/current (i.e., 50 Hz or 314 rad/s). The corner frequency, ω_n can be calculated using the following equation:

$$\omega_n = \frac{r_f}{L_f} \tag{5.90}$$

ω_F also called the resonant frequency of the PR-controller. Noticed that when the difference between the actual grid-current and its reference is compensated by using PR-controller, it provides a large gain inside its bandpass region (i.e., in the range between ω_n and ω_F, making the crossover frequency tenfold the corner frequency [2]. Therefore, the dynamic response of the grid-current/voltage can be enhanced without the detriment of system stability. The complete design and simulation for section 5.3 and section 5.4 will be performed in future work.

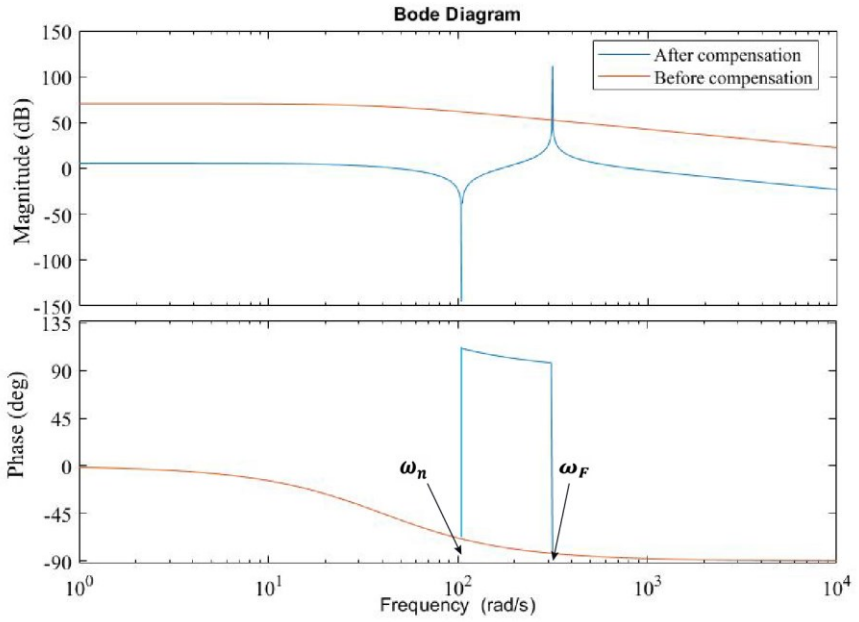

Figure 5.11: Bode plot for grid-current closed-loop control

Figure 5.12 represents the PV-based qZCHI STATCOM system control scheme block diagram. Notice in Figure 5.12, the control system consists of total voltage loop and separate voltage loop. The total voltage loop is used to track the summation of n^{th} PV-array voltages by comparing its value with the total output voltage reference from MPPT algorithm. The difference in reference voltage will then be compensated by a controller (i.e., lead compensator) and the generated reference value will be fed into the grid-tie current loop as discussed in section 5.4.1. With the combination of total PV loop and grid-tie current loop, the modulation output signal can be generated. This control loop combination is required to generate the first qZSI module's modulation signal. Other than that, this control loop is also employed in a single-stage grid-tie qZSI based STATCOM system. On the other hand, each of the qZSI module (other than the first module) has its own individual PV-array voltage loop to achieve MPPT. The $(n-1)^{th}$ separate PV voltage loops regulate the $(n-1)^{th}$ PV-array voltages using their respective controller in each of the module by generating each qZSI-CHB module modulation signal. This can reduce the n^{th} regulator's burden, achieve a fast dynamic response and minimize the grid voltage's impact on the grid-tie current [61].

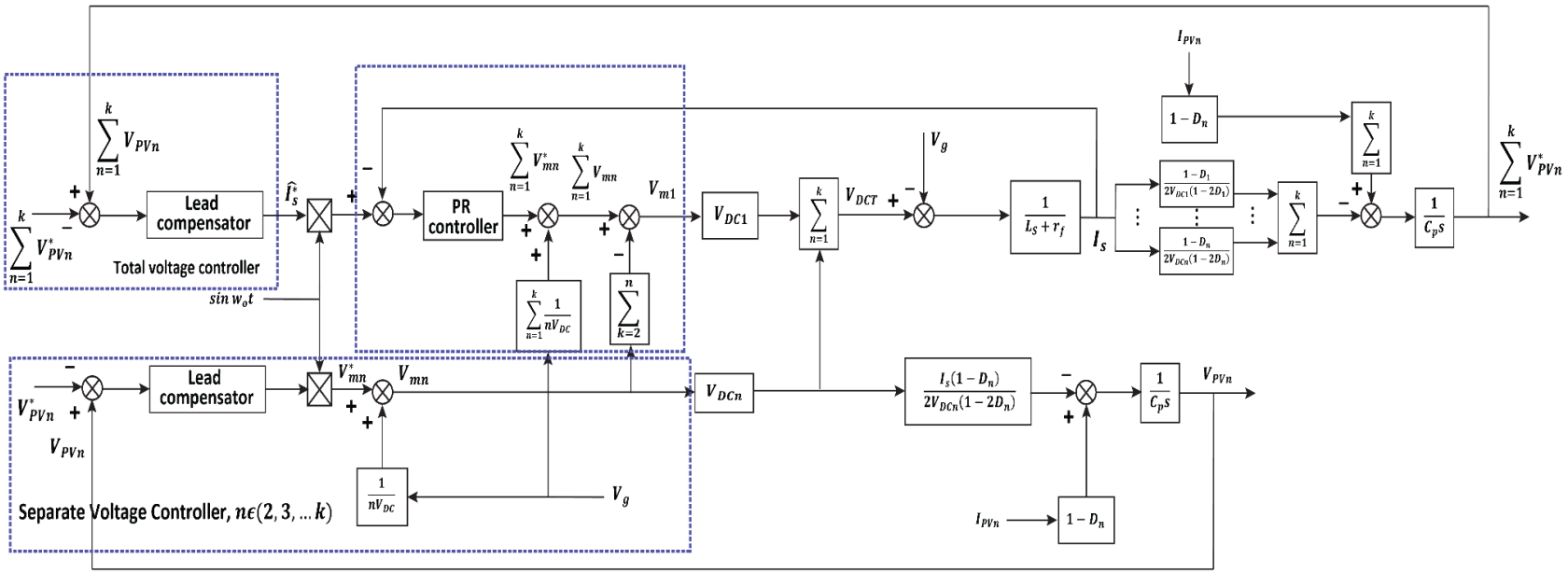

Figure 5.12: Block diagram of PV-based qZCHI STATCOM system control scheme

5.5 Simulation results

This section discusses the MATLAB/SIMULINK results for MPPT control and qZSI based STATCOM system under different loading conditions.

5.5.1 MPPT based duty cycle control of qZSI

In this simulation model, a PV-panel with model SunPower SPR-305-WHT was used. The combination of 1 series and 2 parallel PV modules was selected in this model. Table 5.1 shows the PV cell's parameters used in this simulation model. In this section, P&O algorithm was applied to the qZSI module for MPPT control. The voltage-ampere and voltage-power characteristic of SunPower SPR-305-WHT module for a specific given condition are shown in Figure 5.13. The model is simulated for various conditions and the obtained results are presented and discussed in this section. The following simulation model can be found in Figure A-6 in Appendix D. On the other hand, the P&O algorithm was coded in MATLAB C programming script to be simulated in SIMULINK block diagram. The code is presented in Appendix E.

Table 5.1: PV module parameters

Module type	SunPower SPR-305-WHT
Number of series-connected modules per string	1
Number of parallel strings	2
PV Open circuit voltage, V_{oc}	$64.2V$
PV Short circuit current, I_{sc}	$5.96A$
Voltage at MPP, V_{mp}	$54.7V$
Current at MPP I_{mp}	$5.58A$

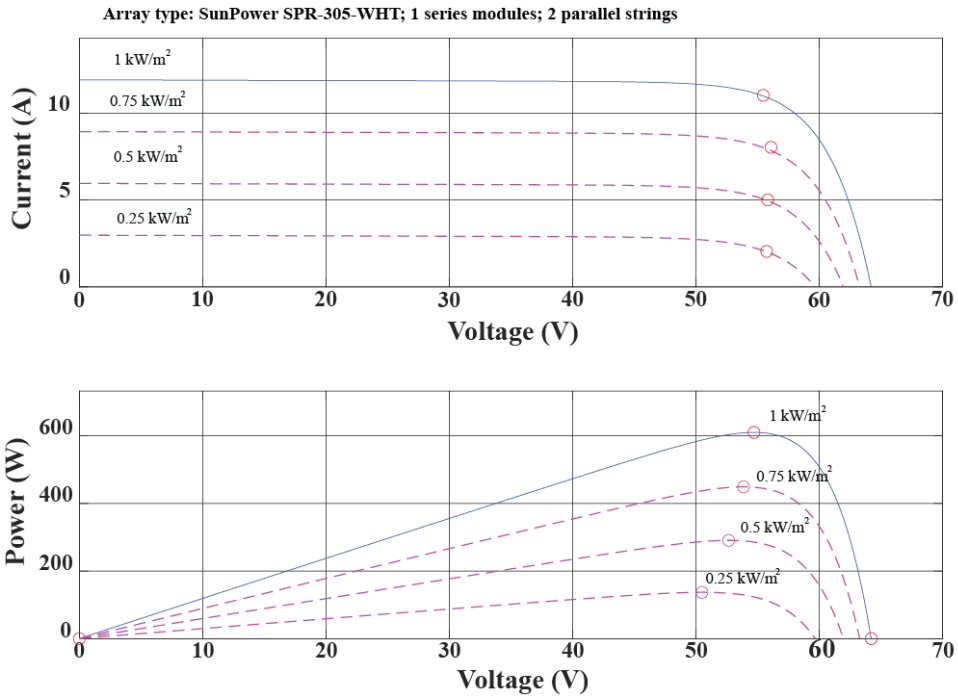

Figure 5.13: String array waveform at MPP (Current-voltage relationship and power-voltage relationship)

In this simulation model, the temperature on the PV module was kept constant while changing the solar irradiance projected to the PV module. Simulation was executed in the case that the output load was kept constant (i.e., $R_{load} = 50\Omega$) with varies PV circumstances (i.e., PV-panels are shaded by clouds etc.). Figure 5.14 shows the changes in the solar irradiance during the entire interval of 3s. The solar irradiance remained at $1\ kw/m^2$ within the interval of $0s$ to $0.7s$. The solar irradiance dropped and reach $0.5\ kw/m^2$ at $1.2s$. The solar irradiance slowly went up and reach $1\ kw/m^2$ again at $2s$ time interval. To shows the effectiveness of the designed controller, the solar irradiance dropped instantaneously to $0.25\ kw/m^2$ at time interval of $2.3s$. Lastly, the solar irradiance raised back up instantaneously at $2.7s$ to $1\ kw/m^2$. The initial duty ratio of qZSI is set to be at a fixed value (i.e., 0.4). The controller starting time is set to be at $0.05s$ for the qZSI system to stabilize itself before the controller has taken control over the output voltage.

According to Figure 5.13, the MPP is measured to be approximately $600W$ when the solar irradiation reaches $1kw/m^2$. At MPP, the voltage and current are expected to be $54.7V$ and $10.96A$ respectively. At solar irradiation of $0.5kw/m^2$, the MPP located at around $250W$ with $54.7V$ and $7.7A$. The solar panel has a MPP located at $170W$ (voltage and current are $54.7V$ and $5.5A$ respectively) when the solar irradiation is set to be $0.25\ kw/m^2$.

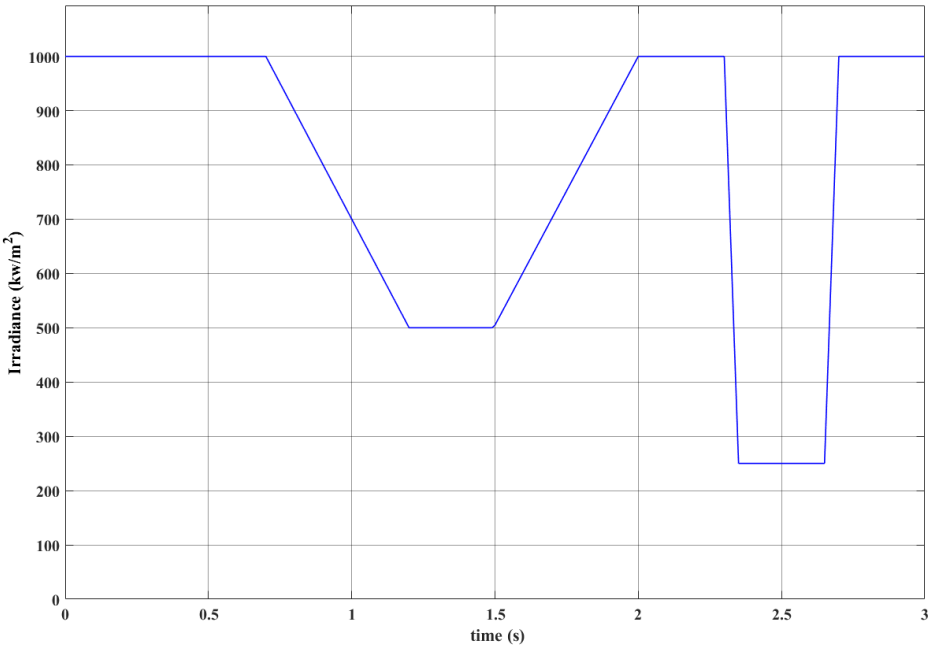

Figure 5.14: Changes in Solar Irradiance

Figure 5.15 and Figure 5.16 shows the duty cycle waveform and the DC-link output voltage waveform respectively. Notice that in this simulation model, the duty ratio did not change the DC-link voltage output. The reason is because the input voltage and current are varying during the time interval as the solar irradiation changes. The controller can maintain the DC-link voltage at stable and constant value even though the solar irradiance changes. Noticed how the duty ratio reacts to the changes in solar irradiance; duty ratio changes proportionally with the changes in solar irradiance. The instantaneous changes in the solar irradiance at $2.3s$ and $2.7s$ caused an overshoot in DC-link voltage. However, the overshoot voltage was somehow within an acceptable range. Nevertheless,

in real-life, the solar irradiation should not be changes in such pace, so we can conclude that the result is acceptable.

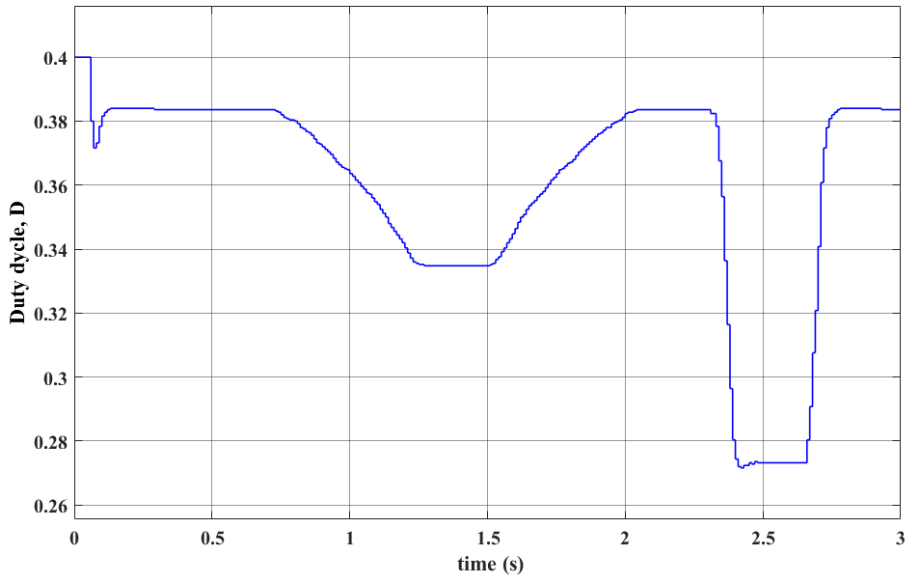

Figure 5.15: Duty cycle waveform

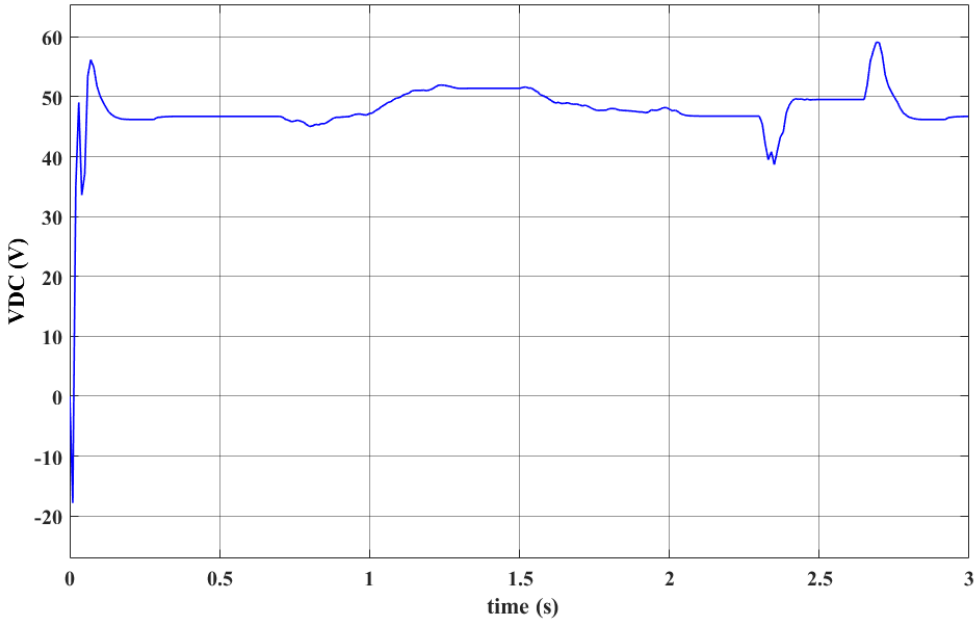

Figure 5.16: DC-link voltage waveform

As depicted from the name of MPPT algorithm, the most crucial parameters to be confined is the input PV power. In other words, the final goal for MPPT algorithm to achieve is to make sure the generated input power is corresponding to the MPP shown in Figure 5.13. Figure 5.17 describes the input power waveform of the qZSI with changes in solar irradiance. Unravel from the fact that Figure 5.13 only shows the theoretical value of MPP for the ideal cases. In Figure 5.17, notice that there is slight discrepancy in the PV generated power when MPPT algorithm was applied to the qZSI with solar irradiance variation. Despite, the MPPT has performed its job well to maintain the input power to be closed to the desired MPP.

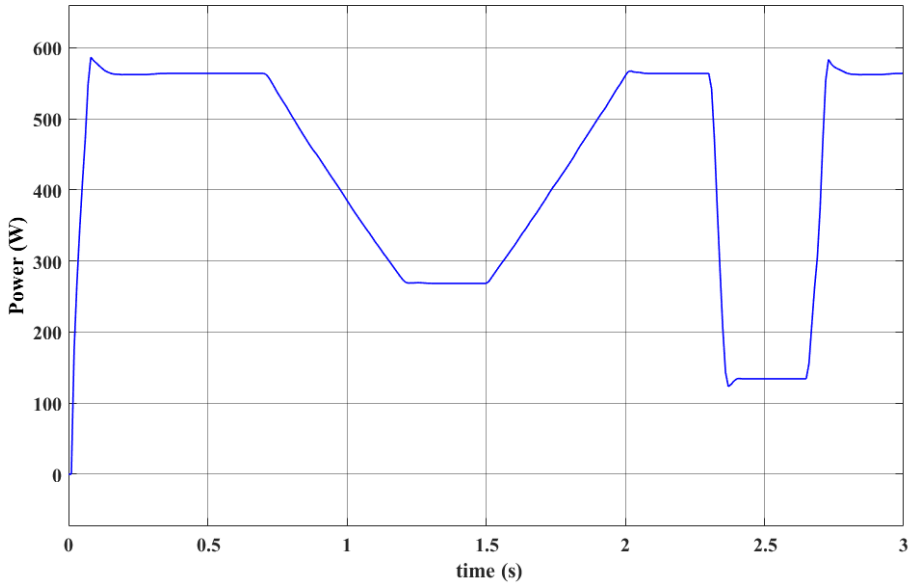

Figure 5.17: Input power waveform

5.5.2 STATCOM control system

In this section, the STATCOM system is incorporated with the SIMULINK model used in section 4.2. The complete simulation model can be found in Figure A-5 in Appendix D. The proposed lead compensator is applied to obtain DC-link voltage balance by controlling the shoot-through duty ratio. On the other hand, the modulation index that has been set as a constant (i.e., 0.5) in section 4.2 is now replaced with an adjustable value; the modulation index is now controlled by the STATCOM system. From the control scheme shown in Figure 5.2, AC output current from the qZSI is measured and fed into the abc-to-dq transformation block diagram. Meanwhile, the AC voltage at PCC is fed into phase-lock loop (PLL) and i_{oq}^{*} algorithm to calculate the desired phase angle and i_{oq}^{*} reference respectively. Table 5.2 below shows the network parameters of the foregoing SIMULINK model. Notice in the following simulation, the output AC voltage is scaled down by ten-fold for better views when comparing the phase difference between voltage and current.

Table 5.2: System parameters for qZSI STATCOM system

System parameters	Value
Input voltage, V_{in}	$12V$
Desired DC-link output voltage, V_{DC}	$60V$
Capacitor C_1 and C_2 value	$1000\mu F$
Inductance L_1 and L_2 value	$100\mu H$
Switching frequency, f_s	$10kHz$
Shoot-through duty ratio, D_{st}	0.4
System AC output frequency, f_{AC}	$50Hz$
Coupling inductance, L_f	$54mH$
Coupling parasitic resistance, R_f	17Ω
d-axis current gain	0.20813
q-axis current gain	1.633505

Figure 5.18(a) shows the combination of grid voltage (i.e., V_s) and grid-current (i.e., I_s) waveforms before reactive power compensation. Table 5.2 shows all the system parameters used in the simulation model. The simulation was conducted using two different loading conditions where the load is being changed at the time interval of 2s. The design of the STATCOM controller is explained and shown in section 5.2. The fully development of the control system can be viewed in [55]. Figure 5.18(b) shows the zoomed-in version of the grid voltage and grid-current waveform to provide a better view on the phase difference between these two waveforms (i.e., the power factor). Clearly by inspection of Figure 5.18(b), the grid-current is lagging of the grid voltage.

Figure 5.19 shows the grid voltage-current waveform after reactive power compensation. The zoomed-in version shown in Figure 5.19(b) has proven that the controller has performed the compensation pleasantly; reducing the time-shift between grid voltage and grid-current (i.e., power factor improvement from 0.62 to 0.99); the power factor is corrected significantly. Based on the graph, we can conclude that the power factor for the inductive load can be compensated to nearly unity after compensation.

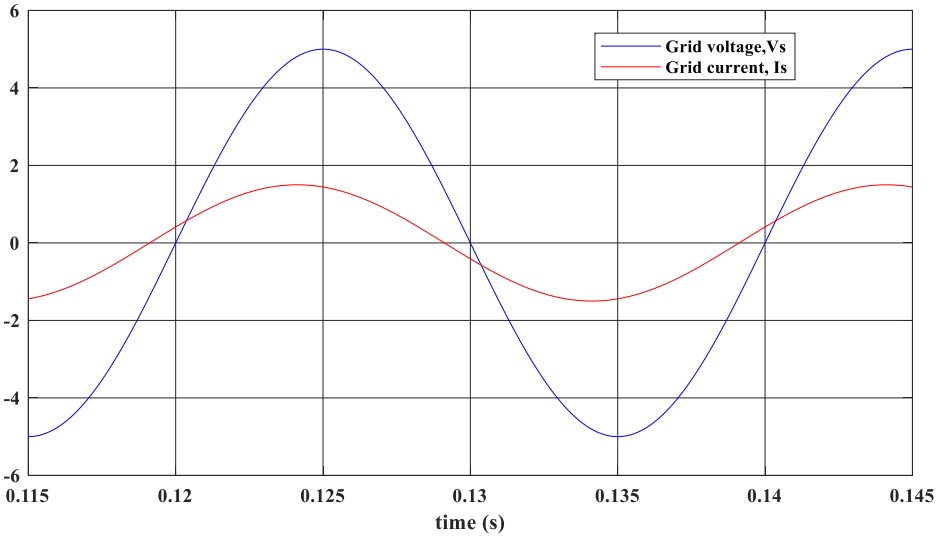

(a)

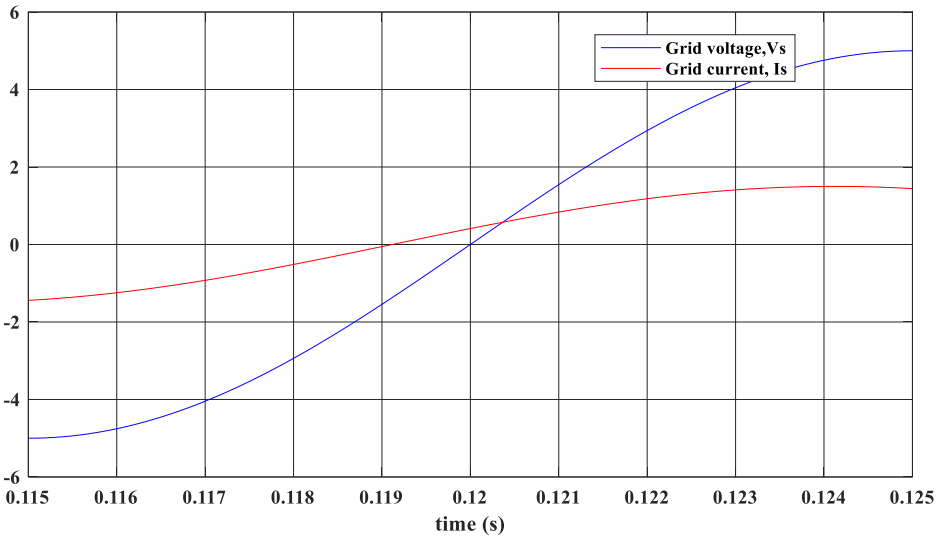

(b)

Figure 5.18: (a) Grid voltage and current waveform before reactive power compensation (b) Zoomed-in version of grid voltage and current waveform before reactive power compensation

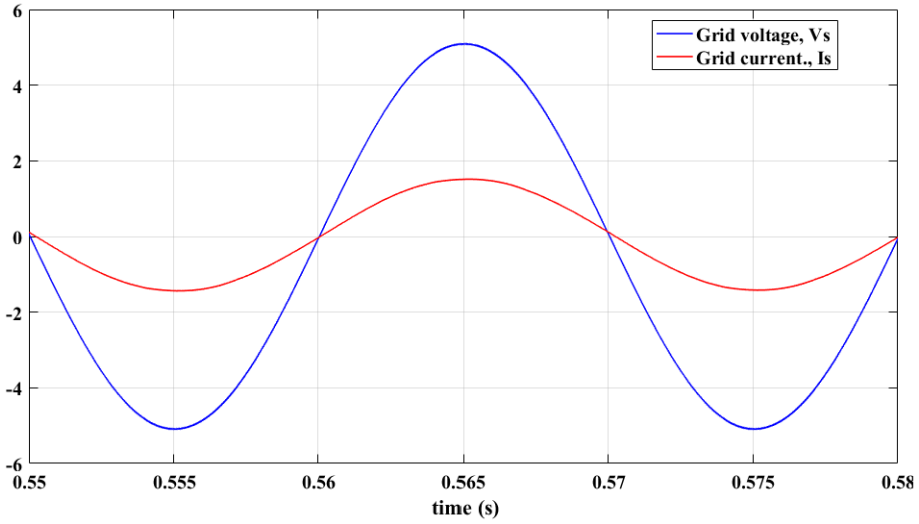

(a)

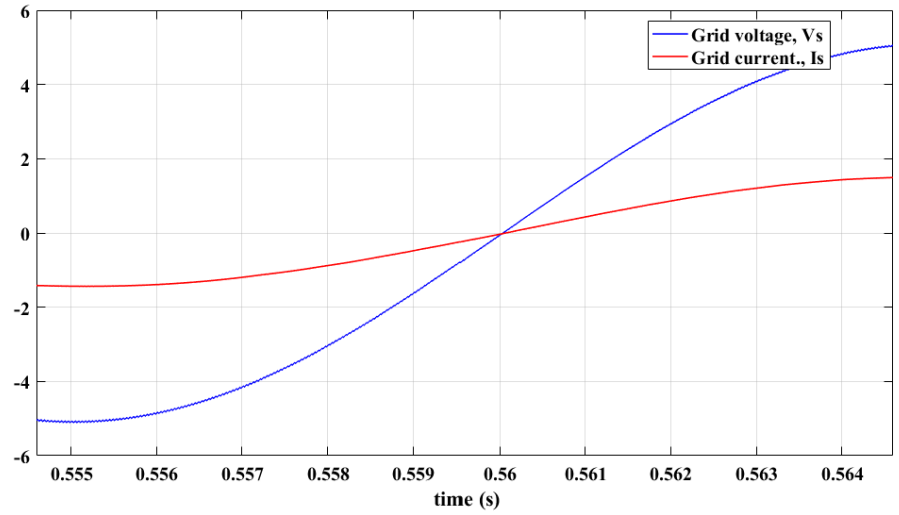

(b)

Figure 5.19: (a) Grid voltage and current waveform after reactive power compensation (b) Zoomed-in version of grid voltage and current waveform after reactive power compensation

Figure 5.20 demonstrates the dynamic and transient performance of the proposed STATCOM control scheme. The controller can maintain the output voltage at a constant value when different loading condition is applied. At the time interval of $2s$, the grid-current shows a minor overshoot and it reaches steady-state within a very short interval, confirms that the qZSI based STATCOM system can properly generate reactive power to compensate for different loading conditions.

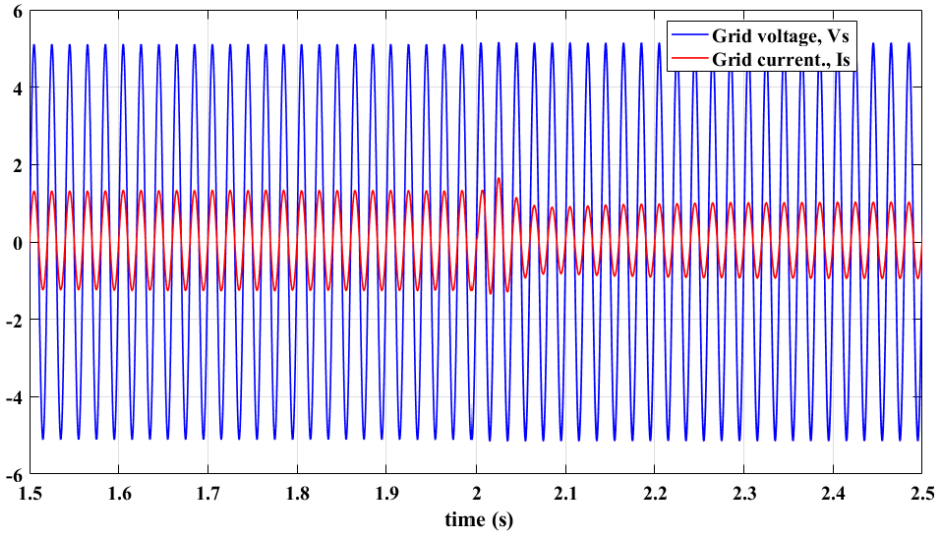

Figure 5.20: Grid voltage and current waveform when varied loading condition was applied

Figure 5.21 shows AC-output voltage and DC-link output voltage without the AC filter. The controller can achieve stable DC-link voltage and maintain it at 60V within a very short period, which has verify the analysis made earlier in chapter 4 (i.e., the feasibility of lead compensator). Figure 5.22 indicates the modulation signal generated by the STATCOM system to compensate with the reactive power generated. Notice that the STATCOM system is only activated after the first 200 ms. Therefore, the initial modulation signal is set to be 0.5. This is to make sure that the DC-link controller is able to achieve optimal DC-link voltage compensation before the STATCOM system takes control over the modulation signal.

Lastly, Figure 5.23 shows the i_{lq} and i_{cq} current within the STATCOM system. The I_{lq} is generated to compensate with the I_{cq} (i.e., due to capacitive load). Figure 5.23 shows the current generated is opposed to each other. In other words, if capacitive reactive current is present in the load, the STATCOM system will generate I_{lq} to cancel out the negative reactive source current, and vice versa.

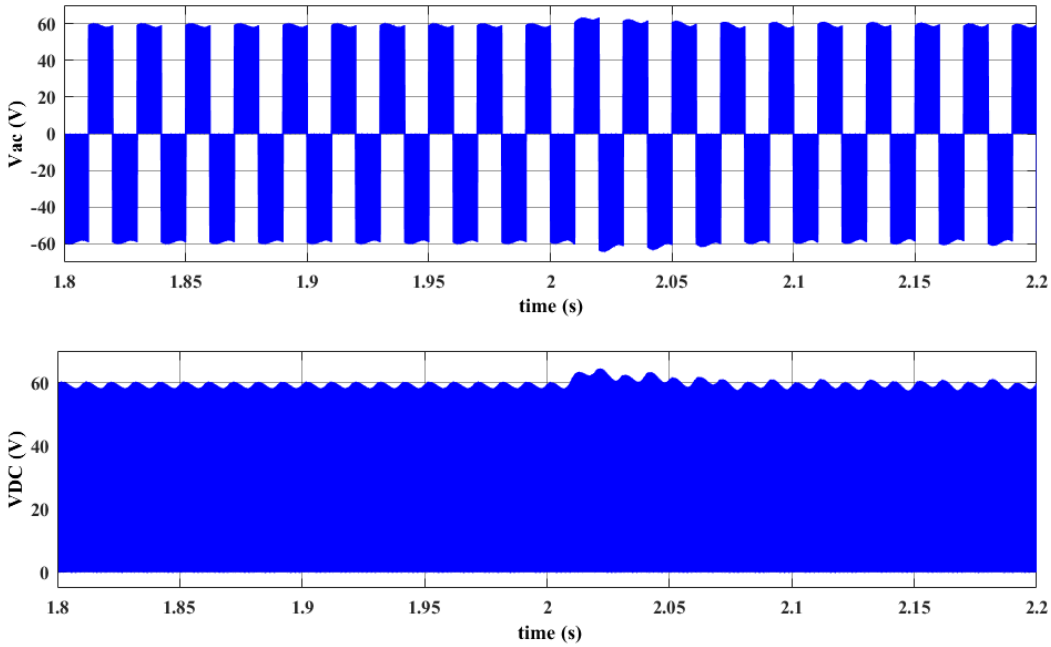

Figure 5.21: (a)AC output voltage (b) DC-link output voltage

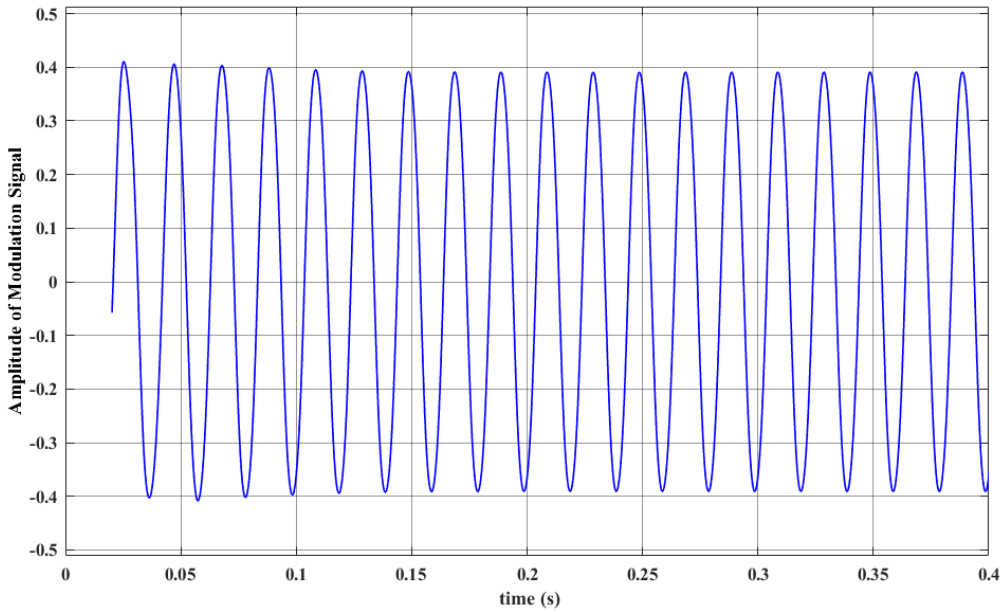

Figure 5.22: Modulation signal

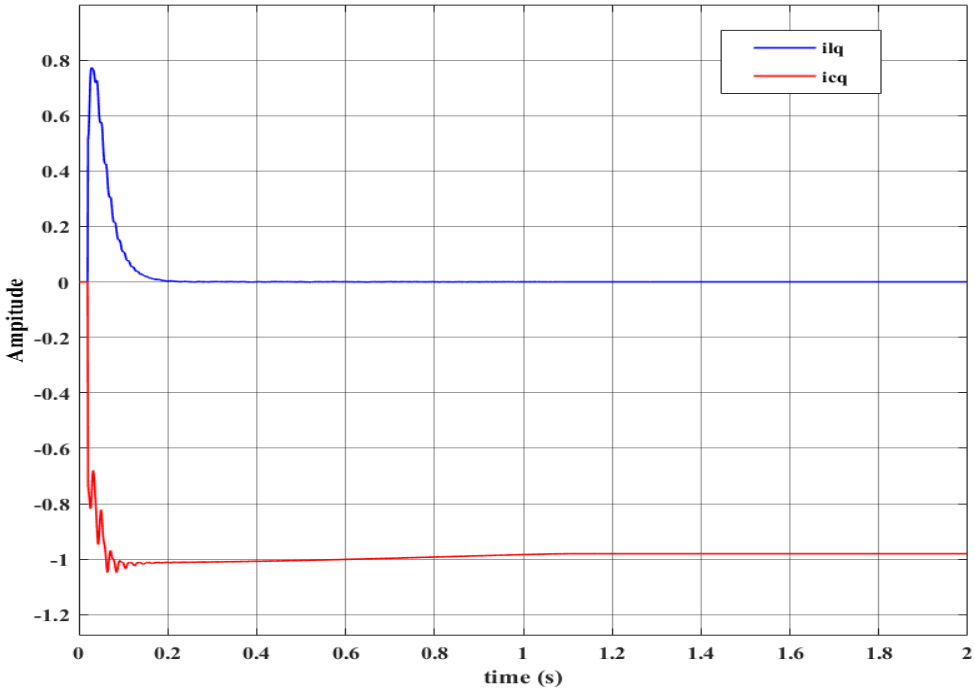

Figure 5.23: Icq & Ilq waveform

5.6 Summary

This chapter is mainly focus on the power quality improvement of qZSI. The first part of results illustrates that the MPPT algorithm has been successfully integrated to qZSI when PV power system is included. The simulation results show that the controller can achieve MPP with small variations from the theoretical value. The second part of the results shows the integration of STATCOM system for reactive power compensation. The STATCOM system ensures that the power factor of the system to reach unity. With the combination of lead compensator, the controllers can maintain the output voltage at constant value. On the other hand, the modelling of two energy storing battery-based qZSI has been conducted and shown in section 5.3. This includes the derivation of large and small-signal transfer function of the proposed topology. Lastly, section 5.4 demonstrates the modelling of MPPT and grid-tie qZS Cascaded Multilevel Inverter-based STATCOM system with the derivation of grid-tie transfer function as well as the transfer function of total and separate PV voltage loop.

Chapter 6: Conclusion and Future Work

6.1 Conclusion Remarks

To conclude, this research project has been carried out successfully through simulation work performed in software MATLAB/SIMULINK. The simulation models consist of three different parts. The first part comprises of the operating mode of qZSI which can be characterized into three categories; CCM, BCM and DCM. Second part of the research project consists of the design of DC-link voltage controller and followed by cascading two qZSI module to generate multilevel output voltage. The third part of the research project covers the power improvement strategy in qZSI.

The first part of research project presents a detailed analysis of CCM, BCM and DCM analysis in qZSI. The mathematical equations to distinguish between these operating modes have been derived. The simulation results have shown that the derived equations were accurate. The derived equations also illustrate and allows researchers to prevent qZSI to operate in DCM, by adjusting several parameters and form different combination when designing qZSI. Thereupon, the obtained simulation results have fulfilled and achieved the first objective of this research project.

In this research work, lead compensator is selected to replace the commonly used controller in qZSI control system (i.e., PI controller) in the voltage loop of the qZSI control system. An equation that compute DC-link voltage to inductor current is missing in conventional qZSI voltage control loop. To compensate with this issue, the mentioned equation is derived and included when lead compensator is used. However, this does not mean that the control system designed by previous researcher is incorrect. By inspecting equation (4.88), we have noticed that the transfer function consists of an integral term multiply with a constant (i.e., gain), which is congruent with the integral term used in a PI controller. Although lead compensator seems to be more complex than PI control, but the design procedure of lead compensator is somewhat simple and easy to be implement. Overall, the performance in lead compensator is rather similar to PI controller when apply in qZSI. The major difference in the performance happens in the DC-link voltage comparison of both methods. From the simulation results, PI controller offers higher

percentage overshoot during the start-up process and requires longer settling time to achieve steady-state in real-time simulation. Nevertheless, controller's performance can be altered when different system parameters are employed. To prevent an unfair judgement, further analysis must be performed in future work. However, based on the selected parameters in this research project, lead compensator shows major dominance over PI controller.

The last chapter of the research project is to enhance the input and output power quality of the qZSI when PV power system is included. Output side of the qZSI refers to the distribution of grid voltage and current. The solar irradiance and temperature change rapidly throughout the day, which causes similar fluctuation in input PV power as well. To comprehend this issue, MPPT algorithm is applied. Further regulation of input power can be done by adding energy storing battery to the qZS module; connected the battery to the qZS capacitor. The modelling of the two energy storing battery-based qZSI has been included with the derivation of novel transfer functions which illustrate the foregoing model. Later, the five-level qZCHI was adopted to be used in STATCOM application with different loading condition. With a simulated reactive load, the qZCHI STATCOM system successfully compensated the reactive power and allow the power factor to attain at unity.

6.2 Future works

With successful simulation execution of this research project, hardware implementation can be performed in the future to further verify the practicality of the derived mathematical equations. Based on literature reviews, most of the researchers only analyse the performance of controller when qZSI operates in CCM. Thus, experiment can be conducted to identify the performance of lead compensator and PI controller in qZSI when the system is operating in DCM as well. Different combination of system parameters should be tested to examine the accuracy of the derived equations.

Section 5.2 discusses the implementation of I_{oq}^{*} algorithm in STATCOM control system. Yet in section 5.4, the STATCOM approach is totally different from that in section 5.2. In [2], the author applied proportional resonant controller in the STATCOM feedback loop to ensure that the voltage and current are in phase; Section 5.4 has similar approaches. As mentioned earlier, no research has been done to implement I_{oq}^{*} algorithm based STATCOM control system to qZSI when PV power system is included. Therefore, it could be another novel research by integrating I_{oq}^{*} algorithm based STATCOM with PV power system to output a modulation index to the inverter IGBTs.

Other than that, simulation and experimental implementation can be performed for the two energy storing battery-based qZSI as the modelling of the proposed topology has been done in section 5.3. The derived transfer function will be verified followed by the design of DC-link controller-based on the proposed topology. Once the DC-link voltage controller has reach the expected performance, PV power system and STATCOM system can be merged into the module. Next, MPPT control will be implemented to regulate the PV power when the energy storing battery has run out of power. Finally, the proposed topology will be implemented in real-life experiment setup.

Reference:

[1] D. Cao, S. Jiang, X. Yu, and F. Z. Peng, "Low-Cost Semi-Z-source Inverter for Single-Phase Photovoltaic Systems," *IEEE Transactions on Power Electronics,* vol. 26, pp. 3514-3523, 2011.

[2] Y. Liu, B. Ge, H. Abu-Rub, and F. Z. Peng, "An Effective Control Method for Quasi-Z-Source Cascade Multilevel Inverter-Based Grid-Tie Single-Phase Photovoltaic Power System," *IEEE Transactions on Industrial Informatics,* vol. 10, pp. 399-407, 2014.

[3] D. Sun, B. Ge, W. Liang, H. Abu-Rub, and F. Z. Peng, "An Energy Stored Quasi-Z-Source Cascade Multilevel Inverter-Based Photovoltaic Power Generation System," *IEEE Transactions on Industrial Electronics,* vol. 62, pp. 5458-5467, 2015.

[4] Y. Zhou, L. Liu, and H. Li, "A High-Performance Photovoltaic Module-Integrated Converter (MIC) Based on Cascaded Quasi-Z-Source Inverters (qZSI) Using eGaN FETs," *IEEE Transactions on Power Electronics,* vol. 28, pp. 2727-2738, 2013.

[5] M. Mosa, R. S. Balog, and H. Abu-Rub, "High-Performance Predictive Control of Quasi-Impedance Source Inverter," *IEEE Transactions on Power Electronics,* vol. 32, pp. 3251-3262, 2017.

[6] B. Ge, F. Z. Peng, H. Abu-Rub, F. J. T. E. Ferreira, and A. T. d. Almeida, "Novel Energy Stored Single-Stage Photovoltaic Power System With Constant DC-Link Peak Voltage," *IEEE Transactions on Sustainable Energy,* vol. 5, pp. 28-36, 2014.

[7] P. K. Jin, M. S. A. Dahidah, and C. Klumpner, "Nine-level SHE-PWM VSC based STATCOM for VAR compensation," in *2010 IEEE International Conference on Power and Energy*, 2010, pp. 135-140.

[8] Y. Liu, B. Ge, H. Abu-Rub, and F. Z. Peng, "Phase-shifted pulse-width-amplitude modulation for quasi-Z-source cascade multilevel inverter-based photovoltaic power system," *IET Power Electronics,* vol. 7, pp. 1444-1456, 2014.

[9] Y. Zhou, H. Li, and H. Li, "A Single-Phase PV Quasi-Z-Source Inverter With Reduced Capacitance Using Modified Modulation and Double-Frequency Ripple Suppression Control," *IEEE Transactions on Power Electronics,* vol. 31, pp. 2166-2173, 2016.

[10] J. J. Shea, "Understanding FACTS-concepts and technology of flexible AC transmission systems [Book Review]," *IEEE Electrical Insulation Magazine,* vol. 18, pp. 46-46, 2002.

[11] K. R. Padiyar. (2007). *FACTS controllers in power transmission and distribution*.

[12] B. Ronner, P. Maibach, and T. Thurnherr, "Operational experiences of STATCOMs for wind parks," *IET Renewable Power Generation,* vol. 3, pp. 349-357, 2009.

[13] B. Nayak, S. Kumar, and S. S. Dash, "Design of phase lead compensator for buck converter fed adjustable speed drive," in *2015 Communication, Control and Intelligent Systems (CCIS)*, 2015, pp. 304-308.

[14] Y. Chen, "Replacing a PID controller by a lat-lead compensator for a robot-a frequency-response approach," *IEEE Transactions on Robotics and Automation,* vol. 5, pp. 174-182, 1989.

[15] *5 Reasons that Electric Vehicles are better than Gasoline Vehicles*. Available: https://webberenergyblog.wordpress.com/2012/04/12/5-reasons-that-electric-vehicles-are-better-than-gasoline-vehicles/

[16] M. Shen, A. Joseph, J. Wang, F. Z. Peng, and D. J. Adams, "Comparison of Traditional Inverters and Z -Source Inverter for Fuel Cell Vehicles," *IEEE Transactions on Power Electronics,* vol. 22, pp. 1453-1463, 2007.

[17] A. Battiston, J. P. Martin, E. H. Miliani, B. Nahid-Mobarakeh, S. Pierfederici, and F. Meibody-Tabar, "Comparison Criteria for Electric Traction System Using Z-Source/Quasi Z-Source Inverter and Conventional Architectures," *IEEE Journal of Emerging and Selected Topics in Power Electronics,* vol. 2, pp. 467-476, 2014.

[18] P. Fang Zheng, "Z-source inverter," *IEEE Transactions on Industry Applications,* vol. 39, pp. 504-510, 2003.

[19] Y. Li, J. Anderson, F. Z. Peng, and D. Liu, "Quasi-Z-Source Inverter for Photovoltaic Power Generation Systems," in *2009 Twenty-Fourth Annual IEEE Applied Power Electronics Conference and Exposition*, 2009, pp. 918-924.

[20] J. Zakis, D. Vinnikov, and I. Roasto, "Soft-switching capability analysis of a qZSI-based DC/DC converter," in *2010 12th Biennial Baltic Electronics Conference*, 2010, pp. 301-304.

[21] J. Anderson and F. Z. Peng, "Four quasi-Z-Source inverters," in *2008 IEEE Power Electronics Specialists Conference*, 2008, pp. 2743-2749.

[22] T. W. Chun, H. H. Lee, H. G. Kim, and E. C. Nho, "Power control for a PV generation system using a single-phase grid-connected quasi Z-source inverter," in *8th International Conference on Power Electronics - ECCE Asia*, 2011, pp. 889-893.

[23] H. Abu-Rub, A. Iqbal, S. M. Ahmed, F. Z. Peng, Y. Li, and G. Baoming, "Quasi-Z-Source Inverter-Based Photovoltaic Generation System With Maximum Power Tracking Control Using ANFIS," *IEEE Transactions on Sustainable Energy,* vol. 4, pp. 11-20, 2013.

[24] A. Keshavarzian and H. Iman-Eini, "A Redundancy-based scheme for balancing DC-link voltages in cascaded H-bridge rectifiers," *IET Power Electronics,* vol. 6, pp. 235-243, 2013.

[25] M. Aleenejad, H. Iman-Eini, and S. Farhangi, "Modified space vector modulation for fault-tolerant operation of multilevel cascaded H-bridge inverters," *IET Power Electronics,* vol. 6, pp. 742-751, 2013.

[26] M. Saradarzadeh, S. Farhangi, J. L. Schanen, P. O. Jeannin, and D. Frey, "Application of cascaded H-bridge distribution-static synchronous series compensator in electrical distribution system power flow control," *IET Power Electronics,* vol. 5, pp. 1660-1675, 2012.

[27] L. Liu, H. Li, Y. Zhao, X. He, and Z. J. Shen, "1 MHz cascaded Z-source inverters for scalable grid-interactive photovoltaic (PV) applications using GaN device," in *2011 IEEE Energy Conversion Congress and Exposition*, 2011, pp. 2738-2745.

[28] S. Dongsen, G. Baoming, F. Z. Peng, A. R. Haitham, B. Daqiang, and L. Yushan, "A new grid-connected PV system based on cascaded H-bridge quasi-Z source inverter," in *2012 IEEE International Symposium on Industrial Electronics*, 2012, pp. 951-956.

[29] P. Fang Zheng, S. Miaosen, and Q. Zhaoming, "Maximum boost control of the Z-source inverter," *IEEE Transactions on Power Electronics,* vol. 20, pp. 833-838, 2005.

[30] M. Shen, W. Jin, A. Joseph, F. Z. Peng, L. M. Tolbert, and D. J. Adams, "Maximum constant boost control of the Z-source inverter," in *Conference Record of the 2004 IEEE Industry Applications Conference, 2004. 39th IAS Annual Meeting.*, 2004, pp. 1-147.

[31] Y. Liu, B. Ge, H. Abu-Rub, and F. Z. Peng, "Overview of Space Vector Modulations for Three-Phase Z-Source/Quasi-Z-Source Inverters," *IEEE Transactions on Power Electronics,* vol. 29, pp. 2098-2108, 2014.

[32] Y. Liu, B. Ge, and H. Abu-Rub, "Modelling and controller design of quasi-Z-source cascaded multilevel inverter-based three-phase grid-tie photovoltaic power system," *IET Renewable Power Generation,* vol. 8, pp. 925-936, 2014.

[33] X. Yu, Q. Lei, and F. Z. Peng, "Boost converter; Inverter system using PWAM for HEV/EV motor drive," in *2012 Twenty-Seventh Annual IEEE Applied Power Electronics Conference and Exposition (APEC)*, 2012, pp. 946-950.

[34] D. Vinnikov, I. Roasto, R. Strzelecki, and M. Adamowicz, "Step-Up DC/DC Converters With Cascaded Quasi-Z-Source Network," *IEEE Transactions on Industrial Electronics,* vol. 59, pp. 3727-3736, 2012.

[35] T. Sato, T. Shimo, T. Takiguchi, and H. Koizumi, "Bidirectional cascaded quasi-Z-source DC-DC converter," in *IECON 2014 - 40th Annual Conference of the IEEE Industrial Electronics Society*, 2014, pp. 1270-1276.

[36] Y. P. Siwakoti, F. Blaabjerg, P. C. Loh, and G. E. Town, "High-voltage boost quasi-Z-source isolated DC/DC converter," *IET Power Electronics,* vol. 7, pp. 2387-2395, 2014.

[37] M. K. Nguyen, Y. C. Lim, and S. J. Park, "A Comparison Between Single-Phase Quasi-Source and Quasi-Switched Boost Inverters," *IEEE Transactions on Industrial Electronics,* vol. 62, pp. 6336-6344, 2015.

[38] F. B. R. Teodorescu, "Proportional-Resonant Controllers. A New Breed of Controllers Suitable for Grid-Connected Voltage-Source Converters," *Journal of Electrical Engineering*.

[39] Z. Li, C. Zang, P. Zeng, H. Yu, H. Li, L. Gao*, et al.*, "Robust mixed H2 / Hinfinity; based optimal controller design for single-phase grid-connected converter," in *2016 Chinese Control and Decision Conference (CCDC)*, 2016, pp. 1230-1234.

[40] S. Andrews and S. Joshi, "Performance Improvement of Dynamic Voltage Restorer using Proportional - Resonant Controller," in *Proceedings of PCIM Europe 2015; International Exhibition and Conference for Power Electronics, Intelligent Motion, Renewable Energy and Energy Management*, 2015, pp. 1-8.

[41] M. N. S. K. Shabbir, E. Haque, and A. B. Shams, "Reduction of settling time and minimization of transient overshoot of a buck converter," in *2016 5th International Conference on Informatics, Electronics and Vision (ICIEV)*, 2016, pp. 345-350.

[42] D. Vinnikov, I. Roasto, R. Strzelecki, and M. Adamowicz, "CCM and DCM operation analysis of cascaded quasi-Z-source inverter," in *2011 IEEE International Symposium on Industrial Electronics*, 2011, pp. 159-164.

[43] A. Kumar and R. K. Singh, "Power loss calculation of diode assisted cascaded Quasi-Z-source converter with CCM and DCM operation," in *2016 IEEE 6th International Conference on Power Systems (ICPS)*, 2016, pp. 1-6.

[44] L. K. Haw, M. Dahidah, and N. Mariun, "Cascaded multilevel inverter based STATCOM with power factor correction feature," in *2011 IEEE Conference on Sustainable Utilization and Development in Engineering and Technology (STUDENT)*, 2011, pp. 1-7.

[45] L. Shengqing, L. Weizhou, X. Wenxiang, and Z. Huanyue, "The Direct Current Control Method of STATCOM and It's Simulation," in *2013 Third International Conference on Intelligent System Design and Engineering Applications*, 2013, pp. 1426-1429.

[46] M. Berrera, A. Dolara, R. Faranda, and S. Leva, "Experimental test of seven widely-adopted MPPT algorithms," in *2009 IEEE Bucharest PowerTech*, 2009, pp. 1-8.

[47] S. S. Mohammed and D. Devaraj, "Simulation of Incremental Conductance MPPT based two phase interleaved boost converter using MATLAB/Simulink," in *2015 IEEE International Conference on Electrical, Computer and Communication Technologies (ICECCT)*, 2015, pp. 1-6.

[48] J. H. Park, H. G. Kim, E. C. Nho, and T. W. Chun, "Capacitor voltage control for MPPT range expansion and efficiency improvement of grid-connected Quasi Z-Source Inverter," in *The 2010 International Power Electronics Conference - ECCE ASIA -*, 2010, pp. 927-931.

[49] L. Yushan, H. Abu-Rub, G. Baoming, F. Peng, A. T. d. Almeida, and F. J. T. E. Ferreira, "An improved MPPT method for quasi-Z-source inverter based grid-connected photovoltaic

power system," in *2012 IEEE International Symposium on Industrial Electronics*, 2012, pp. 1754-1758.

[50] J. H. Park, H. G. Kim, E. C. Nho, T. W. Chun, and J. Choi, "Grid-connected PV System Using a Quasi-Z-source Inverter," in *2009 Twenty-Fourth Annual IEEE Applied Power Electronics Conference and Exposition*, 2009, pp. 925-929.

[51] F. Li, B. Ge, D. Sun, D. Bi, F. Z. Peng, and A. R. Haitham, "Quasi-Z source inverter with battery based PV power generation system," in *2011 International Conference on Electrical Machines and Systems*, 2011, pp. 1-5.

[52] R. Sivaranjani, "StatCom control at wind farms with fixed-speed induction generators under asymmetrical grid faults," in *2016 International Conference on Electrical, Electronics, and Optimization Techniques (ICEEOT)*, 2016, pp. 3442-3447.

[53] J. Muñoz, J. Rohten, J. Espinoza, P. Melín, C. Baier, and M. Rivera, "Review of current control techniques for a cascaded H-Bridge STATCOM," in *2015 IEEE International Conference on Industrial Technology (ICIT)*, 2015, pp. 3085-3090.

[54] K. H. Law, "An Effective Voltage Controller for Quasi Z-Source Inverter based STATCOM with Constant DC-Link Voltage," *IEEE Transactions on Power Electronics,* pp. 1-1, 2017.

[55] L. K. Haw, M. S. A. Dahidah, and H. A. F. Almurib, "A New Reactive Current Reference Algorithm for the STATCOM System Based on Cascaded Multilevel Inverters," *IEEE Transactions on Power Electronics,* vol. 30, pp. 3577-3588, 2015.

[56] L. K. Haw, M. S. A. Dahidah, and H. A. F. Almurib, "SHE-PWM Cascaded Multilevel Inverter With Adjustable DC Voltage Levels Control for STATCOM Applications," *IEEE Transactions on Power Electronics,* vol. 29, pp. 6433-6444, 2014.

[57] B. Ge, Y. Liu, H. Abu-Rub, and F. Z. Peng, "State-of-Charge Balancing Control for a Battery-Energy-Stored Quasi-Z-Source Cascaded-Multilevel-Inverter-Based Photovoltaic Power System," *IEEE Transactions on Industrial Electronics,* vol. 65, pp. 2268-2279, 2018.

[58] W. Liang, B. Ge, Y. Liu, H. Abu-Rub, R. S. Balog, and Y. Xue, "Modeling, analysis, and impedance design of battery energy stored single-phase quasi-Z source photovoltaic inverter system," in *2016 IEEE Energy Conversion Congress and Exposition (ECCE)*, 2016, pp. 1-6.

[59] D. N. Zmood and D. G. Holmes, "Stationary frame current regulation of PWM inverters with zero steady-state error," *IEEE Transactions on Power Electronics,* vol. 18, pp. 814-822, 2003.

[60] J. Zhang, L. Li, D. G. Dorrell, and Y. Guo, "Space vector modulation based proportional resonant current controller with selective harmonics compensation for matrix converter systems," in *2017 20th International Conference on Electrical Machines and Systems (ICEMS)*, 2017, pp. 1-6.

[61] Y. Liu, B. Ge, H. Abu-Rub, and F. Z. Peng, "An Effective Control Method for Three-Phase Quasi-Z-Source Cascaded Multilevel Inverter Based Grid-Tie Photovoltaic Power System," *IEEE Transactions on Industrial Electronics,* vol. 61, pp. 6794-6802, 2014.

Appendix

Appendix A: Derivation of Inductor Current Transfer Function in Non-Shoot-Through state

During shoot-through state

$$V_{DC_{ST}} = 0 \tag{A-1}$$

Where $V_{DC_{ST}}$ is the DC-link voltage in shoot-through state.

$$I_{DC_{ST}} = I_{L1_{ST}} \tag{A-2}$$

Where $I_{DC_{ST}}$ and $I_{L1_{ST}}$ is the DC-link output current and inductor 1 current respectively.

During non-shoot-through state (i.e., active-state), the DC-link output current is equal to the AC output current. In equation (A-3), $I_{DC_{NST}}$ represents DC-link output current, while I_o represents the AC output current generated.

$$I_{DC_{NST}} = I_o \tag{A-3}$$

Over a full switching cycle, the output power, P_{out} is defined as:

$$P_{out} = V_{DC_{nst}} \times I_{DC_{nst}} \times (1 - D) + V_{DC_{ST}} \times I_{DC_{ST}} \times D$$

$$P_{out} = V_{DC_{nst}} \times I_{DC_{nst}} \times (1 - D) + 0 \times I_{DC_{ST}} \times D$$

$$P_{out} = V_{DC_{nst}} \times I_o \times (1 - D) \tag{A-4}$$

Assuming input power equal to output power (i.e., $P_{in} = P_{out}$).

$$V_{in} \times I_{L1} = V_{DC_{nst}} \times I_o \times (1 - D)$$

$$V_{in} \times I_{L1} = \frac{1}{1 - 2D} \times V_{in} \times I_o \times (1 - D)$$

$$I_{L1} = \frac{1 - D}{1 - 2D} \times I_o \tag{A-5}$$

Appendix B: qZSI transfer function design procedure

This section describes the calculation of the qZSI transfer function as shown in section 4.2.1. The parameters in Table 4.1 is substituted to qZSI transfer functions to obtain numerical equation for controller design in later stage. To generate a 50V voltage from 12V input voltage, duty cycle of 0.38 in value is used. The inductor current can be calculated using equation (3.46). In shoot-through state, the AC output current is equal to zero. In non-shoot-through state, the AC output current can be calculated with following equation:

$$I_{AC} = \frac{V_o}{R} = \frac{V_{DC}}{R} = \frac{50V}{50\Omega} = 1A$$

$$I_L = \frac{1 - D_{ST}}{1 - 2D_{ST}} I_{AC}$$

$$I_L = \frac{1 - 0.38}{1 - 2 \times 0.38}(1) = 2.583A$$

The minimum inductor value for qZSI to stay in CCM based on parameters shown in Table 4.1

$$L_{min} = \frac{(V_{in} + V_{C2})D_{ST}}{2I_L \times f_s} = \frac{(12 + 19)(0.38)}{2 \times 2.583 \times 10000} = 0.000228H = 2.28\mu H$$

Since the inductance used in section 4.2.1 is lower than the calculated minimum inductor value, the designed qZSI is operating in DCM. To calculate the voltage loop transfer function, equation (5.36) is used.

$$G_{\widehat{v_c}\widehat{d_{ST}}} = \frac{\left[(I_o - I_{L1} - I_{L2})\big(Ls + (r + R)\big) + (V_{C1} + V_{C2} - RI_{DC})(1 - 2D_{ST})\right]}{[LCs^2 + C(R + r)s + (1 - 2D_{ST})^2]}$$

$$G_{\widehat{v_c}\widehat{d_{ST}}} = \frac{\left[(1 - 2.583 - 2.583)\big(100 \times 10^{-6}s + (3.22 \times 10^{-2} + 5.60 \times 10^{-2})\big) + (31 + 19 - 5.60 \times 10^{-2})(1 - 2 \times 0.38)\right]}{[(100 \times 10^{-6} \times 1 \times 10^{-3})s^2 + (1 \times 10^{-3})(3.22 \times 10^{-2} + 5.60 \times 10^{-2})s + (1 - 2 \times 0.38)^2}$$

$$G_{\widehat{v_c}\widehat{d_{ST}}} = \frac{-0.000417s + 11.61906}{0.0000001s^2 + 0.0000882s + 0.0576}$$

From the above calculation, it is obvious that the qZSI transfer function has a right-hand plane zero at $s = 27863.5$, therefore, this indicates that qZSI operates in non-minimum phase. To calculate the current inner loop transfer function, equation (4.37) is used.

$$G_{\widehat{i_L}\widehat{d_{ST}}} = \frac{Cs(V_{C1} + V_{C2} - RI_o) + (I_{L1} + I_{L2} - I_o)(1 - 2D_{ST})}{\left[(Ls + R + r)[LCs^2 + (R + r)Cs + (1 - 2D_{ST})^2]\right]}$$

$$G_{\widehat{v_c}\widehat{d_{ST}}}$$

$$= \frac{(100 \times 10^{-3})s(31 + 19 - 50) + (2.583 + 2.583 - 1)(1 - 2 \times 0.38)}{[(100 \times 10^{-6} \times 1 \times 10^{-3})s^2 + (1 \times 10^{-3})(3.22 \times 10^{-2} + 5.60 \times 10^{-2})s + (1 - 2 \times 0.38)^2}$$

$$G_{\widehat{v_c}\widehat{d_{ST}}} = \frac{4.99 \times 10^{-2}s + 1}{0.0000001s^2 + 0.0000882s + 0.0576}$$

Similar calculation can be performed calculated for the parameters shown in section 4.2.2.

Appendix C: Tuning of PI controller in MATLAB/SIMULINK

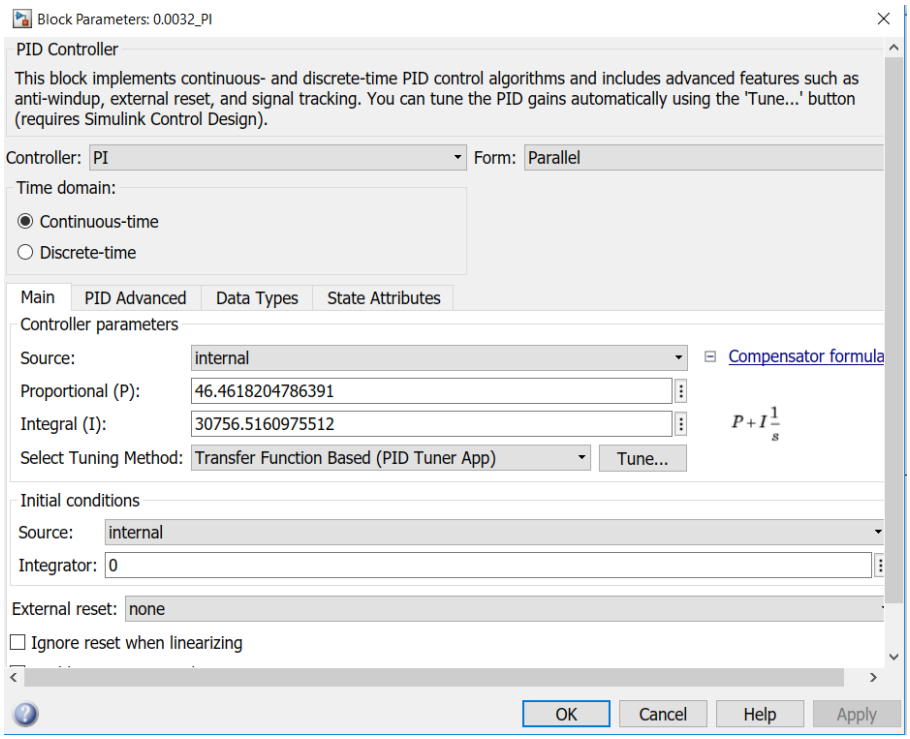

Figure A-1: PI controller tuning block diagram in MATLAB/SIMULINK

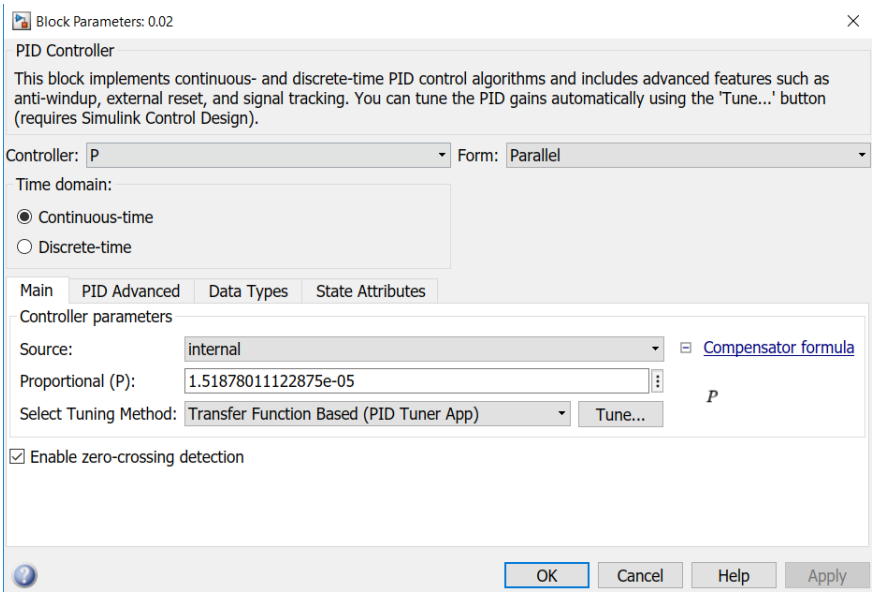

Figure A-2: P controller tuning block diagram in MATLAB/SIMUINK

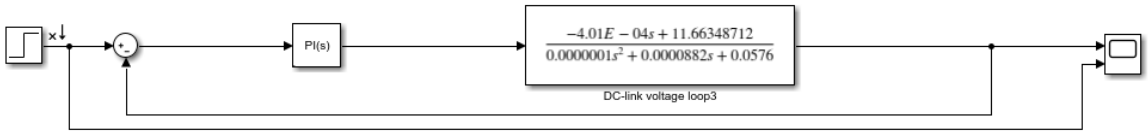

Figure A-3: DC-link voltage control loop with PI controller

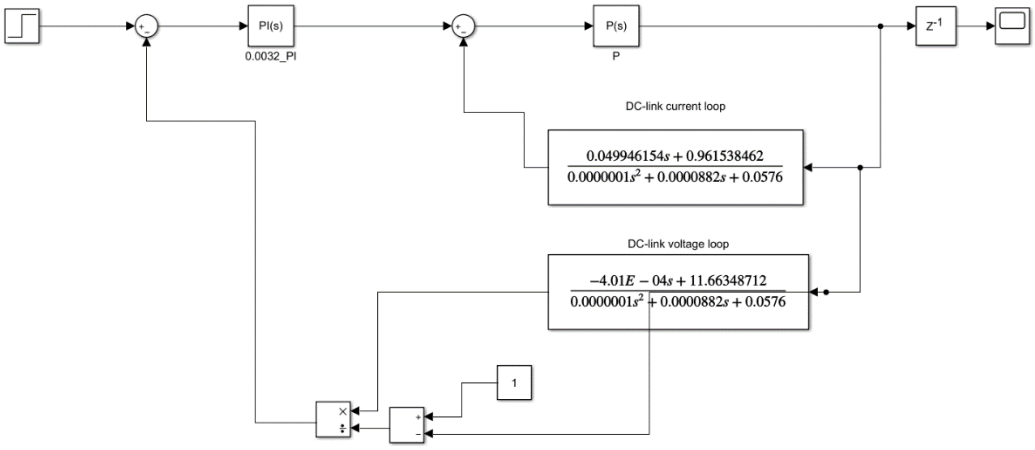

Figure A-4: Complete DC-link control system of qZSI model (with voltage and current inner loop)

From Figure A-4, the PI controller represents the controller used in the DC-link voltage loop, whereas the P controller is used in the inner current loop. Control system with PI-P controller requires tuning both the PI and P controller concurrently as each of the controller does have impact the overall transient response. Adjusting the transient time and the transient behaviour of the controller until obtain satisfaction results.

Similar approach can be done by tuning the proportional gain of the current inner loop when lead compensator is used in the voltage loop. However, lead compensator is always designed ahead of the tuning procedure as this provide more flexibility to the design process. The lead compensator will make sure that the voltage loop can attain stable transient and dynamic response beforehand, reducing the burden of the P controller.

Appendix D: Simulation Model

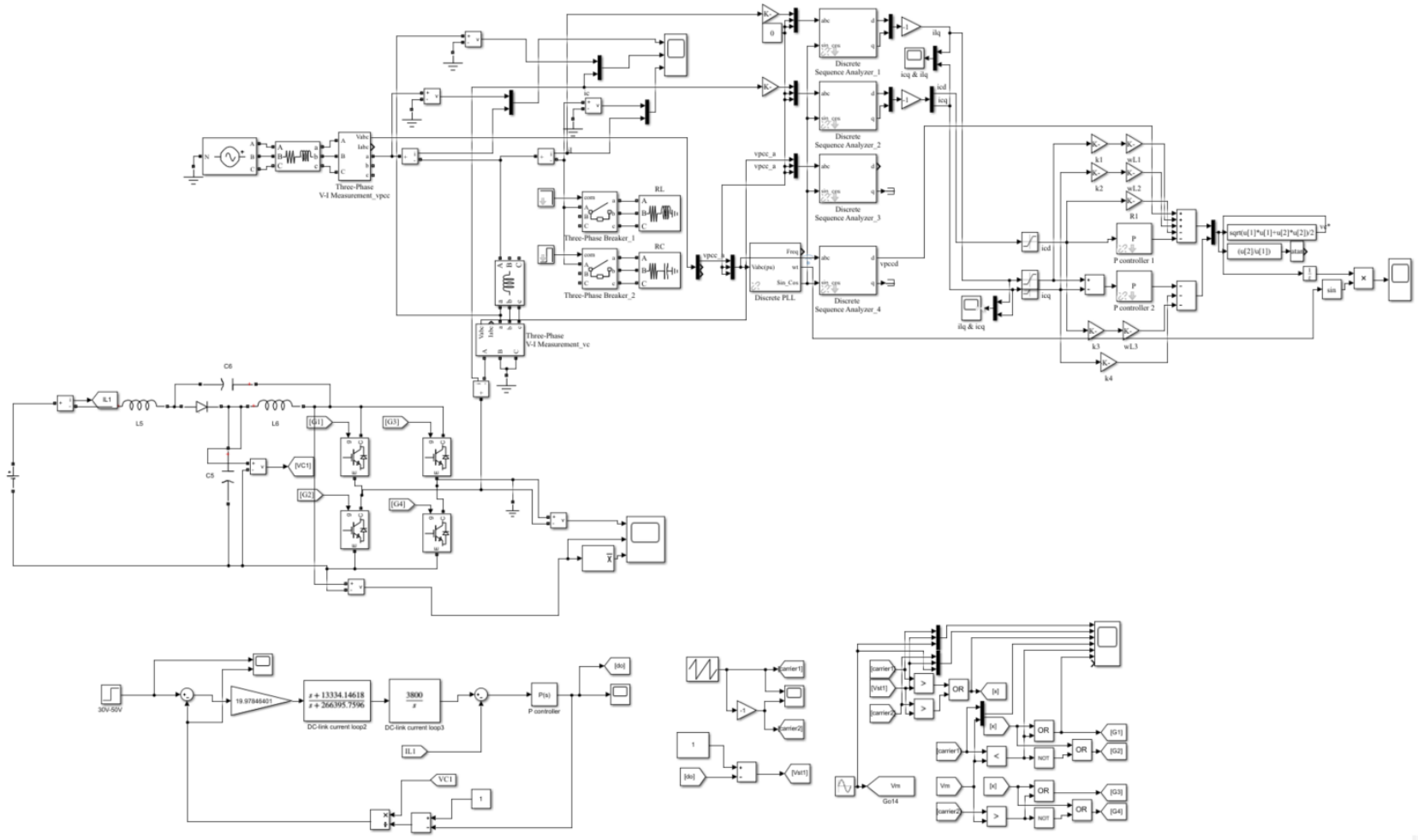

Figure A-5: Complete SIMULINK design of grid-tie qZSI based STATCOM system

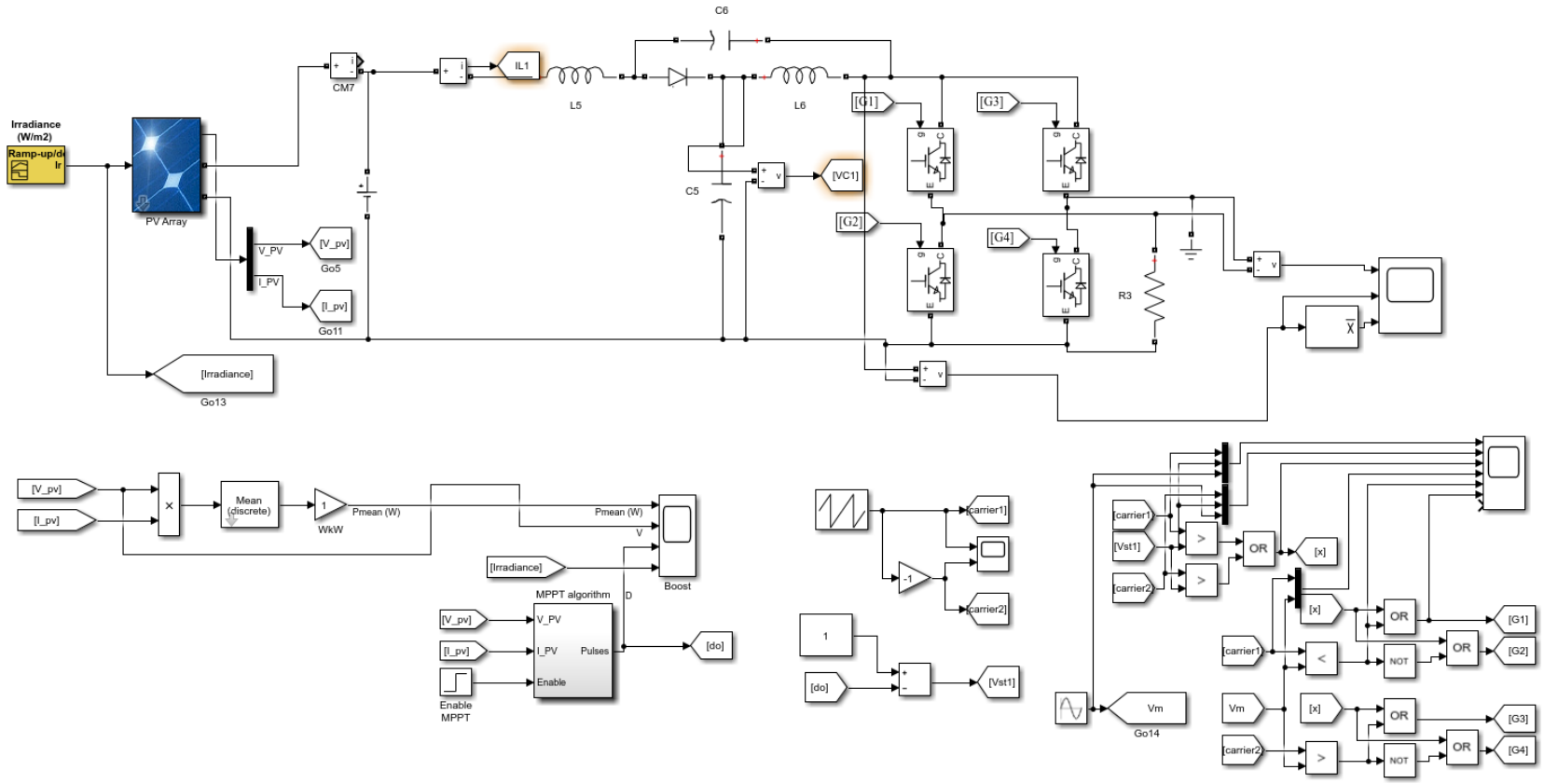

Figure A-6: qZSI topology with MPPT control

Appendix E: MPPT Algorithm MATLAB C Code

The following appendix shows the MPPT algorithm (i.e., Perturb and Observed Algorithm) MATLAB coding.

```
function D  = POalgorithm(Parameter, Enabled, V, I)

Dint = Parameter(1);  %initial D
Dmax = Parameter(2);   %Maximum value for D (0.5)
Dmin = Parameter(3);   %Minimum value for D
deltaD = Parameter(4); %increment of D in each cycle

persistent V_old P_old D_old;

dataType = 'double';

if isempty(V_old)
   V_old=0;
   P_old=0;
   D_old=Dint;
end
P= V*I;
dV= V – V_old;
dP= P – P_old;

if dP ~= 0 & Enabled ~=0
   if dP < 0
      if dV < 0
         D = D_old - deltaD;
```

```
        else
            D = D_old + deltaD;
        end
    else
        if dV < 0
            D = D_old + deltaD;
        else
            D = D_old - deltaD;
        end
    end
else D=D_old;
end

if D >= Dmax | D<= Dmin
    D=D_old;
end

D_old=D;
V_old=V;
P_old=P;
```